



**VORTEX GENERATION AND BUBBLE DYNAMICS IN
A MICROFLUIDIC CHAMBER WITH ACTUATIONS**

SHANG XIAOPENG

SCHOOL OF MECHANICAL & AEROSPACE ENGINEERING

2017

VORTEX GENERATION AND BUBBLE DYNAMICS IN A MICROFLUIDIC CHAMBER WITH ACTUATIONS

SHANG XIAOPENG

School of Mechanical & Aerospace Engineering

A thesis submitted to Nanyang Technological University in partial fulfillment of
the requirement of the degree of
Doctor of Philosophy

2017

Abstract

This dissertation presents a comprehensive study on vortex generation, vortex control and bubble dynamics in a microfluidic chamber with PZT (lead-zirconate-titanate) actuations, which can be applied to mixing enhancement and manipulations of microparticles and nanoparticles in microfluidics. The microfluidic chamber is featured with an acoustic resonator shape, and the PZT disk is formed as part of the chamber walls. The working fluid (DI water) is pumped into the chamber with a controllable flowrate. Both vortices and bubbles are generated inside the chamber, depending on the actuation conditions.

In the study on vortex generation, it is found that, at proper actuation conditions, large-scale vortices are formed inside the chamber, and the vortex generation and intensity can be regulated by the operation conditions, including actuation frequency, voltage and the flowrate through the microfluidic chamber. There is an actuation frequency window between 1.5 kHz and 3 kHz for the vortex generation and at the actuation frequency out of this window, the vortex is very weak or even unable to occur. The vortex intensity is found to increase with actuation voltage, and decreases with the flowrates.

The direction of the generated vortex can, in principle, be clockwise or counter-clockwise due to the symmetry of the chamber and the PZT actuator. However, it is found that only one type of vortex can occur in an individual microfluidic chamber. This is probably due to the imperfection in the chamber fabrication. The control of the vortex direction has been carried out. The microfluidic chamber is modified by dividing the piezoelectric transducer into two parts which can be actuated separately, so that the actuation becomes asymmetric. In the modified microfluidic chamber, the vortex direction can be shifted on-demand from clockwise to counterclockwise by a switch to alter the working transducer.

The mechanism of the vortex generation in the present study is investigated. It is found that the vibration of the PZT disk induces a large-amplitude pulsatile flow at the outlet channel of the chamber, where the geometry and configuration are similar to a sudden expansion from a narrow channel to a wide chamber. It is proposed that the vortex generation in the present study is due to the instability of the actuation-induced pulsatile flow through the sudden expansion part of the outlet channel at high Reynolds number. The flow velocity, corresponding to the actuation, at the

outlet channel is measured to confirm that the flow Reynolds number at the working conditions is high enough for the vortex generation.

Bubbles can be generated inside the chamber when the actuation voltage is larger than a threshold and the actuation frequency is within the range between 0.5 kHz and 5 kHz. The bubbles can be generated in forms of a single bubble, or as a cloud of bubbles, depending on the applied voltage. Such type of bubble generation is novel compared to the conventional bubble generations in other microfluidic devices reported in open literatures.

The dynamics of multi-bubbles in the chamber with actuations at 1 kHz is investigated both experimentally and numerically. It is found that, under actuations, the bubbles are generated near the center of the chamber, grow up in size and move upstream against the hydrodynamic flow from inlets. Along with the bubbles' motions, coalescences and breakups happen frequently and cause vigorous motions of surrounding liquids, which has a major contribution to the mixing enhancement. The pressure variation and distribution in the chamber are calculated by numerical simulation. The simulation results show that inside the chamber there is a low-pressure zone, which is consistent with the area of bubble generation observed in the experiment. The amplitude of the actuation exceeds the Blake threshold of nuclei ($> 10 \mu\text{m}$), which leads to the explosive growth of the nuclei in the working fluids, and hence the bubble are generated and observed in the experiments.

The dynamics of a single bubble is investigated both experimentally and analytically. It is found that the bubble, after being generated, translates upstream against the flow at an average velocity of about 0.23 m/s, and undergoes significant expansion and compression with a ratio of the maximum to minimum volume up to 22. In order to understand the bubble translation under actuations, a simplified analytical model which describes the dynamics of a bubble nearby two intersected boundaries is constructed by using the Lagrangian scheme and the method of images. The analytical results of the model are found to be agreeable with the experimental observations in terms of the bubble expansion, compression and translation. It is concluded that the bubble translation is caused by the attractive secondary Bjerknes force of image bubbles behind the two inclined walls, which is the so-called wall effect.

Acknowledgments

First and above all, I would like to express my special thanks of gratitude to my supervisor, Associate Professor Huang Xiaoyang, for his patient help, inspiring guidance in my research and sincere solicitude in my personal life during the past years.

I would like to thank Associate Professor Yang Chun, Charles, my co-supervisor, for his enthusiastic enlightenment, continuous motivation and endless support in my study and research during past years.

I would also like to express my appreciation to our technicians Mr. Yuan Kee Hock, Mr. Cheo Hock Leong for their help in experiments. I also thank Dr. Cui Xinguang, Yan Zhibin, Zhu Guiping and Huang Yi and other friends, who share their knowledge and experience with me in these days.

Finally, I would like to thank my wife Li Chong and my daughter Linda, whose love and support have made this work completed.

Abbreviations

AC	alternating current
DI water	de-ionized water
ICEO	induced-charge electroosmosis
LDV	Laser Doppler Vibrometer
PCR	polymerase chain reaction
PIV	Particle image velocimetry
PMMA	polymethylmethacrylate
PZT	lead-zirconate-titanate
RD	rectified diffusion
<i>Re</i>	Reynolds number
TOMV	twin opposing microvortice
UDF	user-defined-function

Contents

Abstract	I
Acknowledgments.....	III
Abbreviations	IV
Contents	V
List of Figures	IX
List of Tables	XVII
Chapter 1 Introduction	1
1.1 Background and motivation	1
1.2 Objectives.....	3
1.3 Outline of the Dissertation	3
Chapter 2 Literature Review	5
2.1 Introduction	5
2.2 Microfluidic vortex generator	6
2.2.1 Vortex in microfluidics.....	6
2.2.2 Passive vortex generators	7
2.2.3 Active vortex generators.....	10
2.3 Cavitation inception and thresholds	17
2.3.1 Cavitation nuclei as bubble sources.....	17
2.3.2 Cavitation threshold.....	18
2.3 Radial dynamics of a bubble in liquid.....	20
2.3.1 Rayleigh-Plesset equation and extensions	21
2.3.2 Linear oscillation of a bubble in oscillatory pressure fields	23
2.3.3 Nonlinear oscillation of a bubble in oscillatory pressure fields	23

2.4 Translational dynamics of a bubble in oscillatory pressure fields	26
2.4.1 Bjerknes force and drag force.....	27
2.4.2 Decoupled model of an oscillating bubble with weak actuations	28
2.4.3 Coupled model of an oscillating bubble with strong actuations.....	29
2.5 Bubble boundary interaction	31
2.6 Bubble dynamics in microfluidics.....	33
Chapter 3 Vortex Generation in a Microfluidic Chamber: Characterization.....	37
3.1 Experimental methods.....	37
3.1.1 Design and fabrication of the microfluidic chamber for vortex generation	37
3.1.2 Experimental setup and characterization.....	39
3.2 Results and discussion.....	41
3.2.1 Flow pattern development in the microfluidic chamber.....	41
3.2.2 Effects of actuation frequency on the generated vortices.....	44
3.2.3 Effects of the applied voltage on the generated vortices	47
3.2.4 Effects of flowrates on the generated vortices.....	49
3.2.5 The vortex generation in a circular chamber	51
3.2.6 The counter-clockwise vortices	52
3.3 Summary	54
Chapter 4 Vortex Generation in a Microfluidic Chamber: Control and Mechanism	55
4.1 Introduction	55
4.2 Experimental methods.....	56
4.2.1 Modification of the microfluidic chamber and experimental setup	56
4.2.2 Measurement of the flow velocity in the outlet channel	58
4.3 Results and discussion.....	59
4.3.1 Visualization of vortex generation and control by fluorescent dyes	59

4.3.2 Effects of actuation conditions on the generated vortices	61
4.3.3. Mechanism of vortex generation and control	64
4.3.4. The flow velocity in the outlet channel	68
4.3.5. Vibration measurement of the PZT disk.....	71
4.4 Summary	73
Chapter 5 Dynamics of multi-bubbles in a Microfluidic Chamber	75
5.1 Introduction	75
5.2 Experimental methods.....	76
5.3 Results and discussion.....	77
5.3.1 Visualization of bubble generation by fluorescent dyes.....	77
5.3.2 Motions of bubbles in the nozzle.....	79
5.3.3 Bubble coalescence and breakup	81
5.3.4 Bubble-wall interactions.....	85
5.4 Numerical simulation	87
5.4.1 Governing equations and boundary conditions	88
5.4.2 Bubble generation by low pressure	90
5.4.3 Volume pulsation by pressure fluctuation	92
5.5 Summary	93
Chapter 6 Dynamics of a single bubble in a Microfluidic Chamber	95
6.1 Introduction	95
6.2 Experimental results and discussion	96
6.2.1. Bubble trajectory of translation	97
6.2.2. Radial oscillation and its interaction with translation	98
6.3 Analytical modelling	100
6.3.1. Analytical modelling for bubble oscillation and translation	101

Contents

6.3.2. Modelling results of bubble oscillation and translation.....	109
6.3.3. Further discussion of bubble translation – wall effect.....	111
6.4 Summary	115
Chapter 7 Conclusions and Recommendations.....	117
7.1 Conclusions	117
7.2 Recommendations for Future Work.....	119
Publication List	120
References	121

List of Figures

Fig. 2.1 Illustration of vortex generators with ridge arrays and generated vortices in microchannels. (a) sloped ridges; (b) herringbone ridges. [17].....	7
Fig. 2.2 (a) Dimensions of the vortex generator integrating “Y” junctions with zigzag microchannels. (b) Velocity vectors obtained at $Re=267$ for zigzag geometries. [18]	8
Fig. 2.3 (a) Schematic illustration of inertial vortex generator. (b) Illustration of the separation principle. The symmetric vortices are indicated by the red dashed lines. (c) Stacked images at various downstream positions illustrating the separation phenomenon at $Re=110$. [19]	9
Fig. 2.4 Flow patterns in the 3D flow-focusing geometry for varying Re . Comparison between experimental (grey-scale images) and numerical pathlines at the centre plane. (a) $Re=2.8$; (b) $Re=6.5$; (c) $Re=94.2$; (d) $Re=113$. [20].....	10
Fig. 2.5 Flow patterns and concentration fields (a) with induced-charge electroosmosis effect and (b) without induced-charge electroosmosis effect. [27]	11
Fig. 2.6 Schematic illustration of the TOMV (twin opposing microvortices) flow with two microvortices (circular arrows) generated by the laser radiation and two coplanar electrodes on the top surface of the microchannel. [32]	12
Fig. 2.7 Stacked images showing various microvortical flows in terms of the location of the laser spots on two electrodes. The laser spot is focused at the middle (a), left side (b), right side (c) of exposed electrode A, and (d) middle of exposed electrode B. [32]	13
Fig. 2.8 Schematic of experimental setup for an acoustic vortex generator. The transducer is positioned adjacent to the channel; a bubble is trapped inside the horse-shoe structure. [34]	14
Fig. 2.9 Characterization of the flow pattern around a single bubble. (a) An air bubble trapped in the horse-shoe structure and stationary particles in the fluid. (b) Vortices around the air bubble when the bubble membrane oscillates at its resonance frequency. [34].....	14
Fig. 2.10 A pair of vortices generated by the bubble oscillation at different driving frequencies (a-d). Outline of the oscillatory bubble superposed over one cycle at different frequencies (e) 9.6 kHz, (f) 20.6 kHz, (g) 48.6 kHz, and (h) 100.3 kHz. [35].....	15
Fig. 2.11 The natural convection-driven flows in a microfluidic chamber. (A to D): trajectories of fluorescent particles in time sequences. [40].....	15

Fig. 2.12 Fluorescence images of microparticles during agitation. The flow can be directed in a clockwise (left-hand panels) or counter-clockwise (right-hand panels) fashion. [41]	16
Fig. 2.13 Radius as a function of time for one cycle of the motion of a bubble of 2 μm . The bubble dynamics is described by the Rayleigh–Plesset equation. [61]	24
Fig. 2.14 Upper graph: Radius-time curve of an oscillating bubble calculated by Miksis model. Bubble radius at rest $R_0=1\text{ }\mu\text{m}$, driving frequency $f=20\text{ kHz}$ and the pressure amplitude $P_a=142\text{ kPa}$ (dash-dotted line), 143.5 kPa (dashed line), and 144 kPa (solid line). [63]	25
Fig. 2.15 Left: Photographs of a bubble driven at 21.4 kHz and 132 kPa . Right: Comparison of the numerically calculated curve (solid line) and experimental data (open circles). [67]	26
Fig. 2.16 Free oscillation of a laser bubble in water: the framing rate is $75,000$; maximum radius is 2 mm . [68]	26
Fig. 2.17 Two cases of stable radial and translational response of a bubble ($R_0=2.0\text{ mm}$) after 29 periods of forcing when it undergoes: (a) mild, super-resonant actuation (b) subresonant excitation. [72]	30
Fig. 2.18 Jerky motion of two bubbles with strong actuations: vertical stripes from successive frames are displayed next to each other, time proceeding from left to right. The acoustic frequency is 20 kHz , and the inter-frame time is 0.4 periods. [77]	31
Fig. 2.19 Photograph of a laser bubble collapsing in the vicinity of a glass wall located at the bottom (time between frames: $5\text{ }\mu\text{s}$). [78]	32
Fig. 2.20 Selected frames showing the translations of several bubbles at (a) 0 ms , (b) 20 ms , (c) 40 ms , (d) 60 ms , (e) 100 ms , (f) 200 ms , (g) 300 ms , (h) 400 ms , and (i) 500 ms . The pressure amplitude was 11.5 kPa . [79]	33
Fig. 2.21 (a) The microfluidic flow-focusing device (top view). (b) Illustration of a bubble in the outlet channel. [84]	34
Fig. 2.22 (a) Schematic of apparatus for bubble generation via a flow-focusing section with external actuations; (b) A series of selected frames of bubble formation captured by highspeed photography at 7692 frames/s . [85]	34
Fig. 2.23 (A) Schematic design of the sorter of microbubbles using the primary Bjerknes force. (B) Photograph of the flow focusing section. (C) Microbubbles are formed in a narrow orifice. (D) A travelling wave changes the trajectory of a series of bubbles. [87]	35

Fig. 3.1 Schematic illustration of the microfluidic chamber with resonator-shaped nozzle. (a) Side view of the configuration; (b) Top view of the configuration with channel design and geometric dimensions.	38
Fig. 3.2 Schematic illustration of the microfluidic chamber without resonator-shaped nozzle. (a) Side view of the configuration; (b) Top view of the configuration with channel design and geometric dimensions.	38
Fig. 3.3 The concept of fabrication and the assembled device.	39
Fig. 3.4 Schematic illustration of the experimental setup for vortex visualization.	40
Fig. 3.5 The microfluidic chamber filled with working fluids and the cross line C'-O-C for vortex characterization.	40
Fig. 3.6 Recorded images in time sequence to show the vortex generated in the microfluidic chamber with actuations. The actuation voltage and frequency were 100 V and 2.0 kHz, and the flowrate was 2 mL/h at each inlet.	42
Fig. 3.7 The dependence of the vortex intensity with time after being formed in the chamber. The actuation voltage and frequency were 100 V and 2.0 kHz, and the flowrate was 2 mL/h at each inlet.	43
Fig. 3.8 Recorded images in time sequence to show the development of the flow pattern under the actuation of 1.5 kHz. The actuation voltage was 100 V and the flowrate was 2 mL/h at each inlet.	44
Fig. 3.9 Recorded images in time sequence to show the development of the flow pattern under the actuation of 2.5 kHz. The actuation voltage was 100 V and the flowrate was 2 mL/h at each inlet.	45
Fig. 3.10 Development of the vortex intensity versus time after the actuation is turned on under various actuation frequencies. The applied voltage and flowrate were fixed at 100 V and 2 mL/h, respectively.	46
Fig. 3.11 Effect of actuation frequency on vortex formation and intensity after the flow patterns are fully developed. The inset images were recorded at 50 seconds. The PZT disk was actuated at the voltage of 100 V and the flowrate was 2 mL/h at each inlet.	46
Fig. 3.12 The images of the flow patterns under various applied voltages from 40 V to 120 V for the DI water. The images were recorded at 50 seconds after actuation is switched on. The driving frequency was 2.0 kHz and the flowrate was 2 mL/h at each inlet.	47

Fig. 3.13 Development of the vortex intensity versus time after the actuation is turned on under various applied voltages. The actuation frequency and flowrate at each inlet were fixed at 2.0 kHz and 2 mL/h, respectively.....	48
Fig. 3.14 Effect of the applied voltage on vortex formation and intensity after the flow patterns are fully developed. The inset images were recorded at 50 seconds. The PZT disk was actuated at the frequency of 2.0 kHz and the flow rate was 2 mL/h at each inlet.	49
Fig. 3.15 Development of the vortex intensity versus time after the actuation is turned on under various flowrates. The actuation frequency and voltage were fixed at 2.0 kHz and 100 V, respectively.....	50
Fig. 3.16 Effect of flowrates on vortex formation and intensity in DI water. The inset images were recorded at 50 seconds after actuation is switched on. The PZT disk was actuated with frequency 2.0 kHz and the applied voltage was 100 V.	50
Fig. 3.17 Visualization of the generated vortex in a circular chamber at the voltage of 140 V. The actuation frequency was 2.0 kHz and the flowrate was 2 mL/h at each inlet.	51
Fig. 3.18 Development of the vortex intensity versus time after the actuation is turned on in a circular chamber. The actuation frequency and voltage were fixed at 2.0 kHz and 140 V, and the flowrate at each inlet is 2 mL/h.	52
Fig. 3.19 Visualization of the generated vortex in the counter-clockwise direction. The actuation frequency was 2.0 kHz, the voltage 100 V and the flowrate 2 mL/h at each inlet.....	53
Fig. 3.20 The intensity of a counter-clockwise vortex versus time after the actuation is turned on. The actuation frequency and voltage were fixed at 2.0 kHz and 100 V, and the flowrate 2 mL/h at each inlet.	53
Fig. 4.1 Illustration of the modified microfluidic chamber and experimental setup. (a) Side view of the configuration. (b) Top view and geometric dimensions of the configuration. (c) Schematic illustration of the assembled device. (d) Schematic illustration of the experimental setups. The velocity in the rectangular region – zone 1 is measured.	57
Fig. 4.2 (a) Illustration of the PZT disk. The PZT disk consists of two separate transducers and a brass sheet. (b) The vibration profile of the PZT disk when Transducer A is working. (c) The vibration profile of the PZT disk when Transducer B is working.....	58
Fig. 4.3 Schematic illustration of the measurement of the velocity field in the outlet channel. The velocity in the rectangular region – zone 1 is measured.....	59

- Fig. 4.4 Recorded images of the flow pattern development with time. Clockwise vortex (CW vortex) is generated when Transducer A is actuated (a-e) and counter-clockwise vortex (CCW vortex) is generated when Transducer B is actuated (g-k). The actuation voltage and frequency are 100 V and 1.5 kHz respectively, and the flowrate is 10 mL/h in total. The traces of particles of CW vortex (f) and CCW vortex (l) are in accordance with the flow patterns of fluorescent dyes, respectively. 61
- Fig. 4.5 Effect of actuation frequency on the generated vortex when Transducer A (solid line) or Transducer B (dashed line) of the PZT disk is actuated. The actuation voltage is 100 V and the flowrate is 10 mL/h in total. All the flow patterns are recorded at 50 s. 62
- Fig. 4.6 Effect of the actuation voltage on the generated vortex when Transducer A (solid line) or Transducer B (dashed line) of the PZT disk is actuated. The actuation frequency is 1.5 kHz and the flowrate is 10 mL/h in total. The inset images are recorded when flows are fully developed at 50 s. 63
- Fig. 4.7 Effect of flowrate on the generated vortex when Transducer A (solid line) or Transducer B (dashed line) of the PZT disk is actuated. The actuation frequency is 1.5 kHz and the voltage is 100 V, respectively. The inset images are recorded when flows are fully developed at 50 s. 63
- Fig. 4.8 Illustration of the flow through a sudden expansion or rectangular chamber. (a) The flow transition from a pair of symmetric vortices to asymmetric at high Reynolds number. [96] (b) Transition of the flow in a rectangular chamber from symmetric to asymmetric when the Reynolds number is above the critical value. [98] (c) The asymmetric flow in a sudden expansion with a large expansion ratio at high Reynolds number. [100] (d) The asymmetric flow in a rectangular chamber with a large expansion ratio at high Reynolds number. [101] ER is the expansion ratio. 65
- Fig. 4.9 The fluids flow into and out of the chamber through the outlet channel with the vibration of the PZT disk. 67
- Fig. 4.10 The fluids flow through a suddenly expanded part with a very large expansion ratio (ER) in the outlet channel when the PZT disk is vibrating. 67
- Fig. 4.11 The velocity fields in the outlet channel at six moments of one cycle when the actuation frequency is 1.5 kHz. 68

Fig. 4.12 The variation of the cross-section mean velocity in zone 1 of the outlet channel with time in one cycle when Transducer A (solid line) or Transducer B (dashed line) is working.	69
Fig. 4.13 The effect of the actuation frequency on the amplitude of the pulsatile velocity in the outlet channel when Transducer A (solid line) or Transducer B (dashed line) is actuated. ...	70
Fig. 4.14 Schematic illustration of the experimental setup for measuring the vibration velocity and displacement of the PZT disk.	71
Fig. 4.15 (a) Vibration velocity amplitude of the center O with the actuation frequency. (b) Vibration displacement amplitude of the center O with the actuation frequency. Solid line – Transducer A is working; Dashed line – Transducer B is working.....	72
Fig. 4.16 Side view of the microfluidic chamber for vortex generation. The fluids are actuated into and out of the microfluidic chamber due to the volume change corresponding to the PZT vibration.....	73
Fig. 5.1 Schematic illustration of the microfluidic chamber. (a) Side view of the configuration. (b) Top view of the chamber with geometric dimensions. The rectangular region zone 2 is selected to record the bubble's motion.	76
Fig. 5.2 Schematic illustration of the experimental setup.....	77
Fig. 5.3 Visualization of the bubbles generated in the chamber with the actuation at frequency 1.0 kHz and voltage 150 V. (a) Recorded image before actuation: the flow is laminar throughout the microfluidic chamber. (b) Recorded image when the actuation is switched on: the bubbles are generated. (c) Recorded image showing that the bubbles are traveling upstream against the main stream. (d) Recorded image when the bubbles arrive at some position close to the straight channel. The flowrate is 10 mL/h in total and the flow direction is from right to left.	79
Fig. 5.4 Photographic series of the dynamics of bubbles in one cycle after being generated. The time interval between two successive images is $1/6 T$, or 0.167 ms. The actuation voltage and frequency are 150 V and 1 kHz, respectively.	80
Fig. 5.5 Images of moving bubbles captured at the same phase of different cycles. The time between two successive images shown in the figure is one period, that is, 0.001 second. The actuation voltage and frequency are 150 V and 1 kHz, respectively.	81

Fig. 5.6 Coalescence of two oscillating bubbles. One small bubble is attracted by a large one and then the two bubbles merge together to form a single one. The time between two successive images is $1/12 T$, or 0.083 ms. The actuation voltage and frequency are 150 V and 1 kHz, respectively.....	82
Fig. 5.7 Breakup of one oscillating bubble at the phase of the violent collapse. The time between two successive images is $1/12 T$, or 0.083 ms. The actuation voltage and frequency are 150 V and 1 kHz, respectively.....	84
Fig. 5.8 A series of coalescence and breakup of the oscillating bubbles in the process of translation. The time between two successive images is $1/12 T$, or 0.083 ms. The actuation voltage and frequency are 150 V and 1 kHz, respectively.	85
Fig. 5.9 The dynamics of an oscillating bubble nearby the upper boundary (1-13) and the trajectory of the bubble by stacking three images of the bubble corresponding to the same phase in a cycle. The time between two successive images is $1/12 T$, or 0.083 ms. The actuation voltage and frequency are 120 V and 1 kHz, respectively.	86
Fig. 5.10 The dynamics of an oscillating bubble nearby the bottom boundary (1-13) and the trajectory of the bubble by stacking three images of the bubble corresponding to the same phase in a cycle. The time between two successive images is $1/12 T$, or 0.083 ms. The actuation voltage and frequency are 120 V and 1 kHz, respectively.	87
Fig. 5.11 (a) Geometry and dimension of the numerical simulation domain. (b) Meshing scheme in x-y plane (not to scale). (c) Meshing scheme in the height direction (not to scale).....	89
Fig. 5.12 The pressure distributions inside the chamber by numerical simulation. (a) Pressure distribution without actuation. (b) Pressure distribution under an actuation of frequency $f = 1.0$ kHz at $0.75 T$ ($T = 1/f = 0.001$ s). The pressure at Point A is 469 Pa.	91
Fig. 5.13 Pressure fluctuation in one cycle at point P (0.013, 0, -0.00015) in zone 2. $T = 1/f = 0.001$ s.....	93
Fig. 6.1 Schematic illustration of the experimental setup. The motion of a single bubble moving through zone 2 is recorded by a high-speed camera and then analyzed in MATLAB.....	96
Fig. 6.2 Movement of a single bubble towards upstream along a straight line after being generated in the chamber. The trajectory is obtained by stacking four images of the bubble corresponding to the same phase in a cycle and the time between two successive images is two periods, that is, 0.002 seconds.	97

Fig. 6.3 (a) Images of a moving single bubble captured at the same phase in different cycles. (b) The displacement of the bubble versus time normalized by the actuation period $T = 0.001$ s. The average translation velocity of the bubble is estimated to be 0.23 m/s, based on the slope of the displacement curve.	98
Fig. 6.4 Images of a bubble under the actuation of two successive cycles, showing remarkable volume oscillation. The time between two successive images is $1/12 T$ with $T = 0.001$ s being the actuation period.	99
Fig. 6.5 (a) Variation of the bubble radius in two successive cycles. (b) Variation of the bubble displacement in two successive cycles. The bubble moves forward at the phase of collapse. $T = 0.001$ s, is the actuation period.	100
Fig. 6.6 Illustration of the analytical model. (a) In the experiment, the bubble is in zone 2 of the microfluidic chamber. (b) In the model, the bubble is located in a position on the bisector line of two inclined straight walls.	102
Fig. 6.7 The model and image system for a bubble located nearby two inclined walls.	103
Fig. 6.8 The whole process of the motions of the bubble nearby two tapered walls. The whole bubble movement corresponds to three stages: uniform movement, accelerated movement and final impact towards the walls. (a) Radius of the bubble with time. (b) Displacement of the bubble with time. The bubble travels at an average velocity of 0.22 m/s in the stage of uniform movement.	110
Fig. 6.9 (a) Details of the radius in two successive periods for the bubble nearby two inclined walls in an oscillatory pressure field. (b) Details of the displacement in two successive periods for the bubble nearby two inclined walls in an oscillatory pressure field.	111
Fig. 6.10 (a) Radius of a bubble in infinite water under the oscillatory pressure actuations. (b) Displacement of a bubble in infinite water under the oscillatory pressure actuations. The bubble remains stationary in the stationary fluid (dashed line) or travels with the main stream at the stream velocity (solid line).	113
Fig. 6.11 Illustration of the real bubble and i th image bubble.	114

List of Tables

Table 5.1 Boundary conditions used in the numerical simulation.....	89
Table 6.1 The boundary conditions at the bubble and wall surfaces.	103
Table 6.2 The parameters used in the analytical model.....	109

Chapter 1 Introduction

1.1 Background and motivation

Microfluidics, which is involved in the science and technology of manipulating small amounts of fluids in networks of micro channels, has been broadly applied in different fields, such as chemistry, medicine and biology, owing to its numerous advantages of simple manipulation, high sensitivity, low cost, little sample consumption and so on [1]. Vortical flows are widely applied for flow control in many microfluidic devices, such as cell centrifuges, mixers, sorters, concentration gradient generators and reactors etc. [2-4]. However, in microfluidics the flow is usually featured with creeping flow due to the predominance of viscosity over inertia. Thus, the Reynolds number (Re) for flows is very small, leading to parallel and highly-ordered streamlines. Besides, the difficulty of vortex generation is greatly increased by the small geometric dimensions and extremely low flowrates. In fact, it is always challenging to generate vortices in microfluidic systems for applications because swirling of streamlines is suppressed by the constraints of small inertia and simple geometries.

To produce vortices, several well-designed configurations have been used in the microfluidic systems, including herringbone structures, zigzag channels, serpentine channels and flow focusing systems [2-4]. However, in these methods, the designs of the configurations are very complex and high flowrates are required. An alternative approach involves introducing external actuations, such as magnetic force, electrokinetic force, acoustic actuation, thermal effect, even external air flux etc. However, special equipment and elaborate manipulation are indispensable, which causes inconvenience in real applications. Another downside is that these methods are primarily for a specific fluid or particle with given properties. If the requirements for the flowrate or materials are changed, a new design might be needed. Therefore, despite of many kinds of vortex generators, the novel and simple methods of vortex generation and control in microfluidic systems remain to be an attractive research topic. This is one of the objectives of the present study.

Bubble dynamics in bulk flow has been intensively studied because of its applications associated with many technologies, such as ultrasonic cleaning, sonochemistry, erosion of bubble

collapse and ultrasonography [5]. Theoretical modelling of the bubble's radial oscillation probably was first conducted by Rayleigh, and Plesset extended Rayleigh's work by including liquid viscosity and surface tension, leading to the well-known Rayleigh-Plesset equation [6]. Experimental studies revealed that bubbles under external actuations not only undergo volume oscillations but also translate in space. The strong coupling between radial oscillation and translation makes it difficult to calculate the radius and displacement of a bubble under actuations. Crum and Eller obtained the translation velocity of an oscillating bubble by introducing the averaged acoustic force and drag, which was justified to be valid only in a weak pressure field [7]. Doinikov derived coupled equations for radial and translational dynamics of a bubble in infinite liquid and obtained the time-dependent radius and displacement of a bubble under high-intensity actuations [8]. In addition to oscillation and translation, an oscillating bubble in a pressure field can also experience a third type of motion – shape deformation when its volume oscillation becomes unstable. Liu et al investigated the shape stability of an encapsulated bubble in an ultrasound field and the nonlinear process of higher-order shape mode was obtained by solving the continuity equation and Navier-Stokes equation directly [9].

Recently, bubble dynamics has been widely applied in lots of microfluidic processes, such as micropumping, micromixing, sorting, flow control and manipulation of micron-sized objects etc. However, the challenges of energy concentration, viscous surface forces and low number of cavitation nuclei make it difficult to generate bubbles directly in microfluidic channels via the conventional acoustic method [10]. Alternatively, gas bubbles can be formed in microfluidic channels by introducing external gas into a flow-focusing system or through laser irradiation. However, the bubble generation by external gas and laser radiation are often inconvenient in real applications: formation of bubbles in flow-focusing systems requires introduction of external gas and elaborated manipulation; laser devices are indispensable for the method of laser radiation. New methods for bubble generation in microfluidic systems are attractive research topics in this field. Besides, most studies on bubbles dynamics under actuations in microfluidics are focused on high frequencies, ranging from 20 kHz to several MHz, while there are few investigations on bubble dynamics at low frequencies. At the low-frequency actuations, the wavelength of actuation pressure will be long compared to the bubble size and microfluidic channel, which are normally in 10^{-2} m – 10^{-4} m. As a result, the actuated pressure is almost uniformly distributed in the microfluidic channels and the pressure gradient is very small around the bubbles, leading to a

negligible primary Bjerknes force compared to high frequencies. Therefore, other mechanisms, such as the wall effects, tend to be the dominant force to propel the bubble forward under the low-frequency actuation in a microfluidic chamber.

1.2 Objectives

This study aims to investigate vortex generation, vortex control, and bubble dynamics in microfluidics with the following objectives.

- 1) To develop a novel method of vortex generation and control in a resonator-shaped microfluidic chamber with actuations.
- 2) To study bubble dynamics in a microfluidic chamber with actuations, including the bubble generation, radial oscillation and spatial translation.

The scope of this research includes:

- 1) Design and fabricate a microfluidic chamber for vortex generation and regulate the direction and intensity of the generated vortices on-demand by varying the actuation conditions, including the working transducers, frequency, voltage and flowrate.
- 2) Investigate the mechanism of the vortex generation and control in the microfluidic chamber with actuations.
- 3) Conduct experiments to study the dynamics of multi-bubbles and a single bubble in a microfluidic chamber with actuations, including the bubble generation, radial oscillation and spatial translation etc.
- 4) Conduct both numerical simulations and analytical modeling to interpret the experimental findings of bubble dynamics in a microfluidic chamber under the low frequency actuations.

1.3 Outline of the Dissertation

The following are the outlines of the present study.

Chapter 1 gives an introduction to the research, including background, motivation and objectives of the present study.

In Chapter 2, literature review is conducted on microfluidic vortex generators, cavitation and bubble dynamics in bulk liquid and microfluidics.

Chapter 3 presents a novel microfluidic chamber with piezoelectric actuations for vortex generation. Fabrication of the microfluidic chamber and experimental visualization are described in detail. The effects of the actuation conditions including the frequency, voltage and flowrate are investigated.

Chapter 4 studies modification of the microfluidic chamber by separating the transducer into two parts. The direction and intensity of the generated vortex in the chamber are regulated by varying the actuation conditions.

Chapter 5 investigates the dynamics of multiple bubbles in the microfluidic chamber with low-frequency actuations. The phenomena of bubble coalescence and breakup are observed. Numerical simulation is carried out to investigate the mechanisms of the bubble dynamics based on the pressure variation and distribution inside the chamber.

In Chapter 6, the dynamics of a single bubble is studied experimentally and analytically. Radial and translational motions of the bubble in the chamber are quantitatively analyzed by measuring the recorded images. An analytical model is constructed by using the Lagrangian mechanics and the method of images and the analytical results are compared with the experimental observations.

Finally, Chapter 7 summarizes the main conclusions and contributions of the present research and gives some recommendations for future research.

Chapter 2 Literature Review

2.1 Introduction

Vortex structure is a prevalent feature in most macro hydraulic flows. Many great figures such as Helmholtz, Kelvin, Prandtl and von Karman, all made substantial contributions to vortex flows in hydrodynamics [11-13]. Up to date, Karman Vortex Street and Taylor vortex are favorable tools to investigate the instability of fluid flows and transition from laminar to turbulence. In microfluidics, due to the low flowrates and small dimensions, viscous force is dominant relative to inertia, which makes it a great challenge to generate vortices in micro-scaled channels. To produce vortex in microfluidics, special design or external disturbance must be introduced to disrupt the highly-ordered streamlines [2-4]. The methods of generating vortices in microfluidics can be categorized into passive and active according to whether external forces are used. Passive methods rely on well-designed geometries and special flow conditions, while active methods require external forces. According to the external forces, the main classes of active vortex generators are electrokinetic generators, magnetic generators, and acoustic generators and so on. Active methods have fewer limits on flow conditions and higher efficiency in contrast to passive methods.

Cavitation, which is defined as rupture of liquid, is widely applied in many areas such as engineering and medicine. The radial response of a cavitation bubble can be described by the well-known Rayleigh-Plesset equation and its extensions, which consider various factors, for instance, damping effects, heat and mass transfer across the interface between liquid and gas, and the liquid compressibility etc. Under weak external actuation, the bubble undergoes linear oscillation; while under strong actuations, the bubble oscillates nonlinearly with violent contraction and even collapse. The bubbles under external actuations not only undergo volume oscillations but also move in space – translate, and the translational dynamics of an oscillating bubble is highly coupled with radial pulsation, which is a challenge for researchers to study the bubble's motions. The challenges of energy concentration, viscous surface forces and low number of cavitation nuclei make it difficult to generate bubbles directly in microfluidic channels via the conventional method. Pulsed laser radiation can provide enough energy to

evaporate the liquid to generate bubbles, but the generated bubbles are usually transient, and more frequently external gas needs to be introduced into a flow-focusing system to create bubbles.

This chapter presents a literature review on microfluidic vortex generators, cavitation phenomenon and bubble dynamics in bulk liquid, and bubble dynamics in microfluidics, including the bubble's radial pulsation and translation. The research gap of current investigation is also summarized.

2.2 Microfluidic vortex generator

2.2.1 Vortex in microfluidics

Vortices form prominent features in most natural flows, such as atmospheric vortices in tornadoes, whirlwinds of dust or leaves, smoke rings and ocean currents. Fluid vortices are also central factors of consideration in many industrial flows: centrifugal separators used in chemical engineering processes, tip vortices generated by wings, wakes of ships and so on.

Although the notion of a vortex is so widely used in fluid dynamics, few researchers can give an exact and inclusive definition of vortex. Several authors have proposed rigorous definitions of vortex. Brachet et al. [14] defines a vortex as a region of negative velocity gradient determinant. Babiano et al. [15] defines a vortex as any domain of a fluid with vorticity greater than a critical value. However, no single definition has gained broad acceptance. Herein, we do not explore deeply the exact mathematical definition of a vortex, but accept the simple and visible description: any type of swirling flow with closed or spiraling streamlines [16].

Vortical flows are widely applied for flow control in many microfluidic devices, such as cell centrifuges, mixers, sorters, concentration gradient generators and reactors etc. However, due to small channel dimensions and low flowrates, the flows in microfluidics tend to be laminar and dominated by viscosity of the fluids. Thus, it is always challenging to generate controllable vortices in microfluidic systems for applications. To produce vortices, several well-designed configurations have been used in the microfluidic systems including herringbone structures, zigzag channels, serpentine channels and flow focusing systems, and this is so-called passive method. An alternative approach, active method, can effectively generate vortical flows with

lower flowrates. It involves the introduction of external actuations, such as electrokinetic force, magnetic force, acoustic actuation, thermal effect, and even external air flux etc.

Next, we will discuss the two typical microfluidic vortex generators in detail.

2.2.2 Passive vortex generators

The passive vortex generators rely on the advection flow caused by complex configurations and geometries of the microchannels, such as herringbone structures, zigzag turns, serpentine channels and flow focusing systems and so on. In this section, the current study of passive vortex generators is briefly reviewed.

Stroock et al. [17] presented the earliest passive vortex generator to mix fluids under certain flow conditions. As illustrated in Fig. 2.1, two types of vortex generators are designed by introducing different ridge arrays at the bottom of the channel. One type is featured with sloped ridges as shown in Fig. 2.1(a) and the other with staggered herringbone ridges as shown in Fig. 2.1(b). Both microstructures can generate vortices under high enough Reynolds number (Re). For example, the staggered herringbone structure (Fig. 2.1(b)) resulted in the vortex flow at Re of about 100.

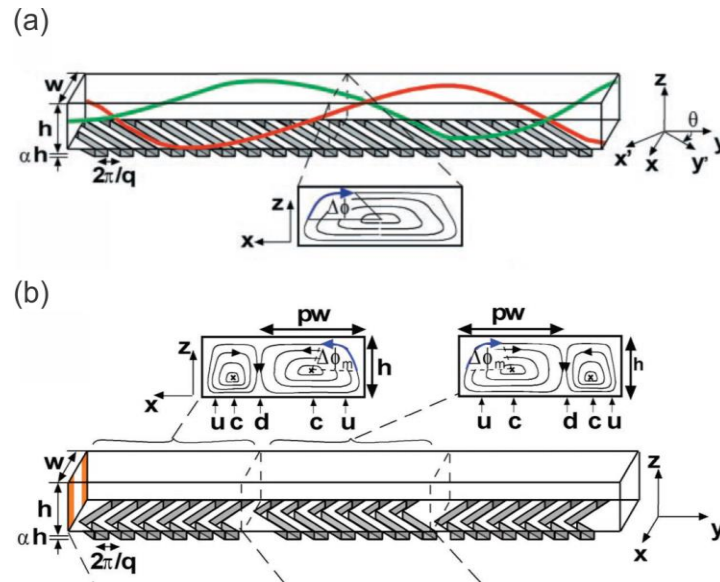


Fig. 2.1 Illustration of vortex generators with ridge arrays and generated vortices in microchannels. (a) sloped ridges; (b) herringbone ridges. [17]

Mengeaud et al. [18] designed a zigzag microchannel integrated with “Y” junctions (Fig. 2.2(a)), which can generate vortices at the corners. They found that below a critical Re of about 80, the flow profile remains parabolic indicating existence of a laminar flow; for higher Re , the occurrence of vortices at the corners is possible. It is observed that the vortices in Fig. 2.2(b) occupied the entire arms of the channel after each angle at $Re=267$.

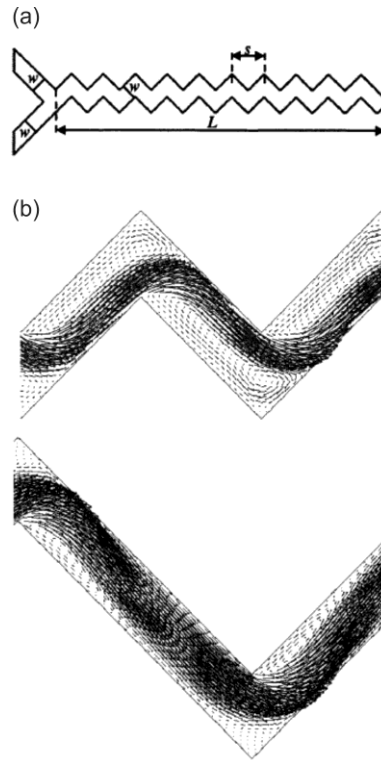


Fig. 2.2 (a) Dimensions of the vortex generator integrating “Y” junctions with zigzag microchannels. (b) Velocity vectors obtained at $Re=267$ for zigzag geometries. [18]

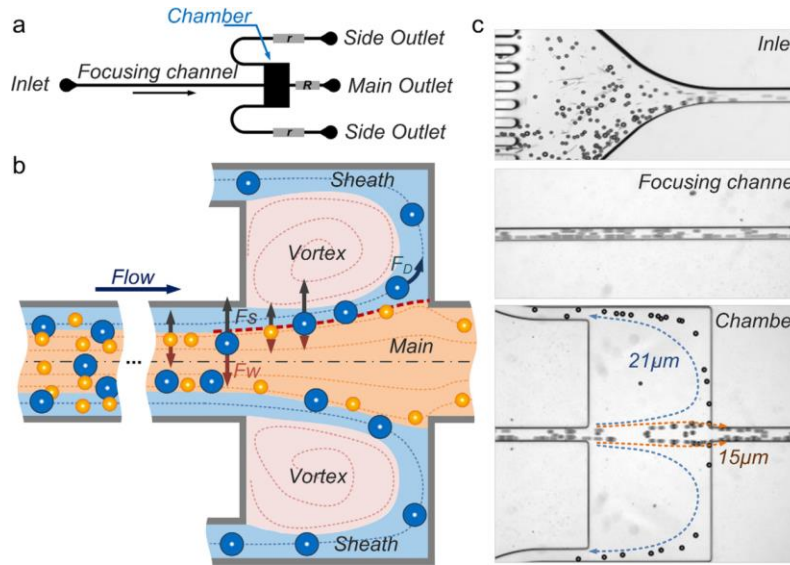


Fig. 2.3 (a) Schematic illustration of inertial vortex generator. (b) Illustration of the separation principle. The symmetric vortices are indicated by the red dashed lines. (c) Stacked images at various downstream positions illustrating the separation phenomenon at $Re=110$. [19]

Wang et al. [19] proposed an inertial vortex generator with simple geometries for cell extraction. The configuration of the device, the principle of separation and experimental images are shown in Fig. 2.3. The design takes advantage of symmetric vortices generated in a high-aspect-ratio microchannel to separate cells.

Oliveira et al. [20] reported the formation of free vortices through a microfluidic flow-focusing system. The device is shaped like a cross-slot and comprises three entrances and one exit. Figure 2.4 shows the flow patterns for varying Re at the channel's center plane using streak photography. Vortices are obtained both in numerical calculations and experimental observations when Re is equal to 94.2 (Fig. 2.4(c)) or 113 (Fig. 2.4(d)).

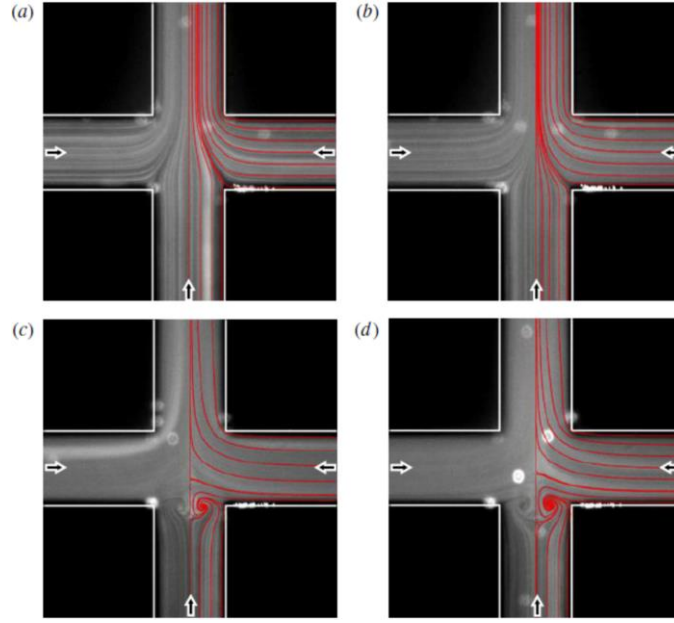


Fig. 2.4 Flow patterns in the 3D flow-focusing geometry for varying Re . Comparison between experimental (grey-scale images) and numerical pathlines at the centre plane. (a) $Re=2.8$; (b) $Re=6.5$; (c) $Re=94.2$; (d) $Re=113$. [20]

Liu et al. [21] reported a three-dimensional serpentine channel which consists of periodic units with a “C-shaped” structure to produce vortices. In this type of channel, strong vortices can only be generated at relatively high Reynolds numbers ($Re = 70$) when the flow patterns become complicated by combined effects of rotational and backward flows. Vortex generation in a passive way is also widely investigated by other researchers such as Singh et al. [22], Kang et al. [23], Simonnet et al. [24] and Camesasca et al. [25] and so on.

Although passive method is easily-manipulated and low cost, it needs a complex geometry design and very high Reynolds number. If changes are induced to either the velocity or materials, a new optimized design might be needed.

2.2.3 Active vortex generators

Vortex can be generated by an external energy input to introduce the perturbation of fluid streamlines in a microfluidic device, which is the so-called active method. Active vortex generators are categorized with respect to the type of external forcing. In this section, we will discuss active vortex generators in microfluidics based on the type of external actuations.

2.2.3.1 Electrokinetic method

Electrokinetic forcing serves as an effective means not only for liquid pumping but also for flow control. For example, electroosmosis is widely used due to its significant advantages such as plug-like velocity profile, ease to control and no mechanical moving parts. Squires and Bazant [26] reported a type of electrokinetic flow called induced-charge electroosmosis (ICEO), which can generate flow circulations near a highly polarizable conducting object in an external electric field. Wu and Li [27] obtained an irregular flow field with micro vortices by means of ICEO flow in experiments and simulations. Figure 2.5 shows the comparison of the flow fields for the case with and without ICEO effect. Clearly, with the presence of ICEO effect, a pair of vortices is generated before and after the throat of the channel, respectively.

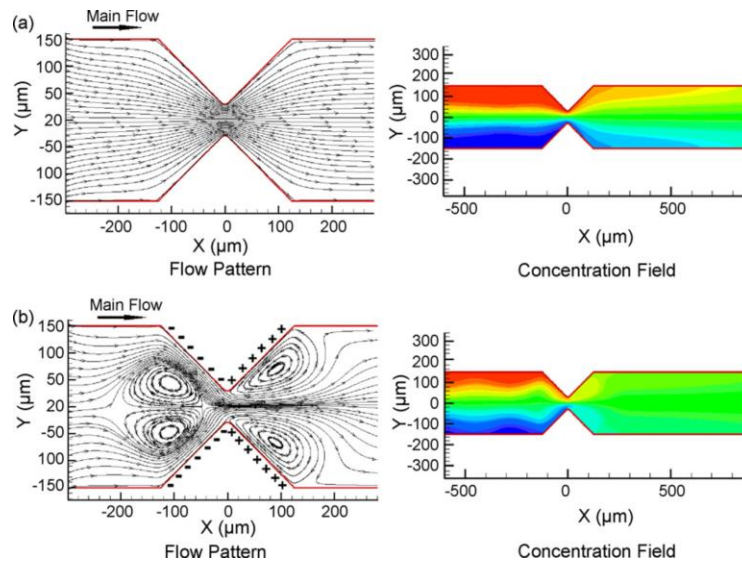


Fig. 2.5 Flow patterns and concentration fields (a) with induced-charge electroosmosis effect and (b) without induced-charge electroosmosis effect. [27]

Developments in fabrication of microelectrodes have intrigued new methods of generating vortices in microfluidics. Wu and Liu [28] reported a vortex generator with the electrodes embedded in the herringbone structure of a T-shaped channel's bottom wall. Sasaki et al. [29] demonstrated a vortex generator due to a meandering electrode pair on the bottom of the "Y" channel, around which electroosmotic flow is created. More complex patterns of microelectrodes on the channel walls were also proposed by Huang et al. [30].

Vortices can also be generated in an opto-electrofluidic platform, which combines a focused laser beam with alternating current (AC) electric fields. In the presence of electric fields, the use of intensive laser irradiation can produce strong vortices in a microchannel formed by two plates, due to a combination of electrothermally-induced flows and electrohydrodynamically-induced flows. Kumar et al. [31] reported the first opto-electric vortex generator in microfluidics when a near-infrared laser beam is focused in a microchannel with an AC electric field. Park and Wereley [32] demonstrated an opto-electric vortex generator with two coplanar electrodes, which can generate twin opposing microvortices (TOMVs). The configuration is different from the design of Kumar, as shown in Fig. 2.6: two electrodes A and B are located on the same surface of the microchannel. When the laser spot is focused on any region of the exposed electrode, a vortical flow is generated rapidly (Fig. 2.7). The motion is a complex, three-dimensional vortex flow but remains steady in time. The pattern and direction of twin vortices are controllable by positioning of the laser radiation on the electrodes. This technique is a promising method to produce desirable fluid flows and manipulate chemical and biological fluids in microfluidics.

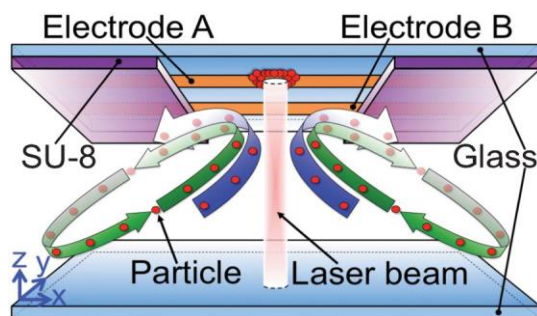


Fig. 2.6 Schematic illustration of the TOMV (twin opposing microvortices) flow with two microvortices (circular arrows) generated by the laser radiation and two coplanar electrodes on the top surface of the microchannel. [32]

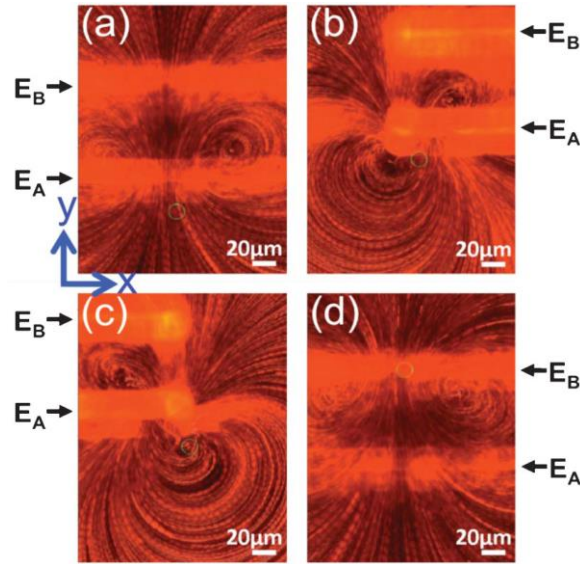


Fig. 2.7 Stacked images showing various microvortical flows in terms of the location of the laser spots on two electrodes. The laser spot is focused at the middle (a), left side (b), right side (c) of exposed electrode A, and (d) middle of exposed electrode B. [32]

2.2.3.2 Acoustic Method

Vortices can be achieved by means of acoustic actuation, which is introduced into the channel by integrated piezoelectric ceramic transducers (PZT). Air bubbles can be introduced in a microfluidic channel and the surface of the air bubbles in liquid exposed to a sound field can function as a vibrating membrane, which causes a bulk fluid movement at the air–liquid interface. This effect, known as cavitation microstreaming, has been applied in microfluidic vortex generation by a single bubble or an array of bubbles.

The first research on acoustic streaming induced by air bubbles is conducted by Liu et al. [33]. A number of air pockets were used for trapping air bubbles and a PZT disk is attached onto the wall of the channel. When an integrated PZT actuator is switched on, acoustic streaming was induced by the vibration of bubbles, resulting in steady vortices around the bubbles. Ahmed et al. [34] designed a single-bubble-based vortex generator by trapping an air bubble within a “horse-shoe” structure located between two laminar flows (Fig. 2.8). Acoustic waves induce the vibration of the trapped air bubble at its resonance frequency, resulting in acoustic streaming. Figure 2.9 shows the visualization of flow patterns near an acoustically excited microbubble trapped in a horse-shoe structure. The particle was nearly motionless prior to the acoustic agitation; as the air bubble was excited, a pair of counter-rotating vortices extended from the

frontside to backside of the horse-shoe structure, which is made visible through the trajectories of particles.

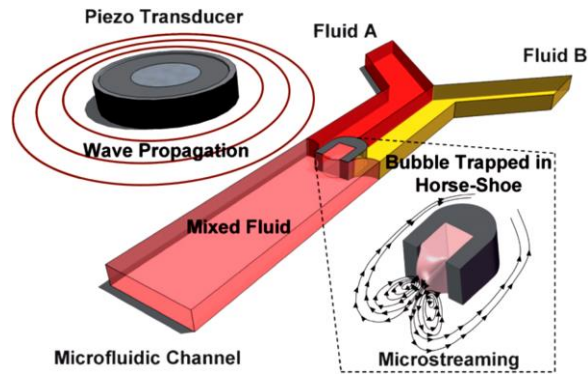


Fig. 2.8 Schematic of experimental setup for an acoustic vortex generator. The transducer is positioned adjacent to the channel; a bubble is trapped inside the horse-shoe structure. [34]

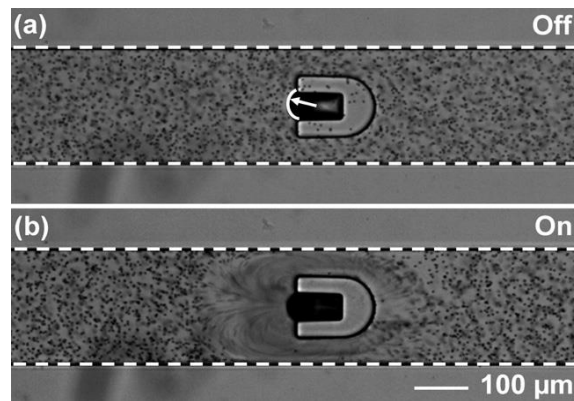


Fig. 2.9 Characterization of the flow pattern around a single bubble. (a) An air bubble trapped in the horse-shoe structure and stationary particles in the fluid. (b) Vortices around the air bubble when the bubble membrane oscillates at its resonance frequency. [34]

Hilgenfeldt et al. [35] investigated the frequency dependence of the vortices of an oscillating bubble in microfluidics, driven by the ultrasounds in the frequency range between 1 kHz and 100 kHz. The oscillation modes and flow patterns are shown in Fig. 2.10. They further developed a complete asymptotic theory to calculate the streaklines of the fluid flow from cylindrical bubbles and the theoretical results are found to be agreeable with experimental observations [36].

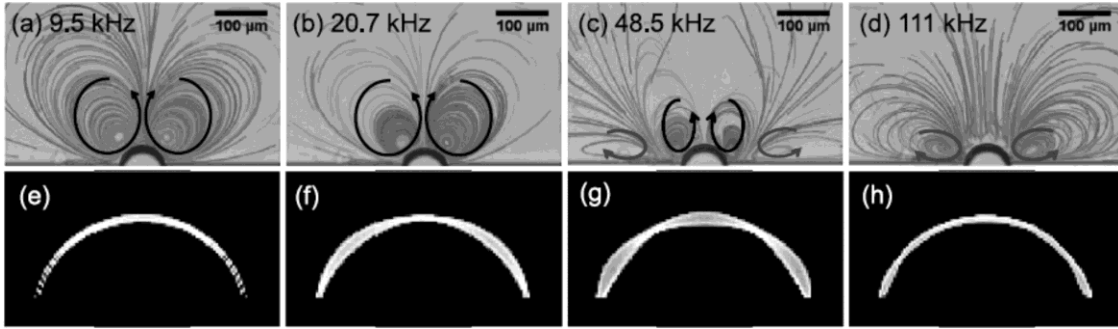


Fig. 2.10 A pair of vortices generated by the bubble oscillation at different driving frequencies (a-d). Outline of the oscillatory bubble superposed over one cycle at different frequencies (e) 9.6 kHz, (f) 20.6 kHz, (g) 48.6 kHz, and (h) 100.3 kHz. [35]

2.2.3.3 Other types of active methods

Vortex can be achieved by stirring of magnetic particles suspended in the fluids [37]. When the scattered paramagnetic particles are exposed in a magnetic field, they tend to align in a chain, which is effective in fluid stirring for vortex generation. Calhoun et al. [38] and Franke et al. [39] verified the feasibility of this method of vortex generation using a rotating magnet and magnetic chains by simulations and experiments, respectively.

Thermal disturbance can also act as the driving force to produce vortices in the microfluidic channels. Kim et al. [40] created multi-vortices by using the natural convection in conjunction with alternating heating and the resultant vortical flow is successfully used for micromixing and polymerase chain reaction (PCR) tests (Fig. 2.11).

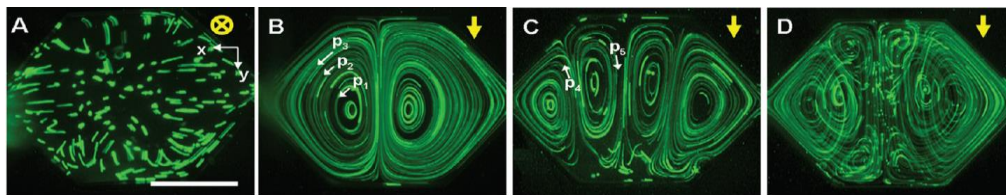


Fig. 2.11 The natural convection-driven flows in a microfluidic chamber. (A to D): trajectories of fluorescent particles in time sequences. [40]

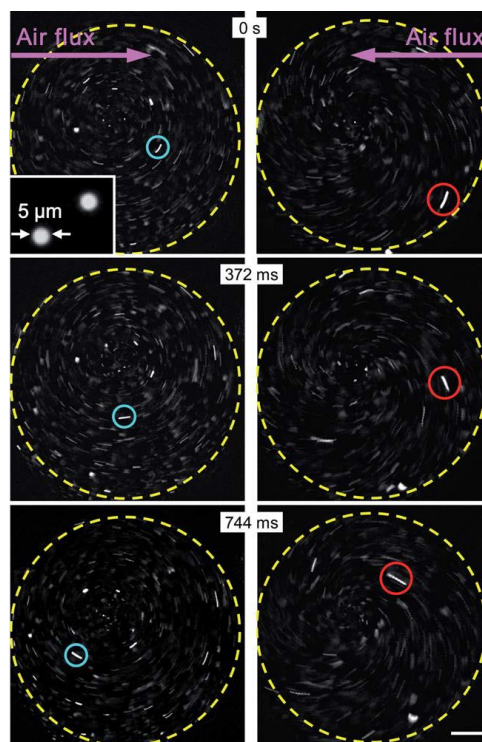


Fig. 2.12 Fluorescence images of microparticles during agitation. The flow can be directed in a clockwise (left-hand panels) or counter-clockwise (right-hand panels) fashion. [41]

Geissler et al. [41] use air flux to induce spiral motions in a small-scale fluid domain by means of a convenient and efficient manner. The air flux is regulated and projected onto a liquid-containing reservoir, which leads to spiral motions of the fluid in the reservoir. A suspension of microbeads follows the spiral motion of the liquid and thus visualizes the flow pattern in the reservoir. As shown in Fig. 2.12, the generated vortex can be either clockwise (left-hand side) or counter-clockwise (right-hand side), depending on the orientation of the incoming air in the supply channel.

Active vortex generators have fewer limits on flow conditions and higher efficiency than passive vortex generators. However, some active methods are primarily for specific fluids or particles with given properties, and the special equipment and elaborate manipulation are also indispensable. For example, the electrokinetic or magnetic actuation has requirements on the conductivity or magnetism of the working fluids. The thermal method may damage the reagents and samples which are sensitive to the temperature variation; the general acoustic methods need to introduce and trap external gas in advance and there is also a problem of temperature rise at high frequency.

2.3 Cavitation inception and thresholds

Cavitation is a very common phenomenon that occurs in a fluid flow system. It refers to the process of nucleation from liquid to gas phase when pressure falls below some critical value, mostly vapor pressure, at almost constant temperature. From a basic physical viewpoint, cavitation has no difference from boiling. Rupture of a liquid leading to gas phase is the main feature in both cavitation and boiling. Cavitation can be further subdivided into hydrodynamic cavitation – rupture in a low or even negative pressure zone of a liquid flow and acoustic cavitation – rupture in sound fields. Apfel [42] initially denominated acoustic cavitation to be formation of a vapor cavity or bubble in response to an acoustic pressure field, but in most circumstances, the bubble which is activated by a sound field is observed to not simply form from bulk liquid but grow from some pre-existing nuclei in liquid. Therefore, the cavitation phenomena might be thought of as the process of creation of new bubbles or expansion/contraction/distortion of pre-existing ones in a liquid, which is coupled to the pressure fluctuation.

2.3.1 Cavitation nuclei as bubble sources

The existence of nuclei in liquid such as water can be expected. Those nuclei are of size between a few microns and some hundreds of microns and operate as starting points for cavitation. In addition to cavitation, the consideration of nuclei inside a homogeneous liquid is common in thermodynamics, for example, boiling, condensation and solidification. It is thought that there are three types of nuclei [43]: some nuclei are freely suspended in liquid; some are trapped in crevices of the walls; many nuclei are also attached to solid motes in liquid. New populations of nuclei can also be generated by larger bubbles that undergo breakup or splitting.

An excess pressure would be imposed to the bubble surface due to the existence of surface tension, which is called surface tension pressure. Under this pressure, bubbles tend to dissolve because the concentration gradient occurs between the bubble wall and infinity. However, the experiments show that in real liquids free nuclei exist after long time [44-45]. Besides, when an external actuation such as a sound field is acting, the oscillation of bubbles can counteract the dissolution from surface tension and bubbles can grow remarkably over long periods of time.

Tensile strength is the largest tension which a liquid can suffer without cavitation, which is equal to the hydrodynamic cavitation threshold of liquids. Considering the cohesion between two liquid molecules, the theoretical tensile strength of pure liquids is remarkably large. Caupin predicts [46] that for pure water at 300 K, the tensile strength is about 128 MPa, beyond which the nucleation of the vapor phase can take place. However, in real liquid, lots of nuclei exist, which are generally of the magnitude of micron-size. Typically, nuclei or microbubbles, which are freely suspended or attached to solid boundaries or motes, act as starting points of cavitation and limit the tensile strength of liquids. Therefore, the real liquid can suffer much smaller tension and even will be nucleated at positive pressure.

The tensile strength or cavitation threshold is often not the property of the pure liquid, but highly depends on the degree of cleanness of the liquid, such as the number of impurities, motes and pre-existing nuclei. The tap water without any further processing begins to be nucleated at even positive pressure - saturated vapor pressure, and no tension occurs in liquid. Herbert et al. [47] reported that, after ultrapure water is treated through a series of rigorous cleaning procedures, the tension strength is found to be 26 MPa at 0 centigrade and 17 MPa at 80 centigrade. Because the tensile strength of laboratory water is greatly less than theoretical prediction, it can be expected that the cavitation can occur easier than “ideal” liquids.

2.3.2 Cavitation threshold

2.3.2.1 Blake threshold

When the ambient pressure is varied to P_∞ , one can expect that the bubble radius is evolved to R from R_0 . In new equilibrium, the pressure inside a bubble consists of gas and vapor, P_i , is

$$P_i = P_g + P_v = P_\infty + P_\sigma \quad (2.1)$$

where P_g , P_v and P_σ are the gas pressure, vapor pressure and surface tension pressure, respectively. Assuming that the variation is slow enough for isothermal process of the gas, the evolution of R can be obtained

$$\left(P_{\infty,0} + \frac{2S}{R_0} - P_v \right) \left(\frac{R_0}{R} \right)^3 + P_{v,0} = P_\infty + P_\sigma \quad (2.2)$$

where S is the surface tension and the subscript 0 denotes the initial state.

If the external pressure is lowered to a critical value, there is no possible equilibrium radius R . Beyond this pressure, the bubble will expand to a multiple of its initial size and collapse violently afterwards. The critical pressure, which depends on R_0 , is called “Blake threshold” [48]. It can be calculated by seeking the minimal R from the above equation [49]

$$P_{\infty}^{crit} = P_0 - P_0 \left(\frac{4}{27} \frac{X^3}{1+X} \right)^{1/2} \quad (2.3)$$

where P_0 is the ambient pressure and $X=2S/P_0R_0$. In an oscillatory pressure field, this expression also determines the minimum actuation pressure, beyond which nuclei will cavitate, grow explosively and collapse violently. Therefore, this is the threshold for inertial cavitation, beyond which stable cavitation cannot occur.

2.3.2.2 Rectified diffusion threshold

Consider a gas bubble undergoing radial oscillation in a liquid with dissolved gas. During the expansion phase of a cycle, the gas tends to enter the bubble while the bubble loses gas during the contraction phase. Hence, the concentration gradient of the dissolved gas will oscillate in liquid, resulting in a pulsating diffusion flux. On average, the net flux within one cycle is non-zero. Although during one cycle, the net flux is very small, diffusion may cause bubbles to grow over long periods of time. This phenomenon of gas accumulation in the bubble over many cycles is referred to “rectified diffusion” or RD [45]. Young [50] proposed the detailed explanations: Firstly, gas diffusion from liquid to the bubble occurs when the area of exchange is larger during the expansion phase of a cycle; secondly, the diffusion boundary layer is thinner during the expansion phase and thus incur a higher inward flux.

An oscillating bubble grows because of rectified diffusion while surface tension promotes the dissolution. A competition takes place between two effects and there exists a threshold for a nucleus to grow or dissolve. For weak oscillation, nuclei will dissolve or remain inactive with the action of surface tension; while under strong actuation, nuclei can aggregate the gas in liquid and become active bubbles over long time. The expression for the RD threshold is proposed by Hsieh and Plesset [51]

$$\frac{P_a}{P_0} = \sqrt{\frac{3}{2} \left[1 - \frac{C_{\infty}}{C_0} \right] \left(1 + \frac{2S}{R_0 P_0} \right)} \quad (2.4)$$

where P_a is the amplitude of pressure fluctuation, C_∞ is the gas concentration in the liquid and C_0 is the saturation gas concentration in the liquid. It applies only to bubbles well below resonance size, and above the threshold, nuclei can grow to become active.

2.3.2.3 Transient threshold

Transient cavitation can be qualitatively distinguished from stable cavitation by whether the bubble is fragmented or dissolved during one period. However, to define the threshold exactly, the transition from stable to transient cavitation can be stated quantitatively in terms of the maximum radial velocity of the bubble surface. When this velocity reaches the sound speed in liquid, that is, Mach number approaches 1, we specify that transient cavitation occurs. In incompressible liquid, a gas bubble which reaches a collapse velocity equal to sound speed will grow to a maximum radius, R_{max} , about 2 times its original size. According to this criterion, Neppiras [52] introduced the expression of the transient threshold

$$P_a = P_0 + \frac{4}{3} \left[\frac{2S^3}{3R_0^3(P_a + 2S/R_0)} \right]^{1/2} \quad (2.5)$$

where P_a is the amplitude of pressure variation, S is the surface tension, P_0 is the ambient pressure and R_0 is the initial radius of the bubble.

The RD threshold is usually regarded as the beginning point for a stable cavitation because below it, the microbubble will be inactive and dissolved afterwards. If a nucleus grows over long time above RD threshold, it may undergo inertial cavitation when reaching Blake threshold. If the pressure amplitude become larger or the bubble grows larger, the bubble can suffer transient cavitation, undergoing fragmentation after violent collapse.

2.3 Radial dynamics of a bubble in liquid

Conventionally, the oscillation of a bubble can be qualitatively classified according to the magnitude of the bubble's vibration in response to the imposed actuations. In general, three regimes are identified [53].

a) Linear oscillation exists under very small pressure amplitudes. The radial oscillation of a bubble is non-linear in nature. However, actuated under low amplitude pressure, the bubble's response is weak oscillation around equilibrium radius and can be regarded as linear.

b) With increasing amplitude of oscillating pressure, the response of a bubble will become featured with weak nonlinearity and slight inertia effect. However, the bubble may still oscillate stably, which can be referred as “stable cavitation”.

c) Under a strong enough pressure field, the bubble size may vary by several orders of magnitude during one cycle. The bubble will experience explosive growth followed by violent fragmentation. Such a response is termed to be “transient cavitation”.

Current experiments show that stable bubbles can also exist under such kind of cavitation – “inertial cavitation”, one of which is the sonoluminescence bubble [54]. Inertial cavitation, which was termed as transient cavitation in the past, is separated independently since the sonoluminescence bubble experiences violent collapse but without fragmentation or dissolution. The cavitation phenomena with low frequencies (in the audible domain and below) approach hydrodynamic cavitation in a way. Nevertheless, the classification of cavitation at low frequencies complies with the same law with the cavitation at high frequencies.

2.3.1 Rayleigh-Plesset equation and extensions

The analysis of cavitation and bubble dynamics was firstly made by Rayleigh, who solved the collapse of a spherical cavity in infinite liquid with the assumption of isothermal change. In 1949, Plesset improved this equation by including the effects of surface tension and viscosity, and obtained the famous Rayleigh-Plesset equation [6]

$$R\ddot{R} + \frac{3}{2}\dot{R}^2 = \frac{P_i - P_\infty}{\rho} - \frac{4\nu_L\dot{R}}{R} - \frac{2S}{\rho R} \quad (2.6)$$

where, over-dots represent the time derivative, ρ is the liquid density, P_∞ is the ambient pressure in liquid, P_i is the pressure inside the bubble, S and ν_L are the surface tension constant and kinetic viscosity of the liquid, respectively.

For a mixture bubble composed of permanent gas and vapor of surrounding liquid, the interior pressure is calculated by Eq. (2.1). Assuming that the gas in the bubble is polytropic so that when the bubble has radius R , the partial pressure of the gas will be:

$$P_g = P_{g,0} (R_0/R)^{3\kappa} = (P_0 + 2S/R_0 - P_v) (R_0/R)^{3\kappa} \quad (2.7)$$

where, $P_{g,0}=P_0+2S/R_0-P_v$, the gas pressure at equilibrium and κ is polytropic index, clearly, $\kappa=1$ for isothermal process and $\kappa=\gamma$ (the ratio of the gas specific heat) for adiabatic behavior.

In a pressure field, the pressure P_∞ is transient, for example, sinusoidal driving, and it can be written as

$$P_\infty = P_\infty(t) = P_0 - P_a \sin(\omega t) \quad (2.8)$$

where P_0 is the static ambient pressure and P_a is the amplitude of driving pressure and ω is the angular frequency. The driving frequency $f = \omega/2\pi = 1/T$, where T is the driving period.

Therefore, substituting Eqs. (2.7) and (2.8) into Eq. (2.6), an extension equation, which describes the radial dynamics of an oscillating mixture bubble in liquid, follows

$$R\ddot{R} + \frac{3}{2}\dot{R}^2 = \frac{P_v - P_0}{\rho} - \frac{4\nu_L \dot{R}}{R} - \frac{2S}{\rho R} + \frac{Pa \sin(\omega t)}{\rho} + \frac{1}{\rho} (P_0 + \frac{2S}{R_0} - P_v) (\frac{R_0}{R})^{3\kappa} \quad (2.9)$$

where, all the symbols are defined above.

This extension of Rayleigh-Plesset equation is termed as RPNP (Rayleigh Plesset Noltingk Neppiras Poritsky) equation and was first derived by Poritsky [55]. When we discuss bubble dynamics in pressure fields in the next part, this equation is referred to Rayleigh-Plesset equation or Rayleigh-Plesset model without ambiguity.

The compressibility of the liquid can be neglected when the characteristic length of the bubble (the radius R) is much smaller than the wavelength of the applied pressure field, $\lambda = c/f$, where c is the sound speed in the liquid. However, for high frequencies, compressibility of the liquid needs to be considered and the Rayleigh-Plesset equation for a permanent gas bubble becomes the so-called Gilmore model [56] which is well suited to the situation that compressibility of liquid plays an important role under high pressure. Different from the Gilmore model which assumed a pressure dependent sound speed, Keller and Miksis assumed that the velocity potential around a bubble in acoustic fields satisfies the spherical wave equation with constant sound speed [57]. Both Gilmore model and Miksis model are extensions of Rayleigh-Plesset equation with similar form. The connection between the different models of bubble dynamics is investigated by Prosperetti and Lezzi [58].

2.3.2 Linear oscillation of a bubble in oscillatory pressure fields

The bubble's oscillation is nonlinear in essence. However, when the actuation pressure field is very weak with small amplitude, the bubble can respond with small oscillations around its equilibrium radius. In this sense, the bubble/liquid system can be regarded as a linear oscillator, similar to a mass-spring system with a periodic force.

The Rayleigh-Plesset equation (2.9) is used to analyze the linear response of a bubble in a pressure field with a small amplitude P_a and frequency ω . When thermal and compressible effects are neglected, we can get a linear relation between the complex amplitude of the bubble radius ϕ and the driving pressure P_a [59]:

$$\phi = \frac{P_a}{\rho R_0^2 (\omega_n^2 - \omega^2 + 4j\omega\nu_L / R_0^2)} \quad (2.10)$$

where R_0 is the equilibrium radius at the pressure P_0 and $R_0|\phi|$ is the amplitude of the bubble's oscillation and the phase of ϕ is the phase difference between P_∞ and R , ν_L is the kinetic viscosity. From Eq. (2.10), we are ready to draw the conclusions that [59]

For $\omega < \omega_n$, the bubble radius is out of phase with the driving forces, which means that the bubble will expand during the depression of the pressure.

For $\omega > \omega_n$, the bubble will be in phase with the driving forces, which sounds impossible because it means that the bubble will contract as the exerted forces increase. This case occurs due to the predominance of the liquid inertia at high frequency.

2.3.3 Nonlinear oscillation of a bubble in oscillatory pressure fields

The preceding section assumes that the perturbation of the bubble's radius is small enough to keep the linear response. However, this approximation is questionable in real cases because the bubble can exhibit a lot of nonlinear phenomena as reviewed by [60]. As the amplitude increases, the bubble may experience the process from stable cavitation to transient cavitation.

The governing equation of an oscillating bubble at infinity is a nonlinear ordinary differential equation, including Rayleigh-Plesset model, Gilmore model or Miksis model. It's difficult to solve the equation directly; however, with the progress of computer science, it's possible to obtain the solution numerically.

An example of bubble dynamics calculated by Rayleigh-Plesset equation is presented in Fig. 2.13 by Vignoli et al [61]. A bubble with initial radius of $2\text{ }\mu\text{m}$ is driven by a sound field of 1.42 atm pressure amplitude and 26.5 kHz . The surface tension and viscosity are 72.8 mN/m and $1.002\text{ mPa}\cdot\text{s}$, respectively, while the compressibility is not considered. By solving Rayleigh-Plesset equation, Hilgenfeldt et al. [62] investigated the role of liquid viscosity on bubble oscillation. They found that the maximum radius in a cycle decreases with increasing viscosity; viscosity, as damping, prevents the bubble from violent collapse and afterbounces and above some threshold, the bubble cannot obtain collapse strong enough for ignition of sonoluminescence.

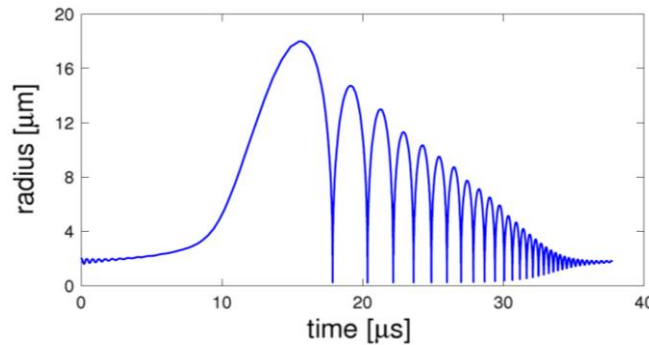


Fig. 2.13 Radius as a function of time for one cycle of the motion of a bubble of $2\text{ }\mu\text{m}$. The bubble dynamics is described by the Rayleigh–Plesset equation. [61]

When a small bubble is encountering external actuations with increasing pressure, inertial cavitation will emerge instead of stable cavitation. Lauterborn and Mettin [63] investigated this transition process of regimes of bubble oscillation by calculating the radius of a $1\text{ }\mu\text{m}$ bubble driven at 20 kHz and increasing pressure by Keller-Miksis model. As shown in Fig. 2.14, the transition from stable to inertial cavitation with increasing pressure is clearly displayed: the maximum radius during one period increases suddenly with a subtle ascent of driving pressure. The upper curve (solid line) shows the typical feature of inertial cavitation which includes explosive growth of the bubble and a steep collapse with a series of afterbounces. During this process, the bubble motion is mainly governed by liquid inertia, which is the reason for the term “inertial oscillation”. Inertial cavitation is in the region of sonoluminescence experiment and has the characteristics of a large excursion followed by an extremely steep collapse with a series of

afterbounces. The radial dynamics of bubble clusters are also studied by researchers by different models, such as volume-averaged equations [64] and ensemble-averaged equations [65].

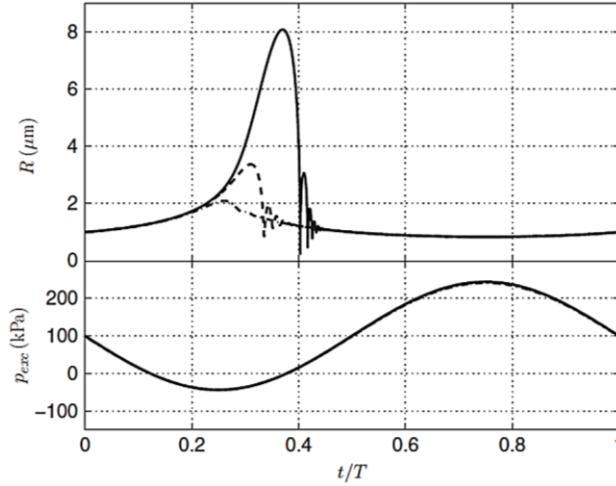


Fig. 2.14 Upper graph: Radius-time curve of an oscillating bubble calculated by Miksis model. Bubble radius at rest $R_0=1 \mu\text{m}$, driving frequency $f=20 \text{ kHz}$ and the pressure amplitude $P_a=142 \text{ kPa}$ (dash-dotted line), 143.5 kPa (dashed line), and 144 kPa (solid line). [63]

In addition to numerical simulation, experiments have been extensively conducted about bubble dynamics to verify the theoretical models and other predictions.

Gompf and Pecha [66] used light scattering method to record the dynamics of a single air bubble in an oscillatory pressure field in water and made comparison of the radius-time curves between measurement and calculation for different driving pressures. The calculation model is based on RP equation. The agreement between experimental result and theoretical model is remarkable except for the afterbounces of the bubble. Lauterborn et al. [67] made more agreeable comparison between experimental result and numerical calculation. They recorded one complete cycle of an oscillating bubble of $8.1 \mu\text{m}$ radius driven by the external actuation of 21.4 kHz for frequency and 132 kPa for amplitude. The dependence of the bubble radius on time from experiments is derived from the images. It is observed in Fig. 2.15 that the bubble shows typical features of inertial cavitation, expanding slowly and shrinking with a fast collapse and several afterbounces. Within the error of measurement, the experiments coincide quite well with numerical calculation.

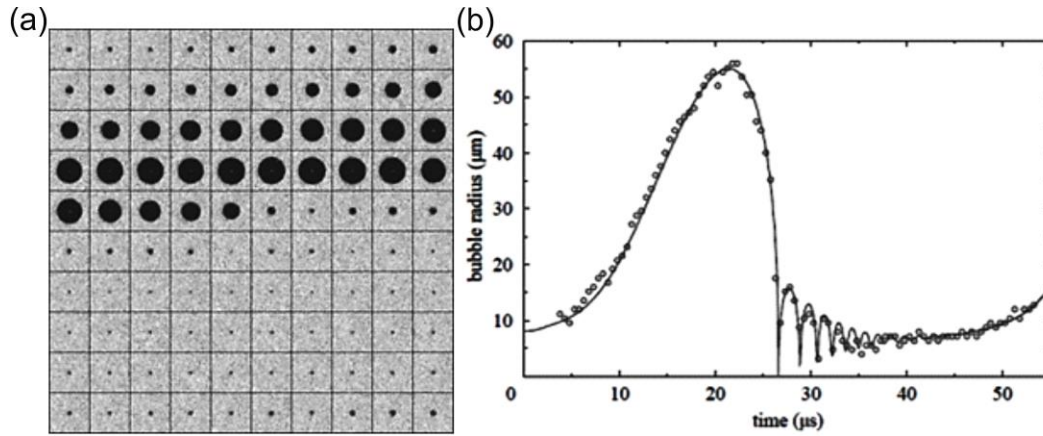


Fig. 2.15 Left: Photographs of a bubble driven at 21.4 kHz and 132 kPa. Right: Comparison of the numerically calculated curve (solid line) and experimental data (open circles). [67]

The bubble can also be generated by a focused laser radiation into a liquid with pulse duration [68]. This kind of bubble only lasts for a few of its own oscillation cycles, which allows for the study of transient bubbles in a controlled and flexible way. Figure 2.16 shows a photographic sequence of the free oscillation of a single laser bubble. It is observed that the spherical bubble reaches a maximum radius of about 2 mm, then the nonlinear oscillation is strongly damped after rebound from the first collapse and finally, the bubble is seen to be almost disappeared after several afterbounces.

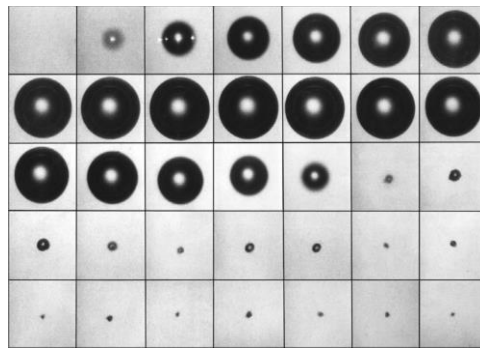


Fig. 2.16 Free oscillation of a laser bubble in water: the framing rate is 75,000; maximum radius is 2 mm. [68]

2.4 Translational dynamics of a bubble in oscillatory pressure fields

The bulk of early work on bubble dynamics was aimed at studying the radial motion of a bubble or bubble population in an actuated pressure field. However, the bubbles under external

actuators not only undergo volume oscillation but also move in space – translational motion. The translational dynamics of an oscillating bubble is coupled with the radial motion and cannot be worked out prior to solving the radial oscillating equation.

There are two ways of obtaining theoretical solution of the translational motion of an oscillating bubble. One method, first proposed by Crum and Eller [7], is averaging and decoupling the equations of radial and translational motions to calculate the long term behavior of the bubble. This approach is based on the averaged Bjerknes force – a kind of radiation force from the external actuators, buoyancy, gravity and viscous force etc. and justified in very weak actuation where both radial and translational movements are relatively small. Another way of studying translation of the bubbles is to solve the coupled equations of radial and translational motions of bubbles directly. The governing equations are coupled nonlinearly between the volume pulsation and translation, and therefore numerical calculation is demanded. This method is applicable to strong external actuators and become popular with the development of numerical analysis. Prior to discussing the translation of an oscillating bubble, several concepts are introduced such as Bjerknes force.

2.4.1 Bjerknes force and drag force

There are two physical phenomena which can be categorized as Bjerknes forces, primary Bjerknes force, which is exerted by the external pressure fields and secondary Bjerknes force, which is the mutual interaction between multiple oscillating bubbles.

Assuming that a bubble in an ideal liquid is spherical and small, and the spatial variation of the pressure gradient in the bubble is negligible. When the centroid of the bubble is located at some point at time t , the Bjerknes force subject to volume pulsation can be calculated in the following [69]

$$F = -\int_V \nabla p dV = -V(t) \nabla p(r, t) \quad (2.11)$$

where V denotes the volume of the bubble and p is the liquid pressure at the bubble wall. When the pressure gradient is caused by the external actuation pressures (e.g. travelling wave or standing wave), this force is the so-called primary Bjerknes force and when the pressure gradient is caused by other bubbles, this force is the so-called secondary Bjerknes force.

The average net force on the bubble during one cycle is

$$F_B = -\langle V(t)\nabla p(r,t) \rangle = -\frac{4\pi}{3} \langle R^3(t)\nabla p(r,t) \rangle \quad (2.12)$$

where $\langle \rangle$ denotes the time average and $R(t)$ is the radius of the bubble.

When considering a real fluid, we must add the viscous drag. The motion of the bubble in liquid can be discussed according to the Reynolds number. The Reynolds number is determined as the ratio of inertial forces to viscous forces and quantifies the relative importance of these two types of forces. In bubble dynamics, if the radial velocity of the bubble wall is introduced as a second characteristic velocity, there are two types of Reynolds number, $Re_U = \rho R |U| / \mu$, $Re_R = \rho R |\dot{R}| / \mu$ [70].

For $Re_U \gg 1$ or $Re_R \gg 1$, that is the bubble moves fast or is strongly forced, the viscous drag is similar to the case of a spherical droplet at high Re [70]

$$F_D = -12\pi\mu RU \quad (2.13)$$

When $Re_U \ll 1$ and $Re_R \ll 1$, that is the bubble is slowly translating with slow radial dynamics, the quasisteady Stokes drag force for an “ideal” bubble (zero shear stress at the interface) follows

$$F_D^{QS} = -4\pi\mu RU \quad (2.14)$$

2.4.2 Decoupled model of an oscillating bubble with weak actuations

A small bubble in an oscillatory pressure field (e.g. standing wave field) oscillates in volume and translates unsteadily and the two motions are coupled. However, it is of great convenience to decouple volume oscillation and translation as an approximation. The translational dynamics of a bubble in a decoupling way was first proposed by Crum and Eller [7]. The two equations are decoupled by averaging all the forces acting on the bubble during one cycle of vibration and the decoupling requires a weak external actuation. Consider an oscillating spherical bubble, the equation of momentum follows

$$F_{pB} + F_A + F_D = 0 \quad (2.15)$$

where F_{pB} is the generalized Bjerknes force, F_A is the force resulting from added mass and F_D is the drag, taking the form without history force. Substituting Eqs. (2.12) and (2.13) into Eq. (2.15), it is transformed to [71],

$$4\pi R^3 \nabla p / 3 - \frac{2\pi\rho}{3} \frac{d}{dt} (R^3 U) - 12\pi\mu R U = 0 \quad (2.16)$$

The pressure gradient and radial oscillation are assumed in the following forms

$$\nabla P(x, t) = \nabla P_a(x) \sin(\omega t) \quad (2.17a)$$

$$R(t) = R_0 [1 - \varepsilon \sin(\omega t)] \quad (2.17b)$$

The equation of motion is rewritten in the time-averaged form

$$\frac{2\pi\rho R_T^3}{3} \dot{U}_T = \frac{4\pi\nabla P_a}{3} \langle R^3 \sin(\omega t) \rangle - 12\pi\mu R_T U_T \quad (2.18)$$

where, $\langle \rangle$ denotes the time average of the quantity during one cycle.

Assuming all the transients expire, the average velocity follows that [71]

$$\bar{U} = -3\varepsilon k_2 / 2k_1 \quad (2.19)$$

where $k_1 = 18\mu / \rho R_0^2$, $k_2 = 2\nabla P_a / \rho$.

By means of this method, Crum and Eller [7] calculated the decoupled solution of averaged velocity of the bubble and found excellent agreement with experimental measurement.

2.4.3 Coupled model of an oscillating bubble with strong actuations

With the increasing capacity of calculation of computers, it is possible to solve the coupled equations of radial and translational motions of an oscillating bubble directly. Reddy and Szeri [72] numerically solved the coupled radial and translational dynamics of a single bubble in a travelling wave field. The radial and translational equations they used are described as

$$\dot{R}\ddot{R} + \frac{3}{2}\dot{R}^2 = \frac{1}{\rho} \left[P_L - P_\infty + \frac{R}{c_L} \frac{d}{dt} (P_L - P_\infty) \right] \quad (2.20a)$$

$$\frac{2\pi}{3} \rho \frac{d}{dt} [R^3 (U_a - \dot{X})] = \frac{4\pi}{3} R^3 \nabla P_\infty - 12\pi\mu R (U_a - \dot{X}) \quad (2.20b)$$

where, X is the displacement of the bubble, U_a is the absolute velocity of liquid. The liquid pressure at the bubble wall P_L is calculated by $P_L = P_g + \frac{R}{3c_g} \frac{dP_g}{dt} - \frac{4\mu_L \dot{R}}{R} - \frac{2S}{R}$ and the liquid pressure at infinity P_∞ , is calculated by $P_\infty = P_0 [1 - P_a \sin(2\pi f t)]$.

Two cases are calculated for a bubble of 2 μm in radius: one in a mild and super-resonant wave field and the other one in subresonant wave field (Fig. 2.17). The solution for coupled

collapse and translation dynamics is agreeable with past experiments and previous theories for decoupled translation dynamics.

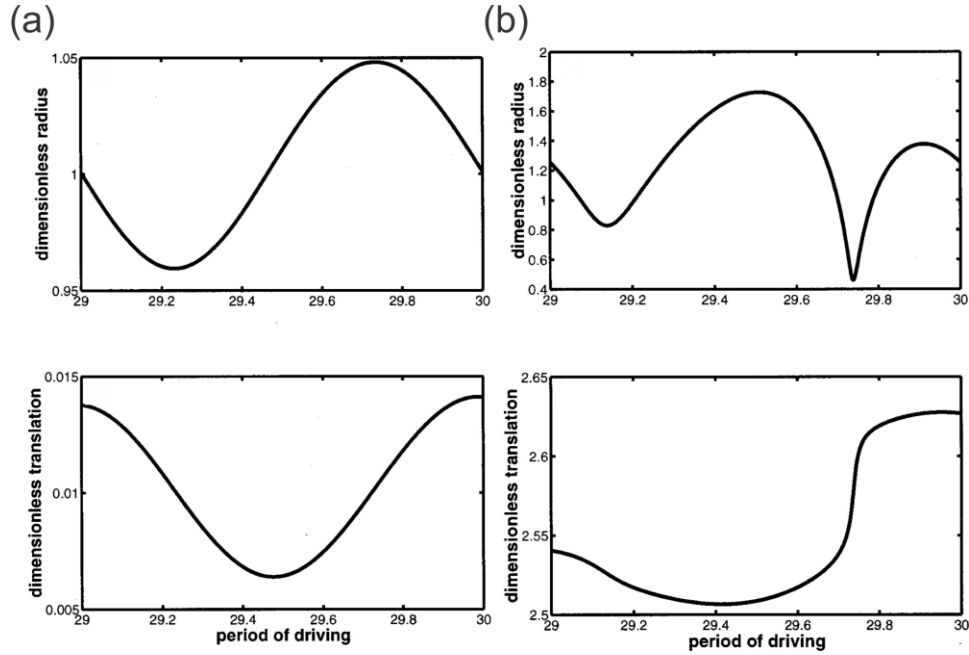


Fig. 2.17 Two cases of stable radial and translational response of a bubble ($R_0 = 2.0$ mm) after 29 periods of forcing when it undergoes: (a) mild, super-resonant actuation (b) subresonant excitation. [72]

Doinikov [8, 73] derived coupled equations of radial and translational motions of an oscillating bubble in an intense standing wave field using Lagrangian formalism. It is found that the radial equation needs a correction term considering the effect of translation. The new coupled equations read as [8]

$$R\ddot{R} + \frac{3}{2}\dot{R}^2 - \frac{P_L}{\rho} = \frac{\dot{x}}{4} \quad (2.21a)$$

$$\ddot{x} + \frac{3\dot{R}\dot{x}}{R} = \frac{3F_{ex}}{2\pi\rho R^3} \quad (2.21b)$$

where F_{ex} is the sum of primary Bjerknes force and viscous drag and P_L is the liquid pressure at the bubble wall and, $P_L = P_g - \frac{2S}{R} - \frac{4\nu_L\dot{R}}{R} - P_\infty$.

By solving the new equations, Doinikov proved that a bubble driven below resonance can reciprocate about the pressure node instead of moving towards pressure antinodes if pressure amplitude is high enough.

There is very little experimental investigation about translation of an oscillating bubble with external actuations since Crum's experiments [7]. Mettin [74] displayed the “jerky” motion of two bubbles during its collapse in Fig. 2.18. The centroid positions of two bubbles that move upwards are marked by white lines. It can be clearly observed that the bubble position frequently jumps upwards during collapse, and stops during expansion. The relatively net velocity of the bubbles is 1 to 1.5 m/s.

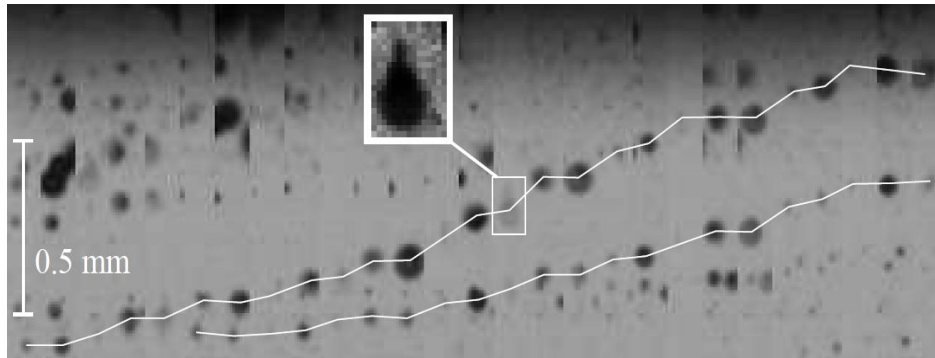


Fig. 2.18 Jerky motion of two bubbles with strong actuations: vertical stripes from successive frames are displayed next to each other, time proceeding from left to right. The acoustic frequency is 20 kHz, and the inter-frame time is 0.4 periods. [74]

2.5 Bubble boundary interaction

Due to the practical importance of bubble-wall interaction in ultrasonic cleaning, sonochemistry and erosion of bubble collapse as well as in medical applications, some progress has been achieved about the dynamics of a bubble nearby plane boundaries and confined configurations [75].

Far from the boundary wall, a bubble in an oscillatory pressure field can be regarded as spherical and the potential problem can be solved by the method of images that replaces the rigid boundary by an image bubble equal to the real one and located symmetrically to it with respect to the boundary.

Cole simulated the global motion of a bubble in the neighborhood of a plane solid wall or a free interface by introducing a series of images [76]. Using Cole's strategy, Sato et al. [77] studied the behavior of a gas bubble near a rigid boundary in an oscillatory pressure field and they found that the period and amplitude of the bubble oscillation are related not only to the

actuation pressure but also to the bubble location from a rigid wall. Near a solid surface, the asymmetry of the flow that the boundary itself introduces gives rise to highly non-spherical bubble shapes and even leads to the formation of a high-velocity jet directed toward the wall at its collapsing phase, while the overall characteristics of the sinklike flow of the image attracts the bubble toward the wall. Kroninger et al. [78] investigated the bubble collapsing aspherically near a rigid wall and experimentally observed the development of a jet and a vortex ring as shown in Fig. 2.19. Besides, their simulation results with the boundary integral method are in good accordance with the experimental observation.

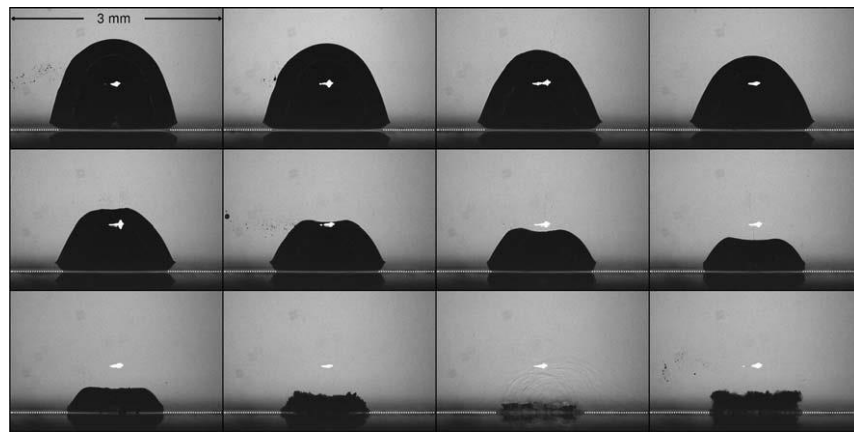


Fig. 2.19 Photograph of a laser bubble collapsing in the vicinity of a glass wall located at the bottom (time between frames: 5 μ s). [78]

Xi et al. [79] investigated the dynamics of collective bubbles near a solid surface, especially the bubble translation, in a weak acoustic standing wave field as shown in Fig. 2.20. It was found that the bubble translation near a surface in a multi-bubble environment was mainly controlled by the primary Bjerknes force imposed by the acoustic field, and secondary Bjerknes force introduced by a surface and neighboring bubble. The primary Bjerknes force dominated the bubble translation when the bubble was far away from the surface and was outweighed by the secondary Bjerknes force from the boundary when the bubble was approaching the surface. Xi et al. also found that the presence of a wall can change a bubble's oscillation mode and in particular, the wall shifts the instability pressure thresholds to smaller driving frequencies for fixed bubble equilibrium radii, or to smaller equilibrium radii for fixed excitation frequency [80].

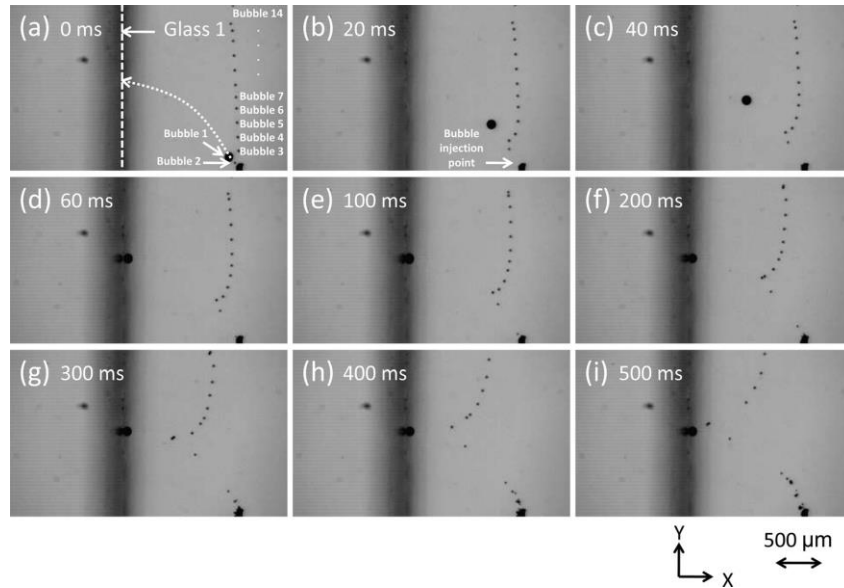


Fig. 2.20 Selected frames showing the translations of several bubbles at (a) 0 ms, (b) 20 ms, (c) 40 ms, (d) 60 ms, (e) 100 ms, (f) 200 ms, (g) 300 ms, (h) 400 ms, and (i) 500 ms. The pressure amplitude was 11.5 kPa. [79]

Investigations have also been conducted with the dynamics of bubbles in the proximity of an elastic boundary or composite material, a free surface, a convex or concave wall, in gaps or tubes and so on [81-83].

2.6 Bubble dynamics in microfluidics

While bubble dynamics has been observed and studied extensively in bulk fluid flows, the bubble dynamics, especially acoustic cavitation, has not been widely investigated in microfluidics so far. The challenges of energy concentration, viscous surface forces and low number of cavitation nuclei make it difficult to generate bubbles directly in microfluidic channels via the conventional method [10]. In current studies of bubble dynamics, the generation of gas bubbles can be formed by the external introduction of gas phase through a flow-focusing system

By importing external gas as the secondary phase, Garstecki et al. [84] firstly reported a method for generating monodisperse bubbles in a microfluidic flow-focusing device as illustrated in Fig. 2.21. The bubbles self-assemble into highly-ordered flowing lattices depending on flow parameters. Shirota et al. [85] produced submillimeter bubbles from an orifice by means of a complex system with a loudspeaker (Fig. 2.22) similar to flow-focusing channels. The

detachment of a bubble is controlled by pulsed actuation pressure and the intensity of actuation pressure is controllable to generate much smaller bubbles compared to ordinary flow-focusing systems.

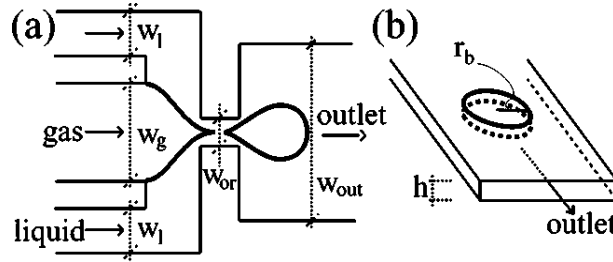


Fig. 2.21 (a) The microfluidic flow-focusing device (top view). (b) Illustration of a bubble in the outlet channel. [84]

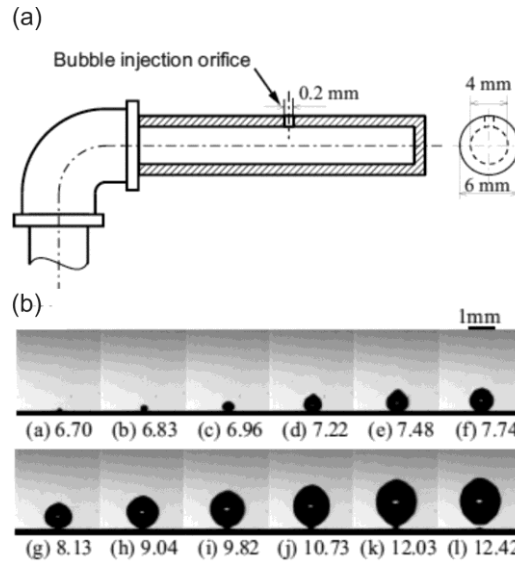


Fig. 2.22 (a) Schematic of apparatus for bubble generation via a flow-focusing section with external actuations; (b) A series of selected frames of bubble formation captured by highspeed photography at 7692 frames/s. [85]

At high frequency actuations, the wavelength of acoustic fields is short and comparable to the microfluidic channel and bubble size. As such, acoustic field and pressure gradients will be established around the bubbles, which will induce significant primary Bjerknes force on the bubbles. Therefore, the current studies of bubble dynamics in microfluidics are concentrated on high frequencies, ranging from 20 kHz to several MHz, to obtain large primary Bjerknes force as the driving force of bubble motion.

Rabaud et al [86] demonstrated the use of primary Bjerknes force or the acoustic radiation force to induce the motion of bubbles confined between walls of microchannels. They developed two applications in microfluidics based on the interplay between the primary Bjerknes force and drag force: asymmetric bubble breakup to produce very well controlled bidisperse populations and intelligent switching at a bifurcation. Segers and Versluis [87] presented a simple lab-on-a-chip method to sort the population of coated microbubbles using the primary Bjerknes force in a travelling ultrasound wave field as shown in Fig. 2.23. They demonstrated successful sorting of a commercial ultrasound contrast agent (UCA) and improved the sensitivity of the contrast sound.

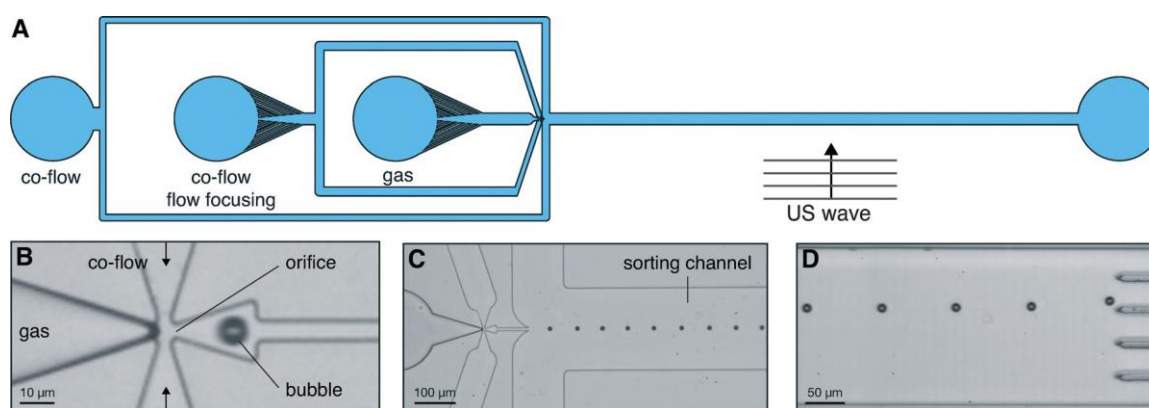


Fig. 2.23 (A) Schematic design of the sorter of microbubbles using the primary Bjerknes force. (B) Photograph of the flow focusing section. (C) Microbubbles are formed in a narrow orifice. (D) A travelling wave changes the trajectory of a series of bubbles. [87]

Another method of bubble generation is radiation of a pulsed laser into the liquid. Zwaan et al. [88] reported generation of bubbles in confined microfluidic system by focusing a pulsed laser into the light-absorbing liquid. The pancake-shaped bubbles expand and collapse radially, agreeable with a two-dimensional Rayleigh-Plesset model. They also investigated the cavitation bubble dynamics in microfluidic gaps with variable height and found that the bubble lifetime increases with decreasing gap height whereas the maximum bubble radius remains constant [89]. Patrascioiu et al. [90] studied the correlation between the laser-induced bubble and liquid ejection by analyzing the time-resolved behavior of the bubble and liquid jetting and found that the pulsating behavior of the bubble leads to successive jetting events with different jet morphologies arising from the particular geometries that the bubble acquires during its evolution. Their results are in good agreement with the numerical simulation of cavitation bubbles near a free-surface of a liquid.

The shortcomings of bubble generation by flow-focusing system or by laser radiation are prominent: formation of bubbles in flow-focusing systems requires introduction of external gas and elaborate manipulation; laser-induced bubbles are transient and laser devices are indispensable for the method of laser radiation. Therefore, the existing methods of bubble generation by external gas or laser radiation are inconvenient in real applications and new methods for bubble generation in microfluidic systems are attractive research topics in this field.

In addition, at low-frequency actuations, the acoustic wavelength will be long comparing to the bubble size and microfluidic channel. For example, the pressure wavelength is 1.5 meter for the case of 1 kHz actuation in water (taking the sound speed in water as 1500m/s). This will be much larger than the dimension of the bubble size and microfluidic channels, which are normally in 10^{-2} m – 10^{-4} m. As a result, the actuated pressure is almost uniformly distributed in the microfluidic channels and the pressure gradient is very small around the bubbles, leading to a weak primary Bjerknes force exerting on the bubbles. Therefore, other mechanisms, such as the wall effect, tend to be the dominant factor to propel the bubble forward under the low-frequency actuation in a microfluidic chamber. In a microfluidic system, the bubbles are enclosed by multiple walls, and in this case the wall effect will be much more complicated than the case of a single wall. Therefore, the dynamics of a bubble in the neighborhood of multiple walls needs to be further investigated.

Chapter 3 Vortex Generation in a Microfluidic Chamber: Characterization

In this chapter, a novel resonator-shaped microfluidic chamber is designed for vortex generation. A PZT (Lead Zirconate Titanate) disk is assembled to the microfluidic chamber from one side to actuate the fluids. The details of the experiment method, including the configuration and fabrication, experimental setup, and measurements of the performance are clearly presented. The vortices generated in the chamber are visualized by tracing fluorescent dye and the vortex intensity is quantitatively analyzed by processing the recorded images in MATLAB. The influence of the actuation conditions, such as the actuation frequency, voltage and flowrate, on the performance of vortex generation in the microfluidic chamber is investigated. The performance of the resonator-shaped chamber is compared with another type of circular chamber to study the effect of the resonator-shaped nozzle part on the vortex generation.

3.1 Experimental methods

3.1.1 Design and fabrication of the microfluidic chamber for vortex generation

The microfluidic chamber for vortex generation is made by two PMMA (polymethylmethacrylate) plates sandwiched by a dry adhesive layer with 300 μm in thickness (Arclad 8102 transfer adhesive, Adhesives Research, Inc.). The configurations and dimensions of the microfluidic chamber are shown in Fig. 3.1. It mainly consists of two parts, a 16 mm diameter semi-circular chamber and a nozzle with an acoustic resonator profile. The overall geometric profile of the chamber can be expressed by

$$y = \begin{cases} \sqrt{8^2 - x^2} & , \quad -8 \leq x \leq 4; \\ 0.5e^{0.1011(30-x)} & , \quad 4 \leq x \leq 30. \end{cases} \quad (3.1)$$

Two inlets are connected at a 60-degree angle to the chamber by a straight channel of 10 mm in length and 1 mm in width, and another straight channel is connected to the other end of the chamber to form the outlet. A PZT (Lead Zirconate Titanate) disk is attached to the bottom of the

chamber to provide actuations. The PZT disk is formed by a piezoelectric ceramic layer of 15 mm diameter glued onto a brass sheet of 22 mm diameter. The brass sheet was painted to avoid direct contact with the working fluids in the chamber. The geometry of the entire configuration is precisely manufactured by a laser cutting machine (Universal M-300 Laser Platform, Universal Laser Systems Inc., Arizona, USA). For comparison, another type of microfluidic chamber without the resonator-shaped nozzle is designed and the configurations and dimensions are illustrated in Fig. 3.2.

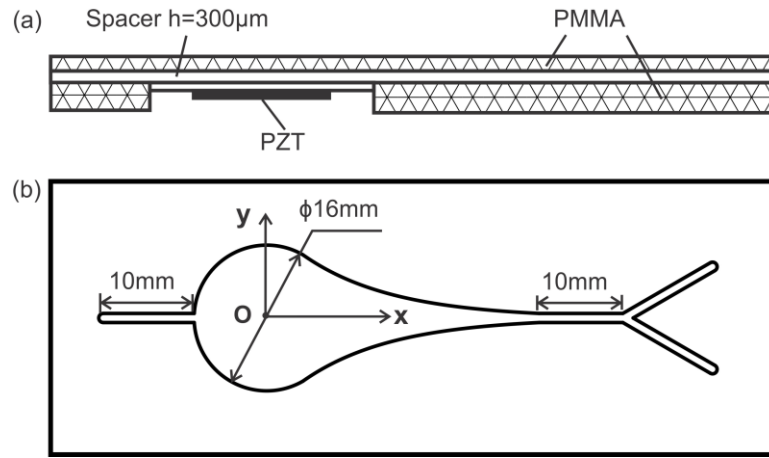


Fig. 3.1 Schematic illustration of the microfluidic chamber with resonator-shaped nozzle. (a) Side view of the configuration; (b) Top view of the configuration with channel design and geometric dimensions.

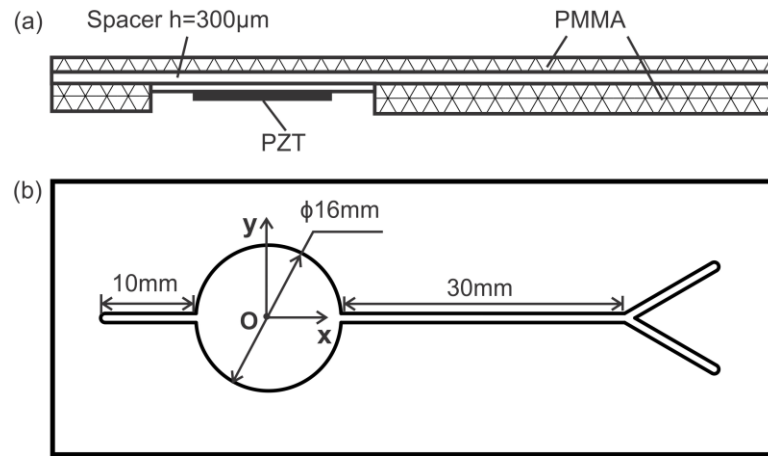


Fig. 3.2 Schematic illustration of the microfluidic chamber without resonator-shaped nozzle. (a) Side view of the configuration; (b) Top view of the configuration with channel design and geometric dimensions.

The microfluidic chamber is fabricated by lamination technology. Two PMMA plates are assembled together by a dry adhesive layer in the middle. The height of the channel is controlled

by the thickness of the adhesive layer. The PZT disk is fitted into the access hole of the top PMMA plate. The inlets and outlet are assembled to the plate by epoxy glue (Araldite, Huntsman Advanced Materials, USA). The concept of fabrication and the assembled device are shown in Fig. 3.3.

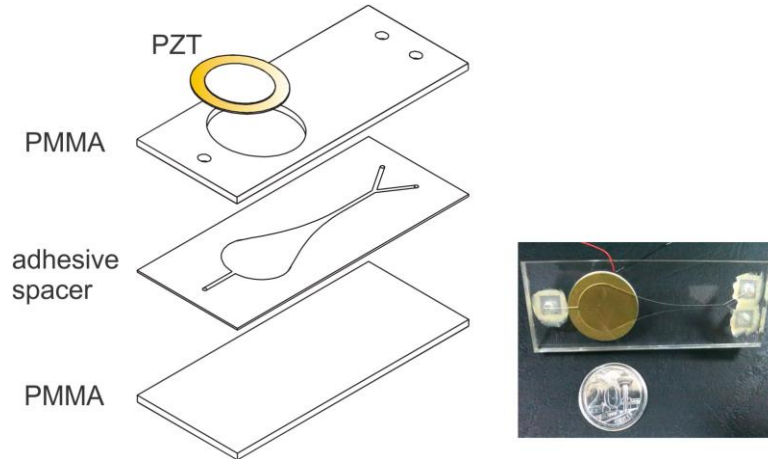


Fig. 3.3 The concept of fabrication and the assembled device.

3.1.2 Experimental setup and characterization

The schematic of the experimental setup is illustrated in Fig. 3.4. In the experiment, a degassed DI water solution was supplied to the microfluidic chamber from inlet A, and the same solution with fluorescent dye was supplied to inlet B. The flowrate was adjusted by two syringe pumps (KD Scientific Inc., USA). By using the fluorescent dye as flow tracers, the vortices can be observed inside the microfluidic chamber after the PZT is switched on under varied voltages and frequencies. The piezoelectric disk was driven by sinusoidal signals generated by a signal generator (33120A, Hewlett Packard) and then amplified 50 times by a voltage amplifier (790, PCB Piezotronics). A high speed CCD camera (Phantom V711, Vision Research, USA) is mounted on top of the chamber to record the flow field.

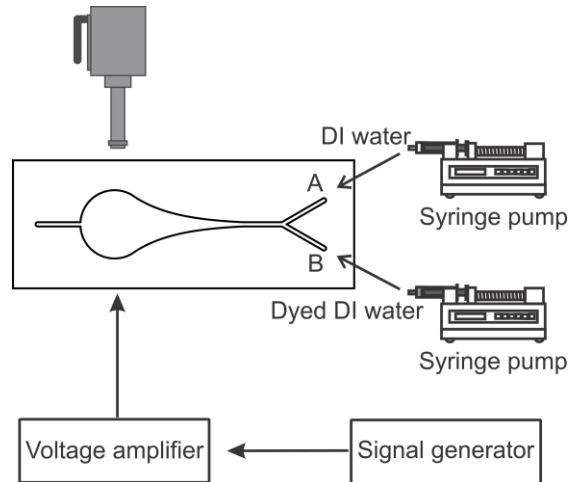


Fig. 3.4 Schematic illustration of the experimental setup for vortex visualization.

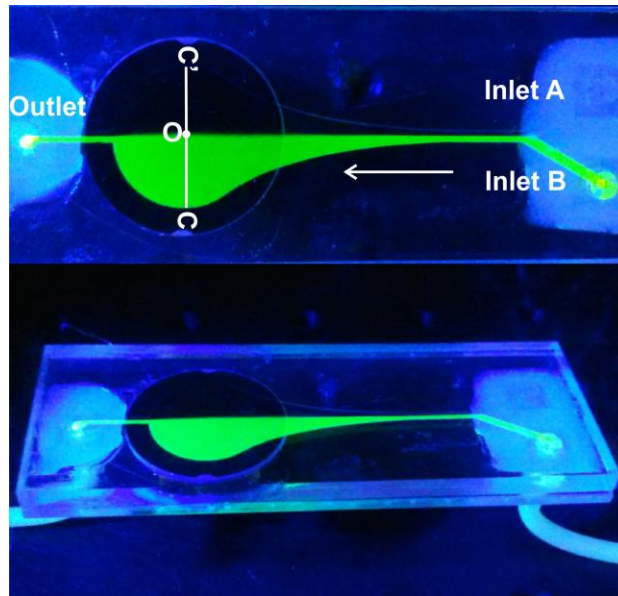


Fig. 3.5 The microfluidic chamber filled with working fluids and the cross line C'-O-C for vortex characterization.

When a vortex forms, the working fluids are stirred and swirled, leading to the mixing of the fluorescent dye in the chamber. Therefore, the vortex intensity is proportional to the uniformity of the fluorescent dye concentration in the chamber, which is an indicator associated with the vortical flow and vortex strength. To quantitatively characterize the intensity of the vortex, a MATLAB code was used to process the captured images assuming that the intensity of grayscale is related to the fluorescent dye concentration in the recorded images.

A cross line C'-O-C (Fig. 3.5) through the center of the chamber was chosen to be analyzed. The vortex intensity is calculated using the following expression:

$$\text{Vortex Intensity}(\%) = 1 - \sqrt{\frac{1}{N-1} \sum_{i=1}^N \left(\frac{\bar{I}_i - \bar{I}_{ave}}{\bar{I}_{ave}} \right)^2} \quad (3.2)$$

where, N represents the total number of points examined along the cross-line C-O-C', \bar{I}_i is the normalized intensity at each point, \bar{I}_{ave} is the mean of normalized intensity at all points, which is calculated by $\bar{I}_{ave} = \frac{1}{N} \left(\sum_{i=1}^N \bar{I}_i \right)$ and the square root denotes the standard deviation of the fluorescent dye distribution. Ideally, this expression will give 0% before vortex is generated and 100% if the fluids are perfectly mixed resulting from the vortex.

The procedures of the experiment are stated in detail as follows:

(1) Fix the device onto a metal holder and then connect the function generator, amplifier and the PZT disk of the microfluidic chamber. Mount a high-speed camera above the PMMA plate enclosing the chamber and install the LED (light emitting diode) as the illumination system.

(2) Fill one syringe with the degassed DI water and the other one with the DI water of fluorescent dye. Connect the syringes with the inlets of the chamber through plastic tubes.

(3) Install two syringes to a pump and switch on the pump to supply the working fluids into the microfluidic chamber through two inlets.

(4) When the flow in the chamber is stable, turn on the PZT disk and meanwhile trigger the camera to record the flow patterns inside the chamber until the flow is fully developed.

(5) Adjust the actuation conditions including the frequency, voltage and flowrate to investigate the influences on the performance of vortex generation. Make sure that the channel is free from bubbles in the experiment.

3.2 Results and discussion

3.2.1 Flow pattern development in the microfluidic chamber

By tracing the patterns of the fluorescent dyes in the flow, the vortices generated in the chamber can be visualized and characterized. Figure 3.6 presents the evolvement of the

generated vortex with time sequences after the PZT disk is actuated. The experimental conditions are as follows: a flowrate of 2 mL/h at each inlet, an actuation voltage of 100 V and a frequency of 2.0 kHz. Without actuations (Fig. 3.6(a)), the interface between the upper fluid (without fluorescent dye from inlet A) and lower fluid (with fluorescent dye from inlet B) is very clear, indicating that the flow is laminar, without vortices. However, as shown in Fig. 3.6(b), 5 seconds after the actuation is turned on, the fluorescent-dyed fluid has been swirled up to the upper half of the chamber and a vortex can be clearly observed. The fluorescent fluid is continuously swirled (see Fig. 3.6(c-e)) and at 25 seconds, the fluids with fluorescent dye are found to occupy the whole chamber. Finally, at 45 seconds, the interface of the fluorescent dye in the fluids disappears with the action of the vortex and the flow pattern is fully developed.

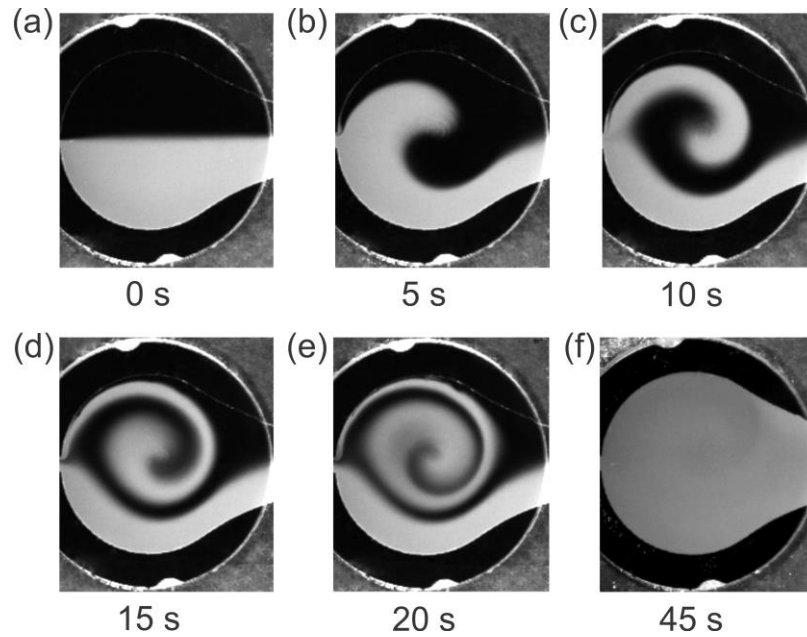


Fig. 3.6 Recorded images in time sequence to show the vortex generated in the microfluidic chamber with actuations. The actuation voltage and frequency were 100 V and 2.0 kHz, and the flowrate was 2 mL/h at each inlet.

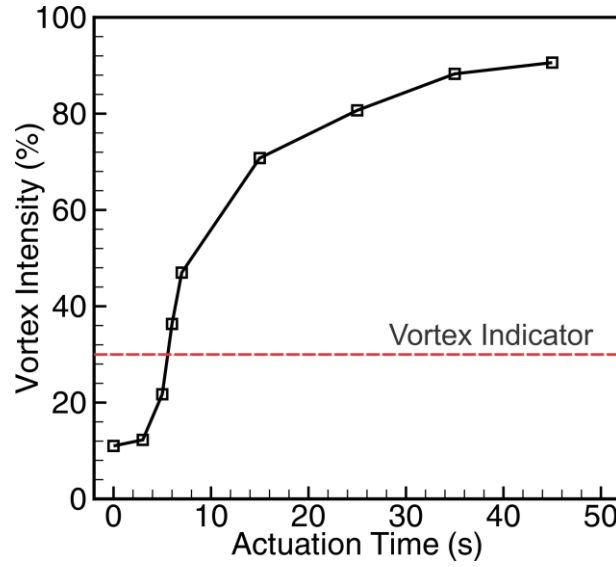


Fig. 3.7 The dependence of the vortex intensity with time after being formed in the chamber. The actuation voltage and frequency were 100 V and 2.0 kHz, and the flowrate was 2 mL/h at each inlet.

In terms of Eq. (3.2), the vortex generation is further characterized by the vortex intensity with time sequence after generation as shown in Fig. 3.7. It shows that the vortex intensity increases with time under the action of the vortex and reaches up to 90% at 45 seconds. We take 30% as a criterion to determine whether the vortex is formed or not inside the chamber although such criterion is a bit arbitrary [91]. Since the vortex is observed by tracing the fluorescent dye and the time scale is characterized by the fluorescent diffusion in such low Reynolds number flow, it therefore takes a long time to observe the vortex formation. The actual vortex development corresponding to the actuation should be much faster and characterized by the actuation frequency. Scalling analysis suggests that the characteristic time for a vortex development is of order $\tau_{vor} = O(1/f)$. Using $f = 2.0$ kHz in frequency, we can obtain the time scale of the vortex development is of the order $\tau_{vor} = O(10^{-3})$ second. On the other hand, the characteristic time of fluorescent dye can be estimated from $\tau_{dye} = O(L_c^2/D)$. Taking the characteristic dimension $L_c = 300 \mu\text{m}$ in channel height and diffusion coefficient $D = 10^{-10} \text{ m}^2/\text{s}$ in dye diffusivity [92], we can find the fluorescent dye relaxation time of the order $\tau_{dye} = O(10)$ second, which is in good agreement with our experimental observation as shown in Fig. 3.6.

3.2.2 Effects of actuation frequency on the generated vortices

The vortices generated in the microfluidic chamber are further investigated under various frequencies. It is found that the pattern of the vortical flow varies at different frequencies. Figure 3.8 and 3.9 show the flow pattern development with time under the actuation of 1.5 kHz and 2.5 kHz for actuation frequency, respectively. The applied voltage was fixed at 100 V and the flowrates were kept 2 mL/h at each inlet. The working fluids are DI water. It is observed that at 1.5 kHz, the vortex is irregular and the flow is rotating around an axis located at the upper-right half of the chamber, compared to the vortex at 2.0 kHz. As shown in Fig. 3.9, at 2.5 kHz, in addition to a large vortex in the middle of the chamber, a smaller one is also observed to occur on the upper-left side of the chamber, which is different from a single vortex at 2.0 kHz.

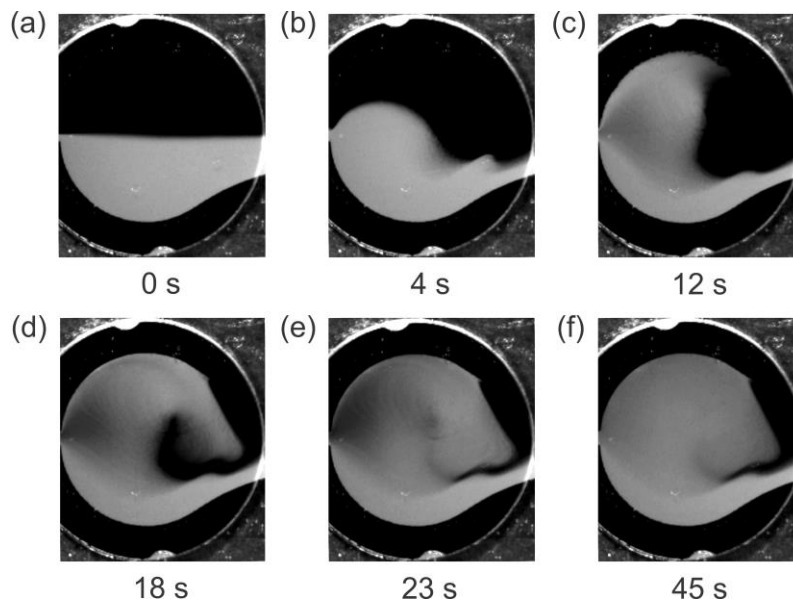


Fig. 3.8 Recorded images in time sequence to show the development of the flow pattern under the actuation of 1.5 kHz. The actuation voltage was 100 V and the flowrate was 2 mL/h at each inlet.

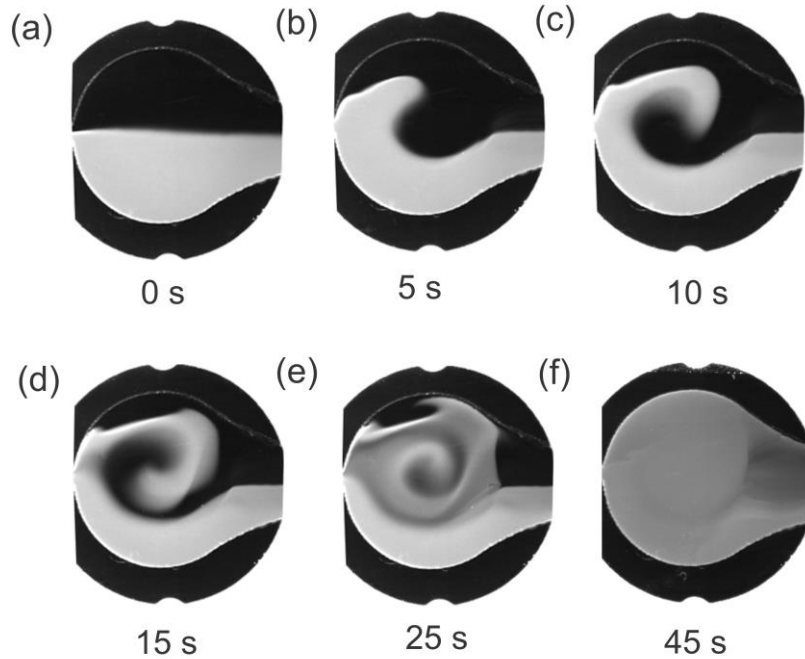


Fig. 3.9 Recorded images in time sequence to show the development of the flow pattern under the actuation of 2.5 kHz. The actuation voltage was 100 V and the flowrate was 2 mL/h at each inlet.

The vortex intensity along the line C'-O-C under various actuation frequencies is calculated by Eq. (3.2) at different times. The vortex intensity versus time for different actuation frequencies is shown in Fig. 3.10. The results show that, the time it takes to achieve the vortex intensity above 30% differs for different actuation frequencies: at 1.5 kHz, 2.0 kHz or 2.5 kHz, the vortex generation is quite easy, indicated by the short times (<10 s) for the vortex intensity to reach above 30% and at either 3.5 kHz or 1.5 kHz, the vortices are found to become too weak to achieve the vortex intensity above 30%. The vortex intensity at 50 seconds when the flows at various frequencies are fully developed is depicted in Fig. 3.11. It is clear that there exists an effective frequency window, within which the strong vortex can be generated while out of this frequency window, the vortex is very weak or even unable to occur in the chamber. In the range from 1.5 kHz to 3.0 kHz, strong vortex can be generated easily with the vortex intensity as high as 70%. At either higher frequencies, e.g. 3.5 kHz or lower frequency, e.g. 1.0 kHz, the vortex is found to become weaker, even below 10%. Such actuation frequency window is found to be dependent on the actuation voltage and flowrate.

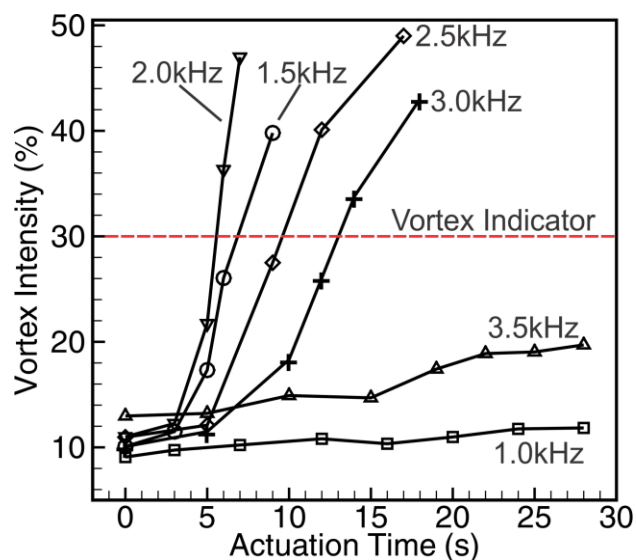


Fig. 3.10 Development of the vortex intensity versus time after the actuation is turned on under various actuation frequencies. The applied voltage and flowrate were fixed at 100 V and 2 mL/h, respectively.

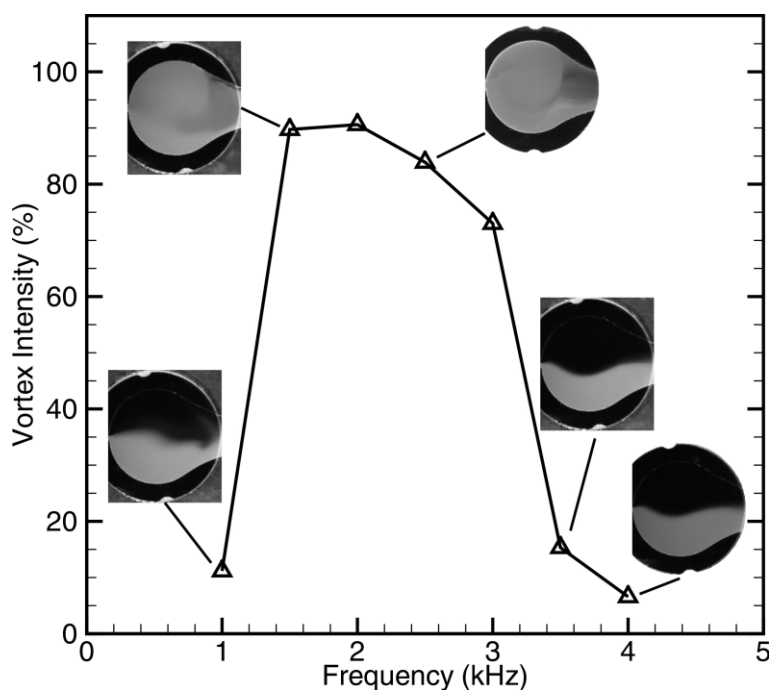


Fig. 3.11 Effect of actuation frequency on vortex formation and intensity after the flow patterns are fully developed. The inset images were recorded at 50 seconds. The PZT disk was actuated at the voltage of 100 V and the flowrate was 2 mL/h at each inlet.

3.2.3 Effects of the applied voltage on the generated vortices

The influence of the applied voltages was investigated by varying the actuation voltage from 40 V to 120 V and the actuation frequency was fixed at 2.0 kHz and the flowrates at 2 mL/h at each inlet. The working fluids are DI water. The flow patterns in Fig. 3.12 were recorded at 50 seconds when the flows are fully developed for all voltages. It is seen that, at 40 V, there were almost no fluorescent dyes in the upper half of the chamber. From 60 V to 80 V (Fig. 3.12(b-c)), more and more fluorescent dyes emerge on the upper half of the chamber with increasing voltages. The higher voltage is applied, the more fluorescent dye is swirled to the upper-half part of the chamber, indicating a stronger vortex is formed by the actuation. However, at very high voltages, gas bubbles are observed in the chamber in addition to the strong vortex flow. As shown in Fig. 3.12(d) for the actuation at 120 V, bubbles are found at some position close to the upstream straight channel (indicated by a dashed rectangle). The bubble generation was reported previously, in which flow mixing enhancement was attributed to the bubble oscillations without mentioning the vortices [93]. The present study clearly reveals that the mixing enhancement can occur without bubbles at relatively low voltages, only because of the vortices generated in the chamber, and at very high voltages, the combined effects of the vortex and bubbles contribute to the mixing enhancement.

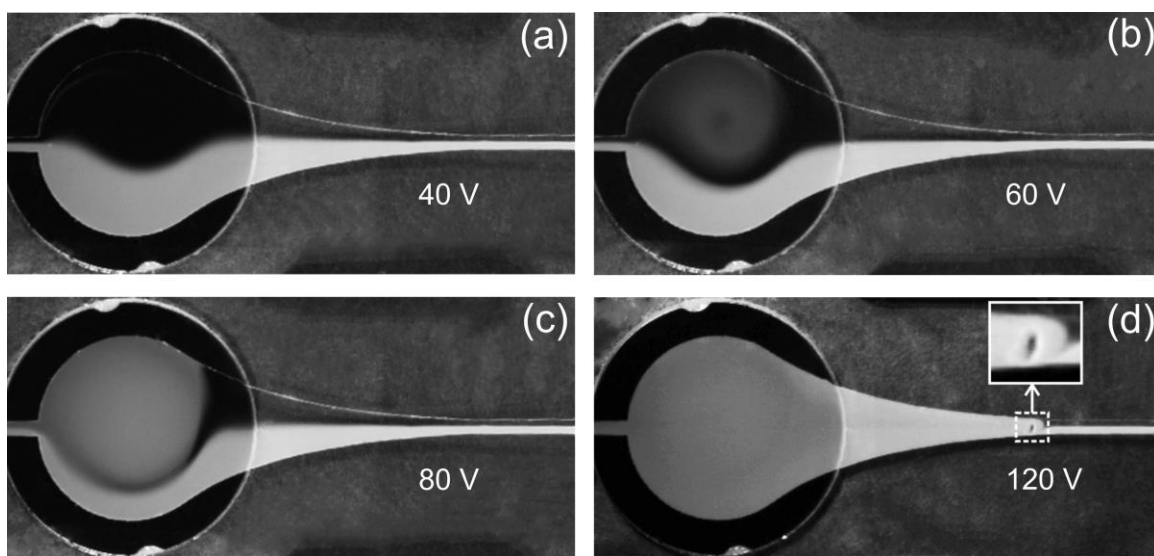


Fig. 3.12 The images of the flow patterns under various applied voltages from 40 V to 120 V for the DI water. The images were recorded at 50 seconds after actuation is switched on. The driving frequency was 2.0 kHz and the flowrate was 2 mL/h at each inlet.

The intensity of the generated vortex under various applied voltages is calculated in terms of Eq. (3.2). Figure 3.13 shows the vortex intensity versus time for different applied voltages, with the frequency and flowrate being fixed at 2.0 kHz and 2 mL/h at each inlet. It is seen that, at the low actuation voltage 40 V, the vortex cannot be properly formed and the vortex intensity remains below 30%. As the voltage is increased to 60 V, the vortex intensity is above 30% after 12 seconds. The higher voltage is applied, the shorter time is taken to bring the vortex intensity above 30%, indicating a stronger vortex formed by the actuation. We demonstrate the vortex intensity under various applied voltages at 50 s when the flows are fully developed for all cases in Fig. 3.14. Clearly the vortex intensity is increased almost proportional to the applied voltages. The vortex intensity is very poor (approx. 10%) at 40 V and increases to 90% at 100 V before the bubbles occurs and when the voltage of 120 V is applied, the vortex intensity reaches 96.4%. The results show that the mixing enhancement can be mainly attributed to the strong vortices generated inside the chamber rather than the bubbles, because the bubbles are generated only at higher actuation voltages.

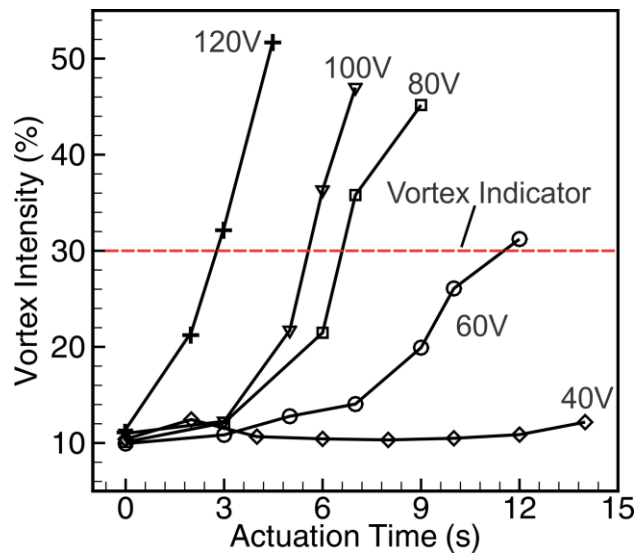


Fig. 3.13 Development of the vortex intensity versus time after the actuation is turned on under various applied voltages. The actuation frequency and flowrate at each inlet were fixed at 2.0 kHz and 2 mL/h, respectively.

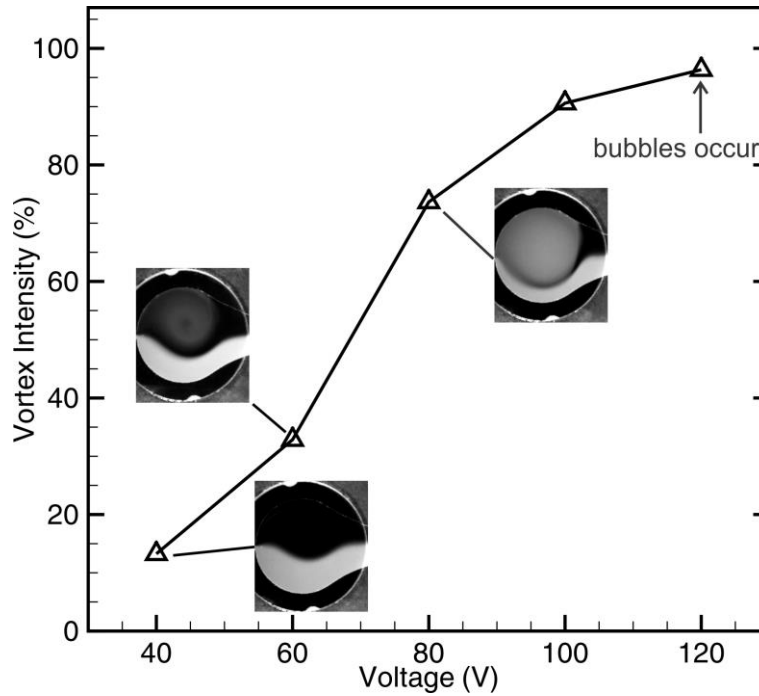


Fig. 3.14 Effect of the applied voltage on vortex formation and intensity after the flow patterns are fully developed. The inset images were recorded at 50 seconds. The PZT disk was actuated at the frequency of 2.0 kHz and the flow rate was 2 mL/h at each inlet.

3.2.4 Effects of flowrates on the generated vortices

To study the effects of flowrates on the performance of the generated vortices, the driving frequency was fixed at 2.0 kHz and the voltage was 100 V while the flowrate at each inlet was increased from 2 mL/h to 20 mL/h. The working fluids were DI water. The vortex intensity versus time for different flowrates was plotted in Fig. 3.15. It can be clearly seen that at low flowrates the strong vortices are relatively easy to be generated, while at high flowrates the vortices are relatively difficult, even unable to be generated if the flowrate at each inlet is equal to or higher than 10 mL/h. The time that it takes for the vortex intensity to reach 30% is increased with the flowrates of the fluids. The vortex intensity under various flowrates is demonstrated in Fig. 3.16 at 50 s when the flows are fully developed for all cases. It shows that the vortex intensity decreases with the increasing flowrate. At the flowrate of 2 mL/h, the vortex intensity is up to 90% and when the flowrate at each inlet is increased to 20 mL/h, the vortex intensity is dropped to approximately 10%. These vortex generation results indicate strong interactions of the hydrodynamic driving of the incoming flows and PZT actuations inside the chamber. The hydrodynamic force from the syringe pump is to maintain the

flowrate and laminar flows in the channel, while the actuation is to impose an external force on the flow for the vortex generation. It is believed that relatively higher hydrodynamic force, corresponding to high flowrates, can counterbalance the external force produced by the actuations so that the vortex becomes weak, is suppressed, or even completely vanishes.

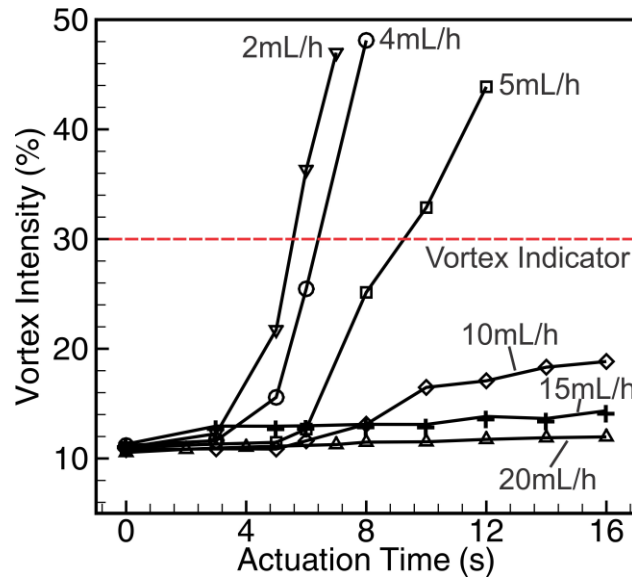


Fig. 3.15 Development of the vortex intensity versus time after the actuation is turned on under various flowrates. The actuation frequency and voltage were fixed at 2.0 kHz and 100 V, respectively.

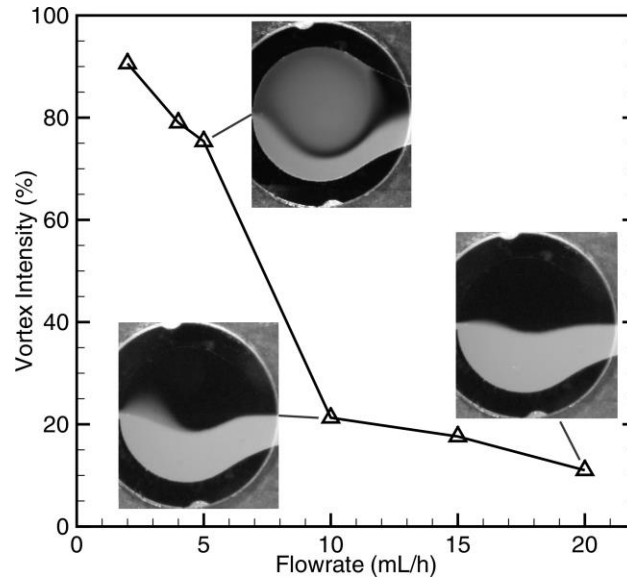


Fig. 3.16 Effect of flowrates on vortex formation and intensity in DI water. The inset images were recorded at 50 seconds after actuation is switched on. The PZT disk was actuated with frequency 2.0 kHz and the applied voltage was 100 V.

3.2.5 The vortex generation in a circular chamber

Investigation of the vortex generation in a circular microfluidic chamber is also conducted for comparison to study the role of the nozzle part in vortex generation. Figure 3.17 shows the flow pattern development in a circular chamber at different times during actuation. By tracing the patterns of the fluorescent dyes in the flow, the vortices generated in the chamber can be visualized and characterized. The experimental conditions as follows: a flowrate of 2 mL/h at each inlet, an actuation voltage of 140 V and a frequency of 2.0 kHz. Similar process of the flow pattern development is observed in the chamber except that the vortex is smaller than that generated in the resonator-shaped chamber. The vortex intensity in a circular chamber was plotted versus time in Fig. 3.18. It can be seen that about 10 seconds after the actuation, the vortex intensity reaches 30% and finally, at 50 seconds, the vortex intensity is only about 50% even when the flow is fully developed. It has been demonstrated that the profile of the nozzle can be used as an acoustic resonator to achieve high amplitude pressure fluctuations and therefore, the resonator-shaped chamber can achieve stronger vortices than the circular chamber.

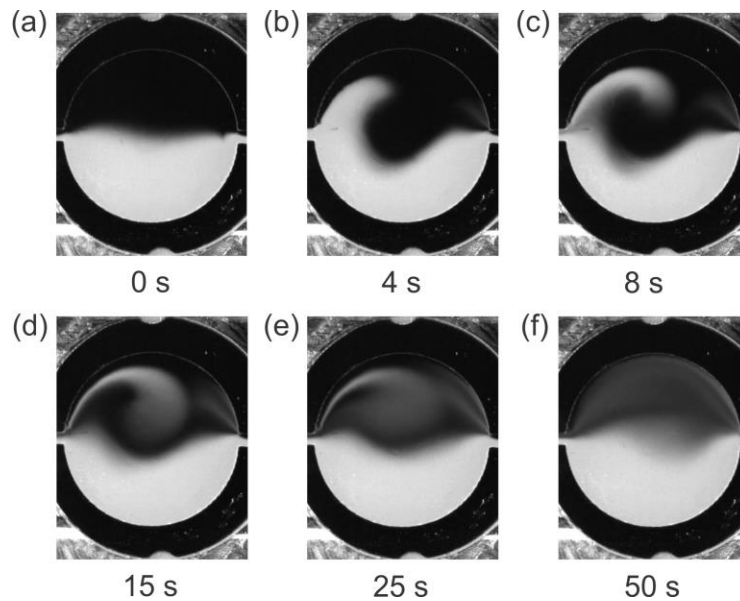


Fig. 3.17 Visualization of the generated vortex in a circular chamber at the voltage of 140 V. The actuation frequency was 2.0 kHz and the flowrate was 2 mL/h at each inlet.

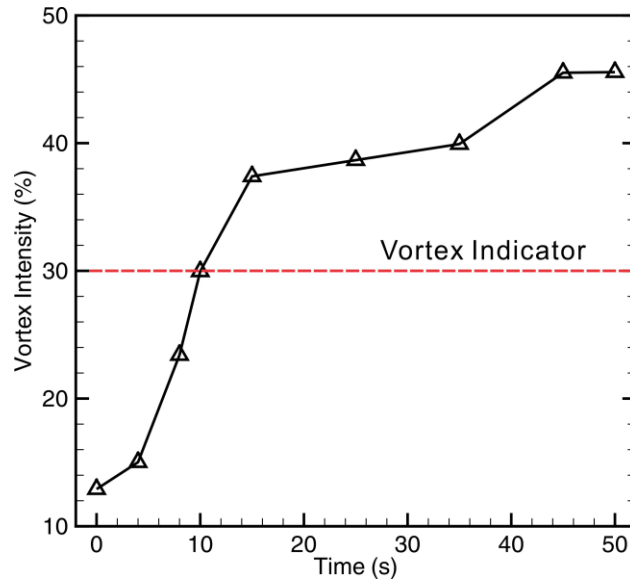


Fig. 3.18 Development of the vortex intensity versus time after the actuation is turned on in a circular chamber. The actuation frequency and voltage were fixed at 2.0 kHz and 140 V, and the flowrate at each inlet is 2 mL/h.

3.2.6 The counter-clockwise vortices

In the previous experiments, the generated vortices are rotating in the clockwise direction. In fact, we have also found that the vortex in the counter-clockwise direction can be generated in the chamber. The experimental conditions include: a flowrate of 2 mL/h at each inlet, an actuation voltage of 100 V and a frequency of 2.0 kHz. As shown in Fig. 3.19, the direction of the generated vortex is counter-clockwise and the process of the flow pattern development is almost symmetric about the centerline compared to the previous ones. The intensity of the counter-clockwise vortex was plotted versus time in Fig. 3.19. It is found that about 7 seconds after the actuation is turned on, the vortex intensity reaches 30% and finally, at 50 seconds when the flow is fully developed, the vortex intensity is up to 90%, which is as strong as the clockwise vortex generated under the same conditions.

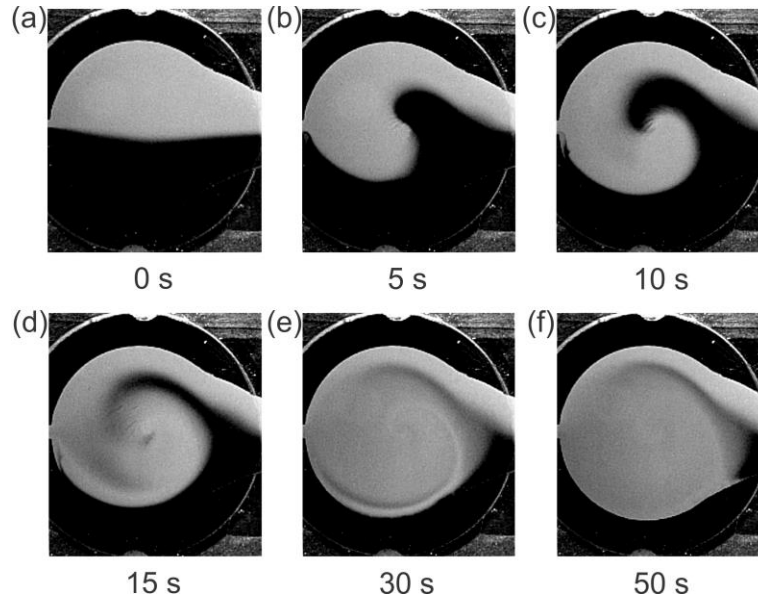


Fig. 3.19 Visualization of the generated vortex in the counter-clockwise direction. The actuation frequency was 2.0 kHz, the voltage 100 V and the flowrate 2 mL/h at each inlet.

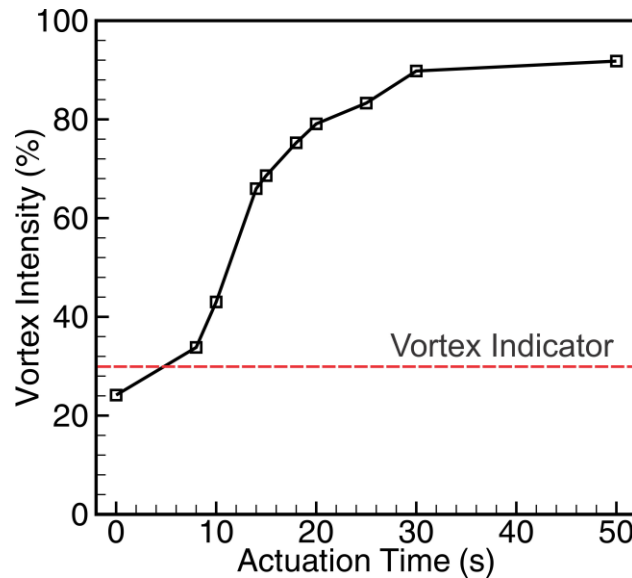


Fig. 3.20 The intensity of a counter-clockwise vortex versus time after the actuation is turned on. The actuation frequency and voltage were fixed at 2.0 kHz and 100 V, and the flowrate 2 mL/h at each inlet.

We also found that only one regime of vortex can be generated in one specific assembled device and it is impossible that one device can have two regimes of vortices no matter how the actuation conditions are adjusted. Besides, the occurrence chance of the two types of vortices is approximately equal: when we fabricate ten devices, clockwise vortex appears in about five devices and counter-clockwise vortex in the other five.

3.3 Summary

In this chapter, a novel method to generate vortices in a specially designed microfluidic chamber with PZT actuations is presented. Experimental studies have been conducted on vortex generation for liquid flows in this chamber. The vortices under the actuation have been visualized and characterized in terms of the actuation voltages, frequencies and flowrates.

The results show that by applying actuations, large-scale vortices can be generated inside the chamber, in which only laminar flows would exist otherwise. A frequency window is identified, in which the vortex generation is possible. The vortex intensity is less than 20% at 40 V, and increases to 90% with the actuation voltage equal to 100 V. Bubbles may be induced in the chamber when the actuation voltage exceeds a threshold. It is also found that the resonator-shaped nozzle which the microfluidic chamber is featured with can contribute to much stronger vortices than a common circular chamber. The vortices generated in the chamber can be clockwise or counter-clockwise while only one regime of vortex can be generated in one specific device and it is impossible that one device can have two regimes of vortices. This method of vortex generation is advantageous in many aspects: it has no requirements on the flowrates and properties of working fluids such as conductivity or magnetism; it can generate large-scale vortices without the need to introduce and trap external gas in advance; it is non-intrusive and damage-free without obvious temperature rise. All these advantages are favorable for this method of vortex generation to be applied in flow control of microfluidic manipulations including mixing enhancement and distribution of microparticles and nanoparticles.

Chapter 4 Vortex Generation in a Microfluidic Chamber: Control and Mechanism

4.1 Introduction

In last chapter, it has been demonstrated that the vortices can be generated in a specially designed microfluidic chamber with PZT actuations and the flow pattern and vortex intensity can be modulated by varying the actuation conditions, including the actuation frequency, applied voltage and flowrate. The generated vortices can be rotated in either clockwise or counter-clockwise direction. However, in one specific device, only one regime of vortex can occur no matter how the actuation conditions are regulated.

In this chapter, the microfluidic chamber is modified to have two regimes of vortices – clockwise or counter-clockwise in one device. The vortex direction and intensity are regulated conveniently by varying the operation conditions. The mechanism of the vortex generation and control is explored by comparing with the instability of the flow through a sudden expansion or a rectangular chamber. Specifically, the flow velocity in the outlet channel at various actuation frequencies is measured in order to support our explanation about the mechanism of the vortex generation. The vibration displacement and velocity of the PZT disk are measured to investigate the relation between the vibration and the frequency window for vortex generation and flow velocity.

4.2 Experimental methods

4.2.1 Modification of the microfluidic chamber and experimental setup

As shown in Fig. 4.1(a-b), the configuration and dimension of the microfluidic chamber used in the experiment are the same as previously except that the ceramic layer of the PZT disk is divided into two transducers which can be actuated separately – Transducer A and Transducer B. The working transducer of the PZT disk can be altered conveniently via a switch without interrupting the flow or exchanging the device. Three inlets, instead of two inlets, are smoothly connected to the chamber through a straight channel at an angle of 36 degrees. The modified microfluidic chamber for vortex generation is illustrated in Fig. 4.1(c).

The microfluidic chamber is fabricated using the same method in last chapter. The schematic of the experimental setup is illustrated in Fig. 4.1(d). To visualize the flow patterns of the generated vortices in clockwise or counter-clockwise direction, the DI water with fluorescent dye is supplied to Inlet 2 in the middle and the degassed DI water without fluorescent dye is supplied to the microfluidic chamber at Inlets 1 and 3. The vortex intensity along the straight line C-O-C' is calculated in terms of Eq. (3.2) for quantitative analysis. In the experiment, Transducer A was triggered at first and meanwhile the flow patterns were recorded; when the flow was fully developed, the actuation was turned off; after the flow was resumed to its original state, Transducer B was triggered.

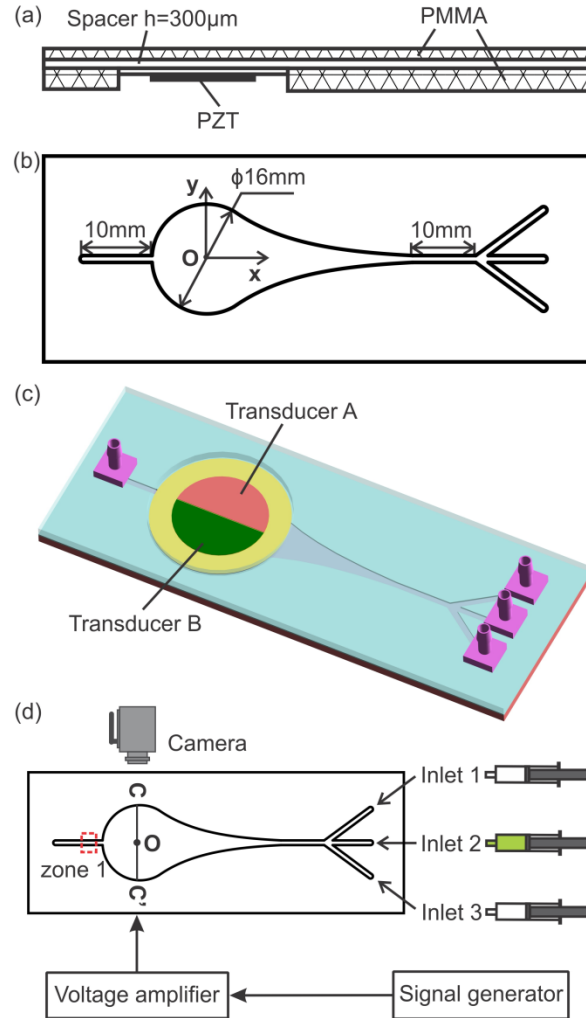


Fig. 4.1 Illustration of the modified microfluidic chamber and experimental setup. (a) Side view of the configuration. (b) Top view and geometric dimensions of the configuration. (c) Schematic illustration of the assembled device. (d) Schematic illustration of the experimental setups. The velocity in the rectangular region – zone 1 is measured.

A piezoelectric actuator converts an electrical signal in terms of voltages into a mechanical displacement (called a stroke). As shown in Fig. 4.2(a), the two separate transducers are affixed to a circular brass sheet to form the PZT disk and the PZT disk will be vibrating as a whole when either transducer is actuated. When the semi-circular transducer – Transducer A or B is actuated, the vibration of the PZT disk is considered as the small deflection of a thin circular plate with off-center loads. As illustrated in Fig. 4.2(b-c), the “vibration center” – the point in the PZT disk with maximum amplitude is not located at its geometric center, so that the flow induced by the actuations is asymmetric and the asymmetry is controllable. In the experiments, the flows were recorded by a camera from the top of the PMMA plate opposite to the PZT disk and thus,

Transducers A and B in Fig. 4.2(a) are shown upside down compared to the illustration in Fig. 4.1(c).

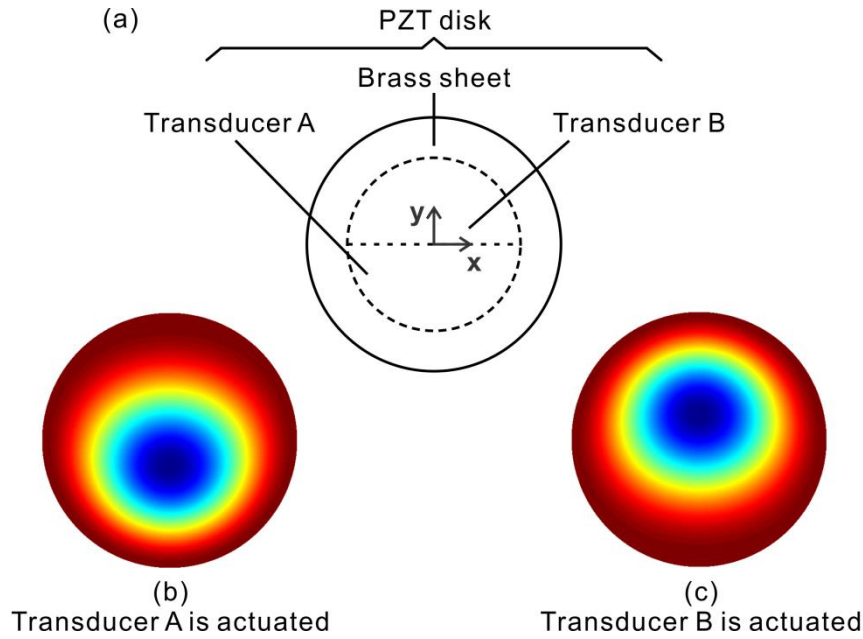


Fig. 4.2 (a) Illustration of the PZT disk. The PZT disk consists of two separate transducers and a brass sheet. (b) The vibration profile of the PZT disk when Transducer A is working. (c) The vibration profile of the PZT disk when Transducer B is working.

4.2.2 Measurement of the flow velocity in the outlet channel

In the traditional PIV (Particle image velocimetry) technique, the velocity field of a flow can be quantitatively measured by tracing the motions of the particles in the fluids. The tracer particles throughout a region are recorded using the multiple exposure method and the velocity field is obtained by calculating the displacement of the particles during the known time interval. The illumination is most commonly provided by a laser sheet. However, due to the limits of laser sampling rate and image transfer capacity, the PIV measurement is not suited to be applied to the flows actuated at high frequencies. For example, the common 15 Hz dual-head pulsed Nd:YAG laser can only capture 15 recordings at most within one second, which is far from our demand. Therefore, we take advantage of the high-speed camera to record the patterns of the flow with particles at first and then transfer the images to the PIV software platform to calculate the particle displacement of two consecutive images. In the experiments, at the frequency of 1.5

kHz, the sampling rate of recording the images is 21,000 fps, namely 14 images captured in one cycle.

The measurement of the transient velocity in the rectangular region – zone 1 is illustrated in Fig. 4.3. The flow patterns of the fluids which are seeded by micro-sized particles are recorded by the CCD camera and then analyzed through a PIV software platform (DynamicStudio, Dantec Dynamics, Denmark). In order to obtain high quality signal with around 2-5 particles per interrogation spot, the traceable polystyrene microspheres (Fluoro-Max, Diameter $4.8\mu\text{m}$, Thermo Scientific) was diluted with degassed DI water to act as the working fluid. The velocity field of the flow was obtained by calculating the particle displacement of two consecutive images by means of DynamicStudio.

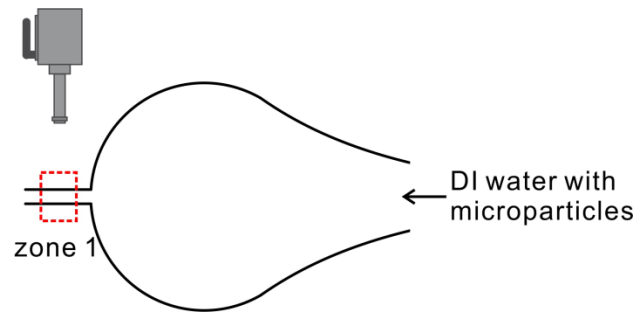


Fig. 4.3 Schematic illustration of the measurement of the velocity field in the outlet channel. The velocity in the rectangular region – zone 1 is measured.

4.3 Results and discussion

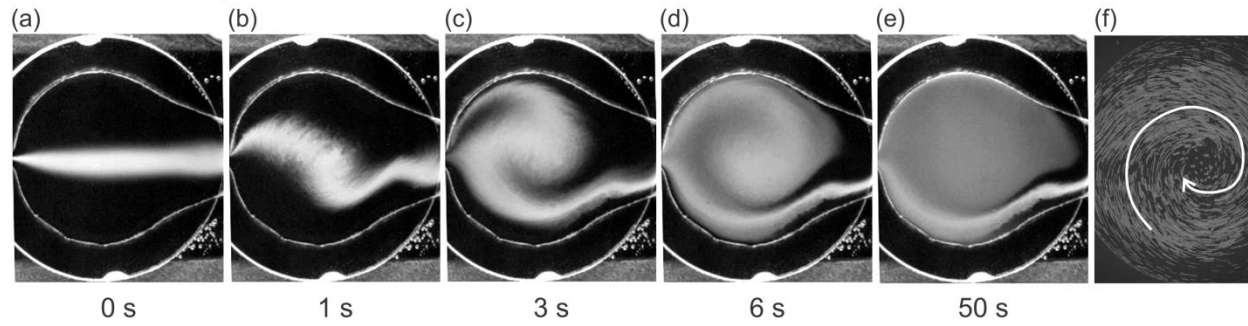
4.3.1 Visualization of vortex generation and control by fluorescent dyes

Using the fluorescent dye as flow tracers, the flow patterns inside the microfluidic chamber were recorded by the camera after the actuation was switched on. The flowrates for the three inlets, 1, 2 and 3 were respectively set as 4.5 mL/h, 1 mL/h and 4.5 mL/h such that the total flowrate through the chamber was 10 mL/h. The PZT disk was actuated at 100 V and 1.5 kHz. The flow pattern development with time for Transducers A and B is presented in Fig. 4.4(a-e) and Fig. 4.4(g-k), respectively. It is seen that, without actuations (Fig. 4.4(a) and 4.4(g)), the fluids flow separately through the chamber and the interface between the fluids is very clear, which means that the flow is laminar. Within a few seconds of turning on the actuation, the

fluorescent-dyed fluids which come from Inlet 2 are distorted and swirled to the whole chamber as shown in Fig. 4.4(b-d) and Fig. 4.4(h-j). In both cases, a large vortex is formed, occupying the whole chamber. However, the regime of the vortex is different for the two cases in terms of the vortex direction: when Transducer A is actuated, the vortex rotates in the clockwise direction, which is denoted as CW vortex; when Transducer B is actuated, the formed vortex is in the counter-clockwise direction, which is denoted as CCW vortex. In Fig. 4.4(e) and 4.4(k), the fluorescent fluid is continuously swirled and finally, the interface between the fluids disappears and the flow is fully developed. In addition, we also used the suspension of microparticles in the flow as the tracer to display the flow characteristics of the generated vortices by stacking a large amount of images of the fluid flow at various moments. As shown in Fig. 4.4(f) and 4.4(l), the traces of particles clearly present the generated vortices in the chamber, in accordance with the flow patterns of fluorescent dyes. It is noticeable that the generated vortices are three dimensional in essence because the flow is induced by the up-and-down vibration of the PZT disk in the height direction.

In the experiments, the two regimes of vortices are similar to those generated in the chamber actuated by a complete circular transducer; while the vortex direction can be shifted conveniently by selecting the working transducer without altering the device or interrupting the flow, which is different from the vortex reported in Chapter 3. These features are novel and useful, which can promote the maneuverability of microfluidic operations for mixing enhancement of multiple reagents and distribution of microparticles and nanoparticles.

The vortex development with Transducer A actuated



The vortex development with Transducer B actuated

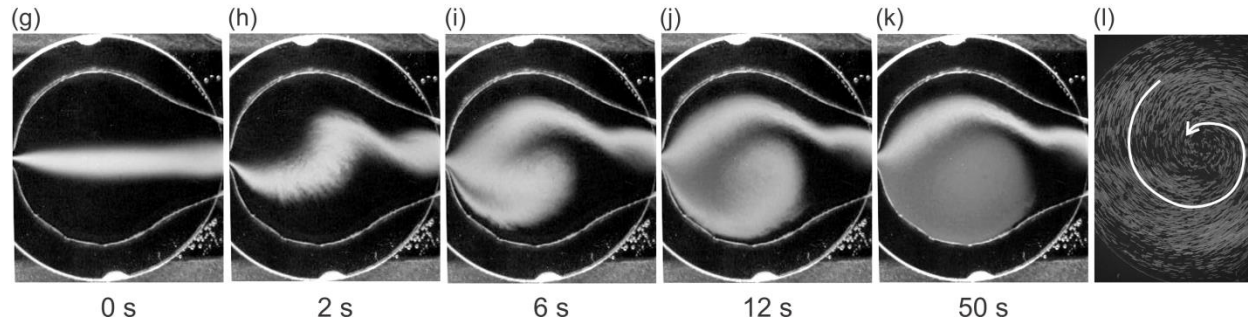


Fig. 4.4 Recorded images of the flow pattern development with time. Clockwise vortex (CW vortex) is generated when Transducer A is actuated (a-e) and counter-clockwise vortex (CCW vortex) is generated when Transducer B is actuated (g-k). The actuation voltage and frequency are 100 V and 1.5 kHz respectively, and the flowrate is 10 mL/h in total. The traces of particles of CW vortex (f) and CCW vortex (l) are in accordance with the flow patterns of fluorescent dyes, respectively.

4.3.2 Effects of actuation conditions on the generated vortices

The effects of the actuation conditions such as the actuation frequency, voltage and flowrate on the generated vortices are investigated to regulate the vortical flow. The dependence of the vortex on actuation frequency is presented in Fig. 4.5. The frequency is varied from 1 kHz to 4.5 kHz, and the applied voltage and flowrate are 100 V and 10 mL/h respectively. The flow patterns in Fig. 4.5 were recorded when the flows were fully developed at 50 s, and the vortex intensity at this time was calculated. From Fig. 4.5, it is clear that when either Transducer A (solid line) or Transducer B (dashed line) is actuated, there exists an effective frequency window for vortex generation. Within the frequency window between 1.5 kHz and 3 kHz, the generated vortex is quite strong, and the vortex intensity indicator is higher than 80%. The intensity of both CW vortex and CCW vortex reaches a maximal at 2.5 kHz. When the actuation frequency is lower than 1 kHz or higher than 4 kHz, the vortex becomes very weak or even unable to occur in the chamber, and thus the vortex intensity is below 15%. It is also found that the vortex direction

keeps unchanged when varying the applied frequency: CW vortex is generated only when Transducer A is actuated, and CCW vortex occurs only when Transducer B is actuated.

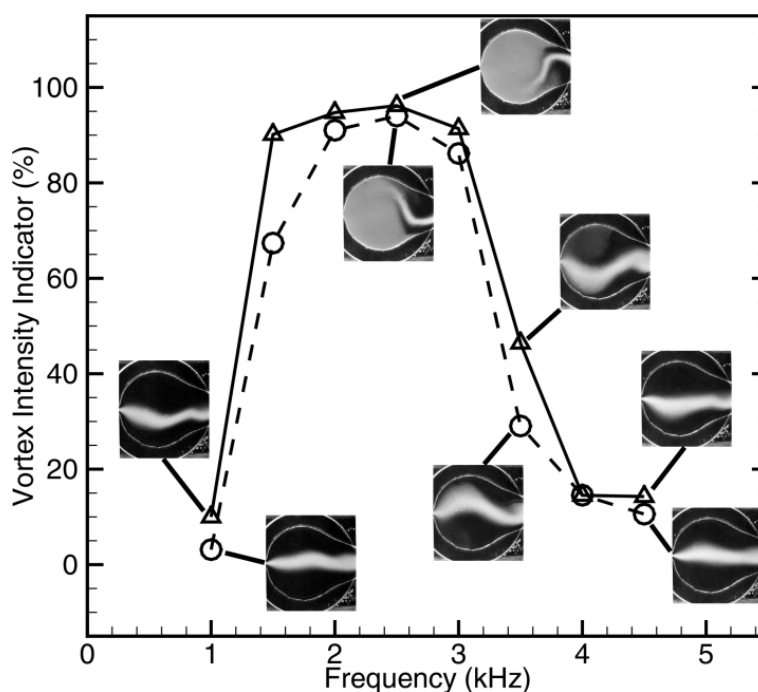


Fig. 4.5 Effect of actuation frequency on the generated vortex when Transducer A (solid line) or Transducer B (dashed line) of the PZT disk is actuated. The actuation voltage is 100 V and the flowrate is 10 mL/h in total. All the flow patterns are recorded at 50 s.

A further investigation was conducted by varying the actuation voltage from 40 V to 100 V while keeping the frequency and flowrate as 1.5 kHz and 10 mL/h, respectively. The results when Transducer A (solid line) or Transducer B (dashed line) is actuated are presented in Fig. 4.6. The inset images were recorded when the flow patterns were fully developed at 50 s and the vortex intensity at this time was calculated. At 40 V, the fluids with fluorescent dye are slightly distorted in the chamber for both cases, indicating that the vortex is very weak. When the applied voltage is varied from 60 V to 100 V, a large vortex occurs inside the chamber and the vortex intensity increases greatly with the applied voltage while the vortex direction keeps unchanged. At 100 V, the intensity of CW vortex is as high as 90% when Transducer A is actuated and the intensity of CCW vortex reaches up to 67% when Transducer B is actuated. It is also found that with increasing actuation voltages, the intensity indicator of CW vortex is larger than that of CCW vortex on the whole.

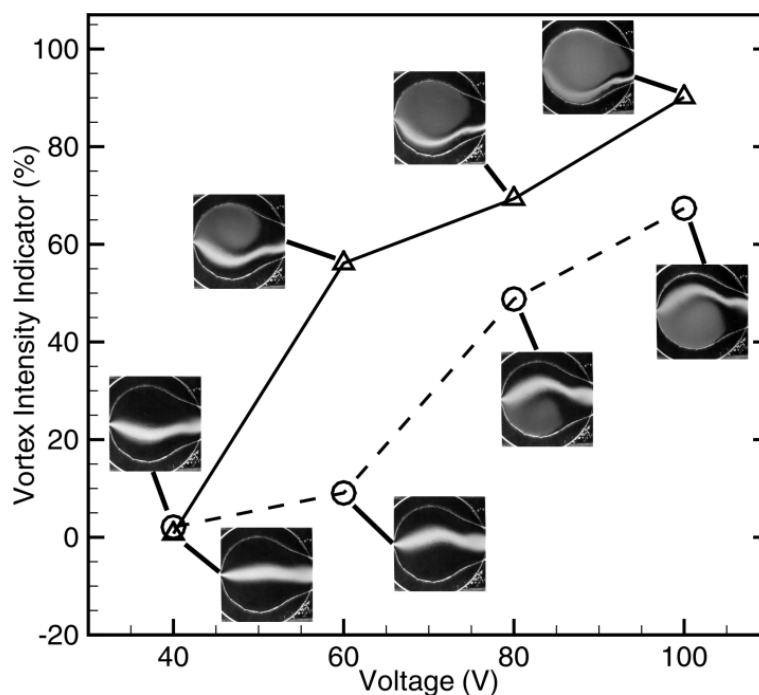


Fig. 4.6 Effect of the actuation voltage on the generated vortex when Transducer A (solid line) or Transducer B (dashed line) of the PZT disk is actuated. The actuation frequency is 1.5 kHz and the flowrate is 10 mL/h in total. The inset images are recorded when flows are fully developed at 50 s.

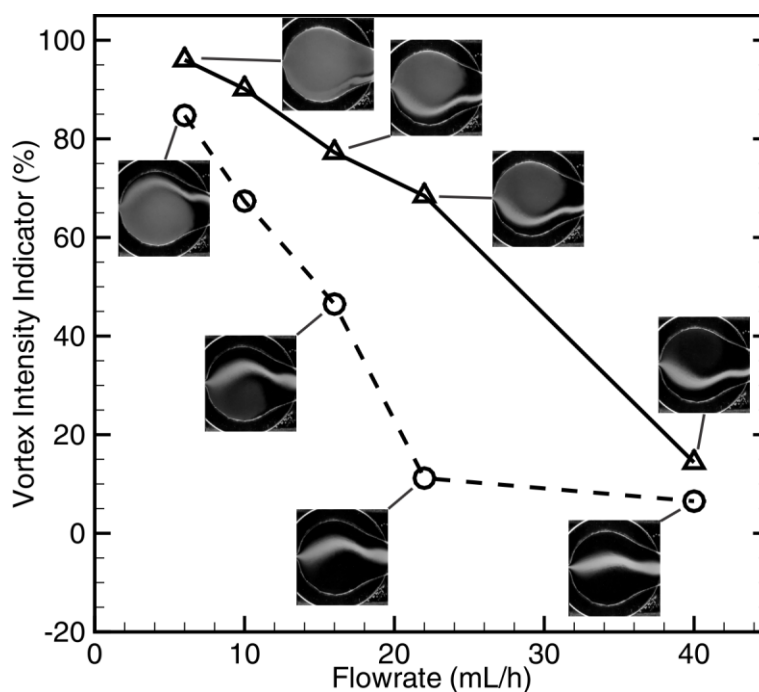


Fig. 4.7 Effect of flowrate on the generated vortex when Transducer A (solid line) or Transducer B (dashed line) of the PZT disk is actuated. The actuation frequency is 1.5 kHz and the voltage is 100 V, respectively. The inset images are recorded when flows are fully developed at 50 s.

To study the effects of the flowrate on the performance of the vortex generation, the total flowrate was set as 6 mL/h, 10 mL/h, 16 mL/h, 22 mL/h and 40 mL/h while the ratio for the three inlets, 1, 2 and 3 was maintained constant at 4.5:1:4.5 for all cases. The driving frequency was fixed at 1.5 kHz and the voltage is 100 V. The working fluids are DI water. It shows that for both cases, the vortex intensity decreases with the increasing flowrate (Fig. 4.7). At the flowrate of 6 mL/h, the vortex intensity reaches up to 90% and at low flowrates the strong vortices are relatively easy to be generated. The vortices are relatively weak at high flowrates, even unable to be generated, for example, the vortex intensity is dropped to below 10%, when the total flowrate is increased to 40 mL/h. It is also found that the different flowrates can only change the vortex intensity and the vortex direction keeps unchanged: CW vortex is generated only when Transducer A is actuated, and CCW vortex occurs only when Transducer B is actuated. Therefore, except for the vortex direction, the vortex intensity can also be tuned conveniently by varying the applied frequency, voltage or the flowrate.

In Fig. 4.5 – 4.7, although the direction of the CW and CCW vortex is opposite, the vortex intensity of Transducer A and Transducer B should be equal in ideal circumstances. However, due to the manufacturing challenges in such a small scale, the real device fabricated in experiments is not perfectly symmetric about the mid-plane where the x-axis is located and this kind of configuration asymmetry results in the difference of the intensity of CW and CCW vortex. The configuration asymmetry may originate from: (i) the transducer may not be perfectly separated into two parts; (ii) the PZT disk may not be concentric with the chamber; (iii) soldering tin of the wires on the PZT disk results in the asymmetry of the mass distribution of the PZT disk.

4.3.3. Mechanism of vortex generation and control

It has been demonstrated, in the previous sections, that the vortices can be generated in the microfluidic chamber incorporated with actuators and the vortex directions can be controlled by varying the actuation conditions. Regarding the mechanism, we propose that the vortex generation in the present study is induced by the instability of the actuation-induced pulsatile flow through the sudden expansion part at the outlet of the chamber, while the vortex control is realized through the asymmetric flows in the chamber induced by the upper or lower transducers.

Acoustic streaming is a second order nonlinear effect where the presence of an oscillatory flow generates steady mean vortical flows [94-95]. However, the acoustic streaming relies on momentum transfer from the acoustic waves – standing waves or travelling waves – to the fluid [95]. Herein, the typical actuation frequency for vortex generation is 1.5 kHz and the actuation pressure wavelength is about 1 meter (taking the sound speed in water to be 1500 m/s). While the largest dimension of the microfluidic chamber in our study is about 0.07 m, which is much smaller than the pressure wavelength. As a result, the actuation pressure is almost uniformly distributed in the microfluidic chamber and no acoustic wave exists in the chamber at all. In other words, the fluid is incompressible inside the chamber in the present actuation frequencies, which indicates that acoustic streaming is not the mechanism of the vortex generation in the present microfluidic chamber.

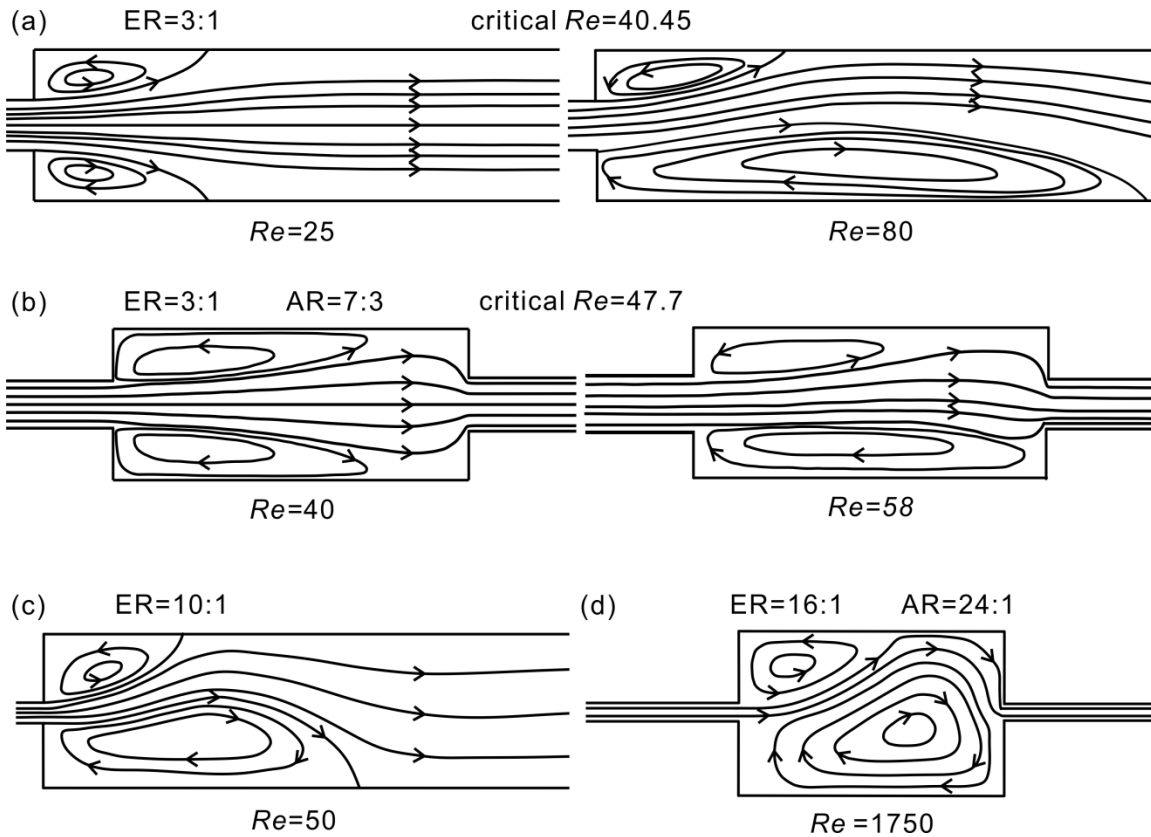


Fig. 4.8 Illustration of the flow through a sudden expansion or rectangular chamber. (a) The flow transition from a pair of symmetric vortices to asymmetric at high Reynolds number. [96] (b) Transition of the flow in a rectangular chamber from symmetric to asymmetric when the Reynolds number is above the critical value. [98] (c) The asymmetric flow in a sudden expansion with a large expansion ratio at high Reynolds number. [100] (d) The asymmetric flow in a rectangular chamber with a large expansion ratio at high Reynolds number. [101] ER is the expansion ratio.

It has been reported that the symmetric flow through a sudden expansion yields to a pair of stable and asymmetric vortices – a large vortex on one side and a small one on the other side, due to the instability of the flow at high Reynolds number [96-101]. As shown in Fig. 4.8(a), Fearn et al. [96] studied the flow in a symmetric expansion experimentally and numerically and showed that in a channel of expansion ratio (ER) equal to 3:1, the asymmetric vortices arose instead of a pair of symmetric vortices due to the symmetry-breaking bifurcation when Re was above 40.45. Shapira and Degani [97] demonstrated that the asymmetric vortices can not only be formed in a “sudden” expansion but also in a “smooth” expansion, and the critical Reynolds number for the flow instability increases with the degree of “smoothness” of the expansion. For example, for a 3:1 expansion ratio, the critical Reynolds number becomes 147 for an expansion of 10° semi-angle. Mizushima et al. [98] investigated the transition of the flow through a rectangular chamber with ER equal to 3:1 and aspect ratio (AR) equal to 7:3 (Fig. 4.8(b)). They found that the steady and symmetric flow became two vortices of unequal size when Re was larger than 47.7. Further investigations show that in the case of a large expansion ratio, the asymmetry of the two uneven-sized vortices in the flows through a sudden expansion or a rectangular chamber is greatly enhanced due to the reduction of the flow stability, as illustrated in Fig. 4.8(c-d) [99-101]. Revuelta demonstrated that the asymmetric vortices in the flow through an expansion of large expansion ratios tended to appear for lower values of Reynolds number due to the momentum exchange between the incoming jet and the recirculating fluids [100]. Dufresne et al. studied the flow fields in a rectangular shallow basin at high Reynolds number and found that in the chamber with ER =16:1, the asymmetric flow had two vortices with distinct sizes: compared to the case of ER =3:1, a larger vortex was formed inside the chamber and a smaller vortex was formed on the upper corner [101]. In addition, researchers demonstrated that even for a pulsatile flow through an expansion channel or a rectangular chamber, the transition to asymmetric vortices from a pair of symmetric vortices can also occur as a result of the flow instability and the periodicity of the flow is lost when the Reynolds number exceeds the critical value [102-103].

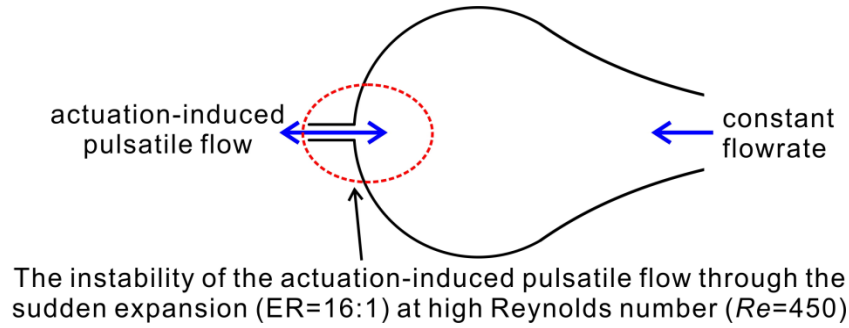


Fig. 4.9 The fluids flow into and out of the chamber through the outlet channel with the vibration of the PZT disk.

In our study, the PZT disk vibrates in the height direction and leads to the variation of the chamber volume. Since the flowrate at the inlets is maintained constant, the outlet channel becomes the only passage of the actuation-induced flow. Therefore, due to the conservation law of mass, the fluids are actuated into and out of the chamber through the outlet channel corresponding to the sucking and squeezing phase of the PZT disk, as shown in Fig. 4.9. The ratio of the diameter of the circular chamber (16mm) versus the width of the outlet channel (1mm) reaches up to 16 which is a sudden expansion of a large expansion ratio. Therefore, the vortex generation in our study is probably induced by the instability of the actuation-induced pulsatile flow through the sudden expansion part of the outlet channel at high Reynolds number and the different vortex directions are realized through the asymmetric flows caused by asymmetric actuations of the upper or lower transducer as illustrated in Fig. 4.10.

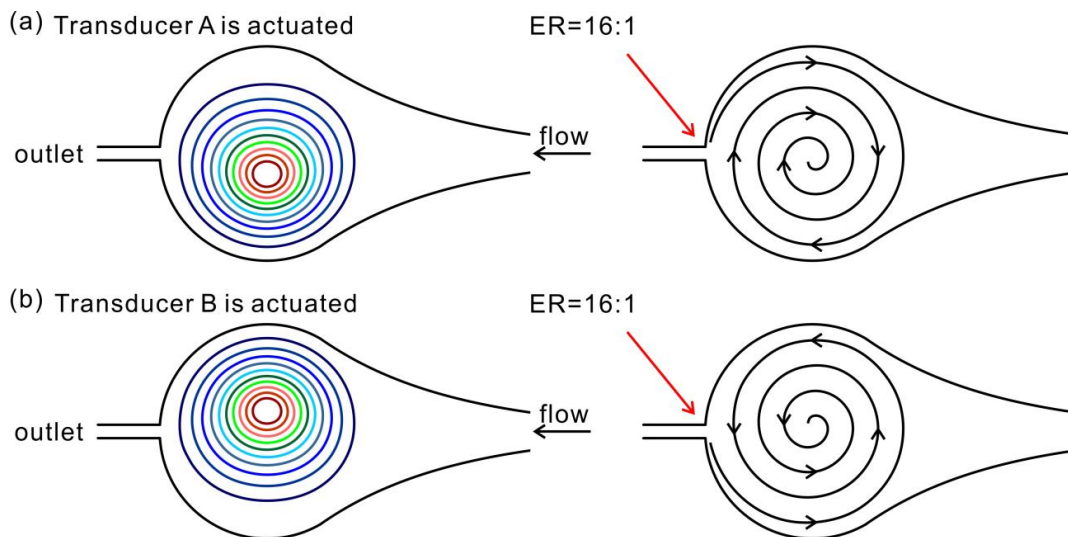


Fig. 4.10 The fluids flow through a suddenly expanded part with a very large expansion ratio (ER) in the outlet channel when the PZT disk is vibrating.

4.3.4. The flow velocity in the outlet channel

In order to support our aforementioned assumption of the vortex generation, the transient velocity of the flow through the outlet channel of the chamber was measured to obtain the Reynolds number. A rectangular region – zone 1 (indicated in Fig. 4.3) was selected to measure the time-dependent flow velocity in the outlet channel. The flow patterns of the fluids which were seeded by micron-sized particles were recorded by the high-speed camera and the images are analyzed through a PIV software platform to calculate the flow velocities. In the experiments, the applied voltage and flowrate were 100 V and 10 mL/h, respectively. Figure 4.11 exemplifies the velocity fields in the outlet channel at six moments of one cycle for the experiment at 1.5 kHz. The sampling rate of the camera was 21,000 fps, which means 14 records every cycle. It is clear that the flow is similar to a plug flow with very thin boundary layer, and the direction and magnitude of the flow velocity are periodic with time.

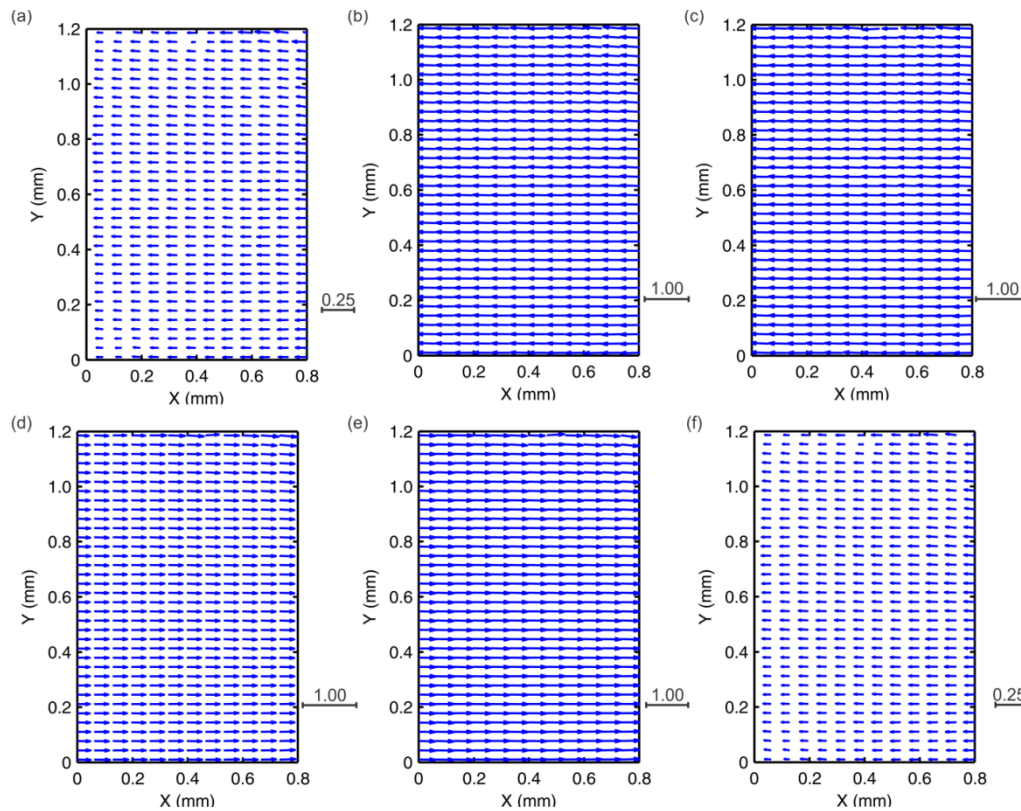


Fig. 4.11 The velocity fields in the outlet channel at six moments of one cycle when the actuation frequency is 1.5 kHz.

The flow velocity in the channel varies with the positions and thus the mean velocity across the outlet channel is calculated. The cross-section mean velocity \bar{u} in the outlet channel is plotted with time in Fig. 4.12. It can be seen that when the transducer A (solid line) or transducer B (dashed line) is actuated, the mean flow velocity fluctuates sinusoidally, indicating that the flow through the outlet is pulsatile corresponding to the vibration of the PZT disk. The peak velocity \bar{u}_p of the pulsatile flow reaches up to 0.45 m/s for both cases. This flow velocity is much greater than the mainstream velocity (0.01 m/s, denoted by red dashed line), which means that the actuation-induced flow by the PZT disk is much greater than the stream flow from inlets. By taking $\bar{u}_p = 0.45$ m/s as the characteristic velocity, outlet channel width (= 1 mm) as the characteristic dimension, and water as the working fluid, the Reynolds number is calculated to be 450, which is large enough for the flow instability in a sudden expansion of ER equal to 16 to generate vortices. The high Reynolds number justifies the proposed mechanism of vortex generation from one perspective.

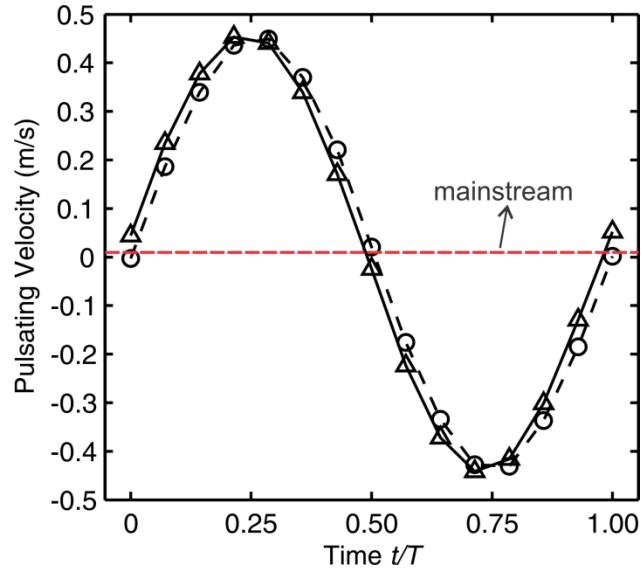


Fig. 4.12 The variation of the cross-section mean velocity in zone 1 of the outlet channel with time in one cycle when Transducer A (solid line) or Transducer B (dashed line) is working.

The peak-to-peak velocity or the velocity amplitude is defined as a half of the difference between the maximum value and the minimum value during one cycle. To study the effects of the actuation frequency on the flow velocity, we plot the flow velocity amplitude versus the actuation frequency in Fig. 4.13. It can be found that there also exists a frequency window for the

flow velocity amplitude: within the frequency range between 1.5 kHz and 3 kHz, the amplitude of the pulsatile velocity is very large, about 0.4 m/s, while out of this frequency range, the velocity amplitude dramatically drops to 0.1 m/s. This frequency window of the velocity amplitude is in accordance with the frequency window for the vortex generation shown in Fig. 4.5, which supports our aforementioned assumption of the vortex generation from another perspective.

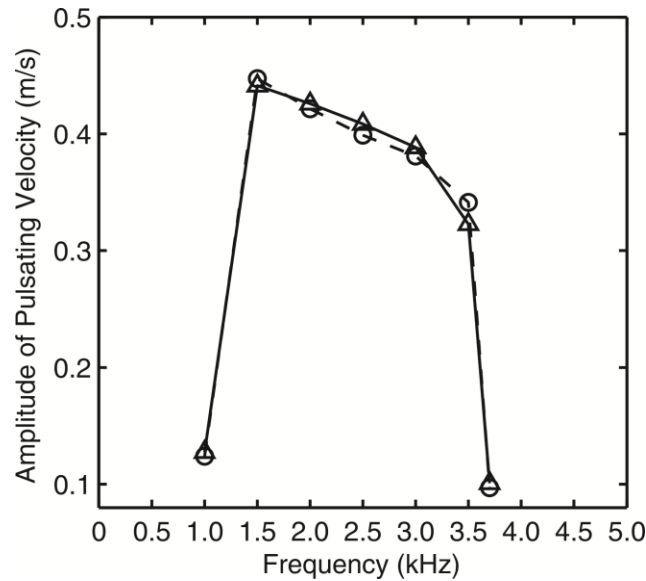


Fig. 4.13 The effect of the actuation frequency on the amplitude of the pulsatile velocity in the outlet channel when Transducer A (solid line) or Transducer B (dashed line) is actuated.

In summary, we can state the mechanism of the vortex generation and control as follows: when the PZT disk is actuated, the fluids periodically flow into/out of the chamber through a suddenly expanded part with very large expansion ratio; at the proper actuation conditions, the velocity of the pulsatile flow is very large that the flow loses its stability at high Reynolds number; as such, a large vortex is formed in the chamber throughout the entire cycle of the actuation and the regime of the generated vortex is dependent on the asymmetric flow induced by the different working transducer of the PZT disk [104].

4.3.5. Vibration measurement of the PZT disk

The frequency window (1.5 kHz – 3.5 kHz) for the vortex generation or flow velocity in the channel is associated with the natural frequency of the diaphragm. As shown in Fig. 4.14, to explore the relation between the vibration of the PZT disk and the frequency window of vortex generation and flow velocity, we measured the vibration velocity amplitude (maximum vibration velocity) of the center of the PZT disk (point O) as a function of the forcing frequency by means of LDV (Laser Doppler Vibrometer, PSV300, Polytec Ltd., UK) technique.

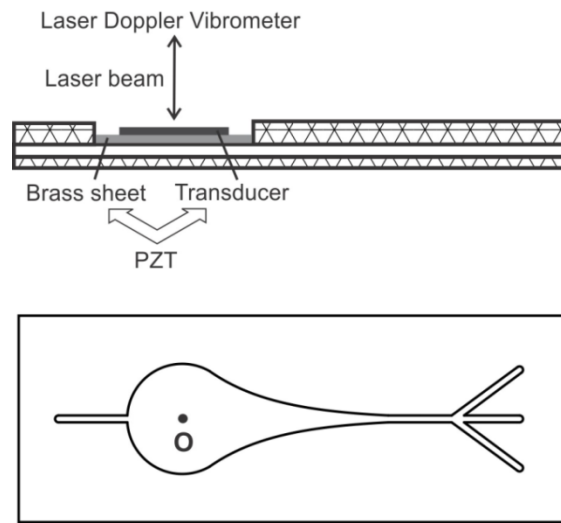


Fig. 4.14 Schematic illustration of the experimental setup for measuring the vibration velocity and displacement of the PZT disk.

The amplitude of the vibration velocity is plotted with the actuation frequency in Fig. 4.15(a). We can see that there is a frequency window for the vibration velocity amplitude between 1.5 kHz and 3 kHz and it is agreeable with the frequency range for the vortex generation or the flow velocity amplitude in the previous sections. The vibration displacement amplitude of the center O is shown in Fig. 4.15(b). We can see that the frequency dependence in Fig. 4.15(b) does not match the frequency window for the vortex generation or the flow velocity in the outlet channel. Thus, the measurement results of the vibration of the PZT disk show that the frequency window for vortex generation or flow velocity in the outlet channel matches the frequency range for the vibration velocity of the PZT disk instead of the vibration displacement of the PZT disk.

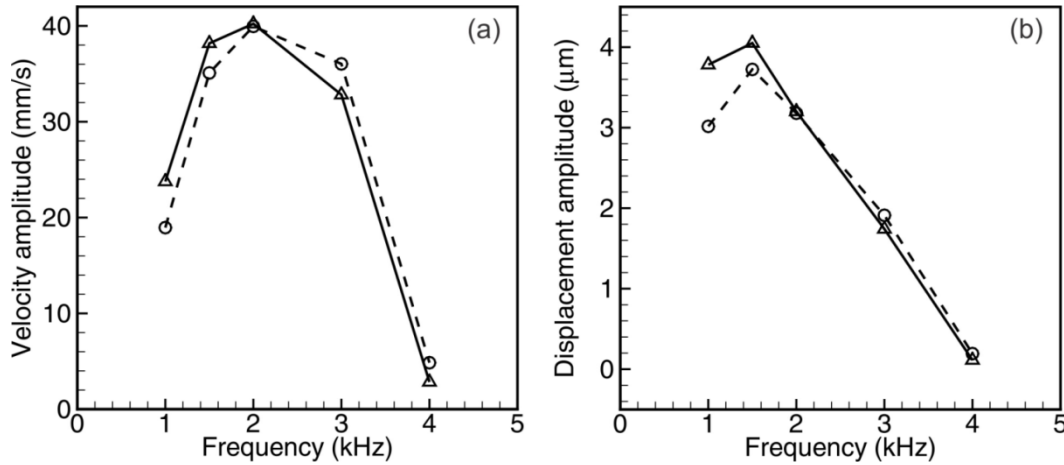


Fig. 4.15 (a) Vibration velocity amplitude of the center O with the actuation frequency. (b) Vibration displacement amplitude of the center O with the actuation frequency. Solid line – Transducer A is working; Dashed line – Transducer B is working.

This agreement can also be explained in terms of the actuation-induced flow by the PZT disk. We illustrate the side view of the microfluidic chamber in Fig. 4.16. The vibration of the PZT disk leads to the variation of the chamber volume and the fluids are actuated into and out of the chamber through the outlet channel since the flowrate at inlets are constant at 10 mL/h controlled by pumps. It means that due to conservation of mass, the flowrate at the outlet is approximately equal to the change rate of the chamber volume because the mainstream flow from inlets is negligible (0.01 m/s versus 0.4 m/s). In another word, the flowrate or the mean velocity in the outlet channel is proportional to the vibration velocity of the PZT disk rather than the vibration displacement of the PZT disk. Therefore, the frequency window for vortex generation or flow velocity in the outlet is agreeable with the frequency range for the vibration velocity of the PZT disk, rather than the vibration displacement of the PZT disk.

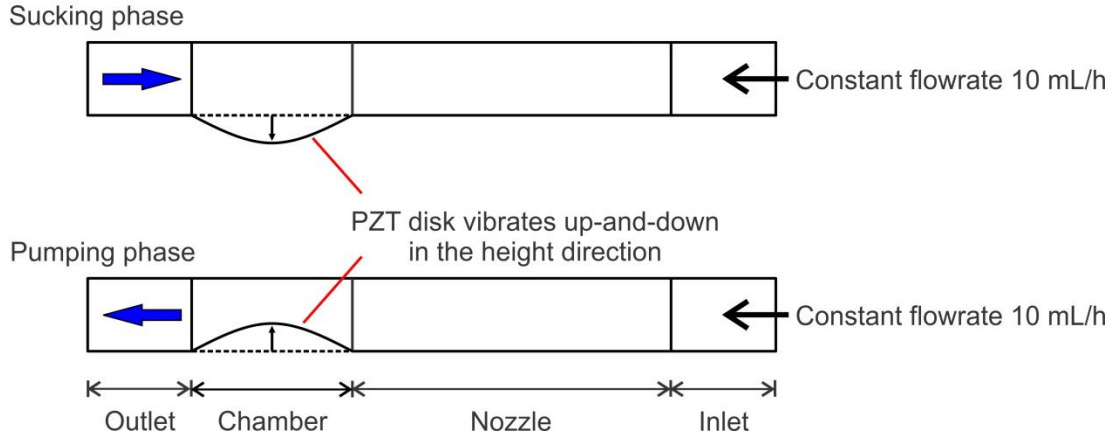


Fig. 4.16 Side view of the microfluidic chamber for vortex generation. The fluids are actuated into and out of the microfluidic chamber due to the volume change corresponding to the PZT vibration.

4.4 Summary

This chapter presents a modified microfluidic chamber for vortex generation and control based on the aforementioned microfluidic chamber with PZT actuations. The transducer of the PZT disk is divided into two parts which can be actuated separately. The generated vortex is visualized by tracing fluorescent dyes in the fluid and recorded by a CCD camera. The results show that two regimes of vortices – CW (clockwise) vortex and CCW (counter-clockwise) vortex can be formed inside a microfluidic chamber with actuations when the PZT disk is actuated at proper frequencies and voltages. The direction of the vortex can be shifted on-demand from clockwise to counterclockwise by simply switching between two different transducers and the vortex intensity can be tuned by the actuation frequency, voltage and flowrate.

To explore the mechanism of the vortex generation, PIV measurements have been conducted to obtain the flow velocity in the outlet channel. The results show that the flow in the outlet channel is pulsatile with the vibration of the PZT disk and the transient velocity is as high as 0.4 m/s at proper actuation conditions, leading to a large Reynolds number. A frequency window of the flow velocity amplitude is identified between 1.5 kHz and 3 kHz, which is in accordance with the frequency range for the vortex generation. The vortex generation in the chamber with actuations is due to the flow instability when the fluids are driven through the sudden expansion part of the outlet channel at high Reynolds number. Based on the vibration measurement of the PZT disk, it is found that the frequency window for vortex generation or flow velocity in the

outlet is agreeable with the frequency range for the vibration velocity of the PZT disk, rather than the vibration displacement of the PZT disk. The controllable vortex direction via a switch is a very novel and useful feature, which may promote the maneuverability of microfluidic operations for mixing enhancement of multiple reagents and distribution of microparticles and nanoparticles.

Chapter 5 Dynamics of multi-bubbles in a Microfluidic Chamber

5.1 Introduction

Bubble dynamics has been widely applied in lots of microfluidic processes, such as micropumping, micromixing, sorting, flow control and manipulation of micron-sized objects etc. However, the challenges of energy concentration, viscous surface force and low number of cavitation nuclei make it difficult to generate bubbles directly in microfluidic channels via the conventional acoustic method. The current methods of bubble formation in microfluidics include laser radiation and introduction of external gas. There are few reports about direct generation of bubbles in microfluidic systems. Besides, most studies on bubbles dynamics under actuations in microfluidics are focused on high frequencies, ranging from 20 kHz to several MHz. At low frequencies, the cavitation phenomena approach in a way hydrodynamic cavitation and the pressure wavelength will be long compared to the bubble size and microfluidic channel. As a result, the driving force to propel the bubble forward at low frequencies greatly differs from those at high frequencies. Therefore, the dynamics of bubbles in the microfluidic system, including the radial oscillation, translation and interactions with boundaries, needs to be thoroughly investigated.

In the previous chapters, we have demonstrated a new design of microfluidic chamber for vortex generation which takes advantage of PZT actuations. In the experiments, we observed that bubbles can be induced at the frequency of kilo-Hz range when actuation voltage is high enough. This phenomenon inspires us that it is an excellent method of bubble generation in microfluidics. Therefore, we investigate the dynamics of bubbles which are directly generated inside the microfluidic chamber, including the bubble generation, oscillation and translation. The bubbles can be generated in the microfluidic chamber within the frequency window between 0.5 kHz and 5 kHz. To reduce the influence of the vortex, we only investigate the flow actuated at the frequency of 1.0 kHz. Experiments are conducted to observe bubble generation, radial oscillation and translation by tracing fluorescent dyes in the flow and photographing the motions of the

bubbles in the nozzle part. Numerical simulation has been carried out using the commercial CFD software Ansys Fluent to elaborate the mechanism of bubble generation in the chamber.

5.2 Experimental methods

The microfluidic chamber used in the present study has the same configuration and dimension as described in Chapter 3. As shown in Fig. 5.1, the chamber contains two parts, a 16 mm diameter circular chamber and a nozzle with an acoustic resonator profile to achieve high amplitude pressure fluctuations. The chamber is made by two PMMA plates sandwiched by a dry adhesive layer with 300 μm in thickness (Arclad 8102 transfer adhesive, Adhesives Research, Inc.). Two inlets are connected at a 60-degree angle to the chamber by a straight channel of 10 mm in length and 1 mm in width, and another straight channel is connected to the other end of the chamber to form the outlet. A piezoelectric (PZT) disk is attached to the bottom of the circular chamber to provide actuation. The PZT disk consists of a PZT ceramic layer of 15 mm diameter and a brass sheet of 22 mm diameter. The height of the channel is controlled by the thickness of the adhesive layer. The geometry of the entire configuration is precisely manufactured by a laser cutting machine (Universal M-300 Laser Platform, Universal Laser Systems Inc., Arizona, USA). Finally, the inlets and outlet are assembled to the plate by epoxy glue (Araldite, Huntsman Advanced Materials, USA).

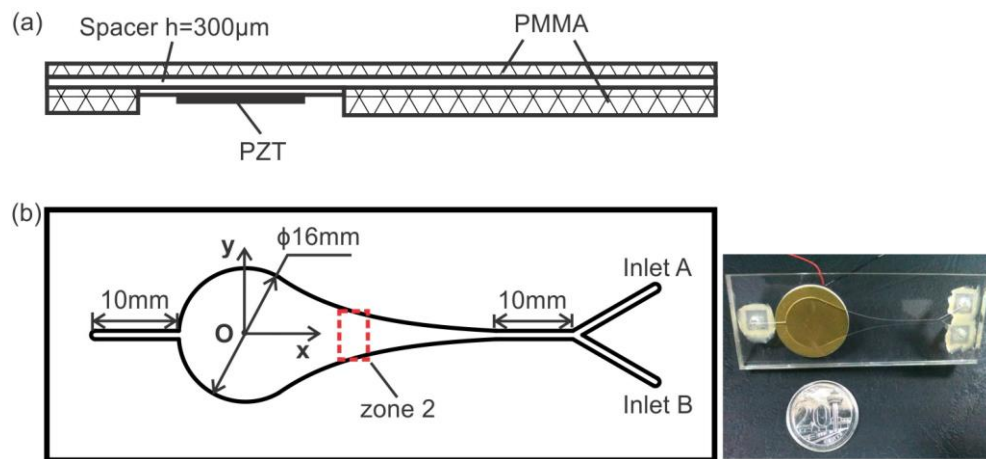


Fig. 5.1 Schematic illustration of the microfluidic chamber. (a) Side view of the configuration. (b) Top view of the chamber with geometric dimensions. The rectangular region zone 2 is selected to record the bubble's motion.

The schematic of the experimental setup is illustrated in Fig. 5.2. The working fluid, DI water, is supplied to the microfluidic chamber through two inlets. The flowrate is controlled by two syringe pumps (KD Scientific Inc., USA). The piezoelectric disk is driven by an external signal generator (33120A, Hewlett Packard) and an amplifier (790, PCB Piezotronics). A high speed CCD camera (Phantom V711, Vision Research, USA) is mounted on top of the chamber to record the flow field and bubble motion. In the experiments, we focused on the motion of the generated bubbles moving through zone 2 (indicated in Fig. 5.2). The actuation frequency is fixed at 1 kHz to weaken the effect of the vortex and the flowrate at each inlet is 5 mL/h.

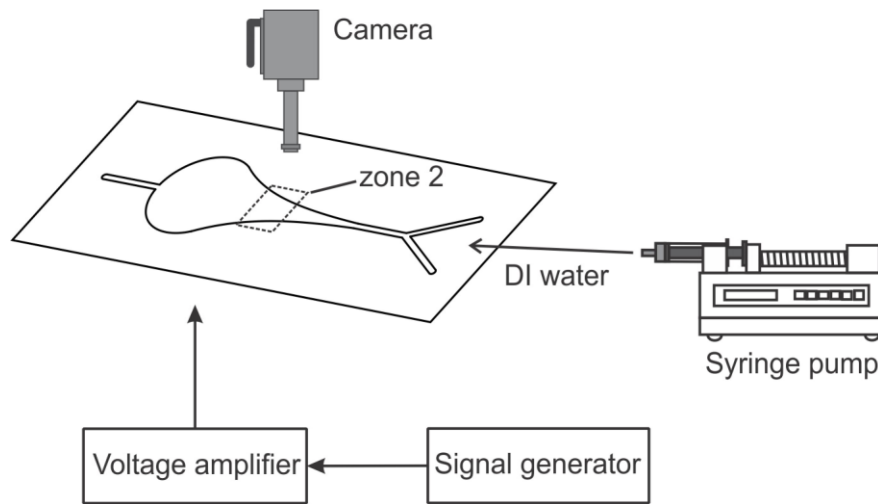


Fig. 5.2 Schematic illustration of the experimental setup.

5.3 Results and discussion

5.3.1 Visualization of bubble generation by fluorescent dyes

In order to visualize the bubble generation, development and moving tracks, the degassed DI water solution is supplied to the microfluidic chamber from inlet A (indicated in Fig. 5.1(b)), and the same DI water solution with fluorescent dye is supplied to inlet B. The total flowrate through the chamber is 10 mL/h. The PZT is actuated at 150 V and 1 kHz.

The images of the flow at different stages are presented in Fig. 5.3. It is seen that, without the actuation (Fig. 5.3(a)), the upper fluid (without fluorescent dye) and lower fluid (with fluorescent dye) flow separately through the chamber, and no bubbles are observed. As shown in

Fig. 5.3(b), after the actuation is switched on, a group of small bubbles are found to be generated in the area near the center of the chamber. As shown in Fig. 5.3(c), after being generated, the bubbles travel upstream against the hydrodynamic flow from the inlets, which is of great interests. The bubbles arrive finally at some position close to the upstream straight channel and keep relatively equilibrium (Fig. 5.3(d)). The violent oscillation, coalescence and breakup of the bubbles cause strong churning of the fluids, so as to enhance the mixing of the fluids inside the whole chamber. It is observed in our experiment that the bubbles can be generated to form as a single bubble, or as a group of bubbles in a cloud moving upstream, depending on the applied voltage and the degree of the fluid degassing. A single bubble tends to occur at low voltage (e.g. 120 V) in heavily degassed water, especially at the immediate beginning when the actuation is switched on.

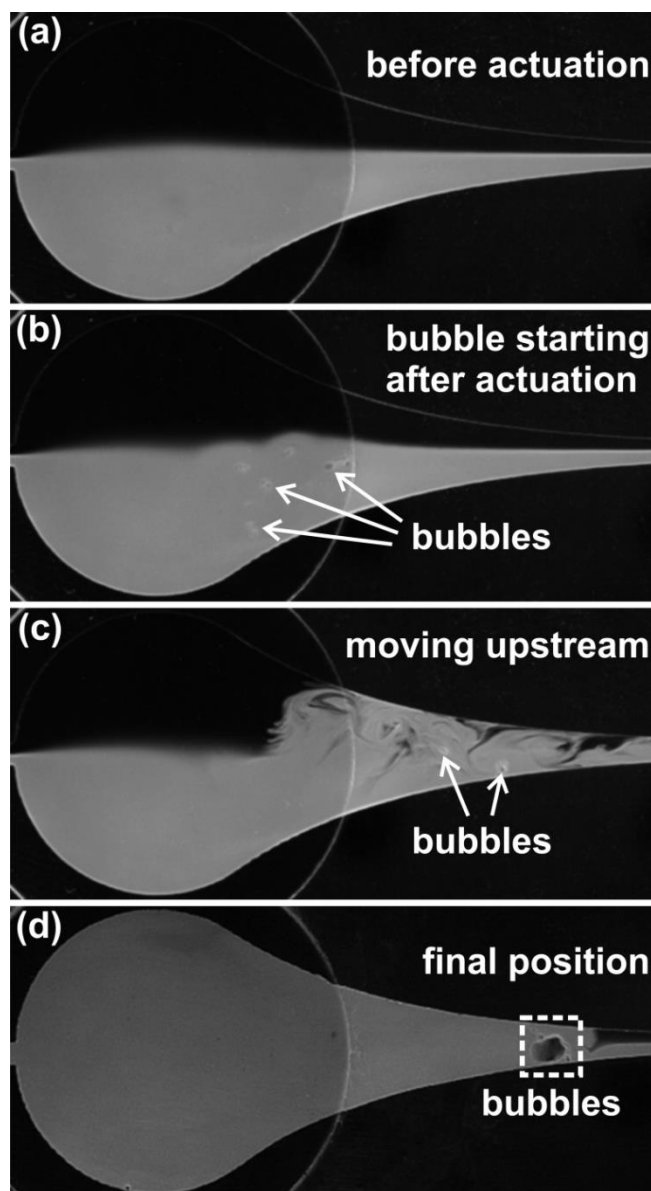


Fig. 5.3 Visualization of the bubbles generated in the chamber with the actuation at frequency 1.0 kHz and voltage 150 V. (a) Recorded image before actuation: the flow is laminar throughout the microfluidic chamber. (b) Recorded image when the actuation is switched on: the bubbles are generated. (c) Recorded image showing that the bubbles are traveling upstream against the main stream. (d) Recorded image when the bubbles arrive at some position close to the straight channel. The flowrate is 10 mL/h in total and the flow direction is from right to left.

5.3.2 Motions of bubbles in the nozzle

The motions of a group of bubbles moving through zone 2 are recorded by the camera at 12,000 fps, namely 12 images captured in per cycle based on the actuation frequency of 1 kHz. The time interval between two consecutive images is one sixth of one period in Figs. 5.4 and 5.5.

It shows that under strong actuations, the bubbles undergo a cycle of explosive growth and violent collapse, and during each period of oscillation the volumes of bubbles are varied by several orders of magnitude: in Fig. 5.4(a), the diameter of the largest bubble is 0.45 mm while in Fig. 5.4(c-e), the bubbles are fragmented or even dissolved by the compression of the actuation. It can also be found that, the bubbles undergo extensive coalescence and breakup under the action of actuations. Such a response with the fragmentation or dissolution of bubbles during the collapse phase is termed as “transient cavitation”, which is distinguished from the “stable cavitation”. After the diameter of the generated bubbles exceeds the height of the channel, the bubbles will lose their spherical shape and possess flat surfaces lubricated by thin liquid films near the top and bottom channel walls.

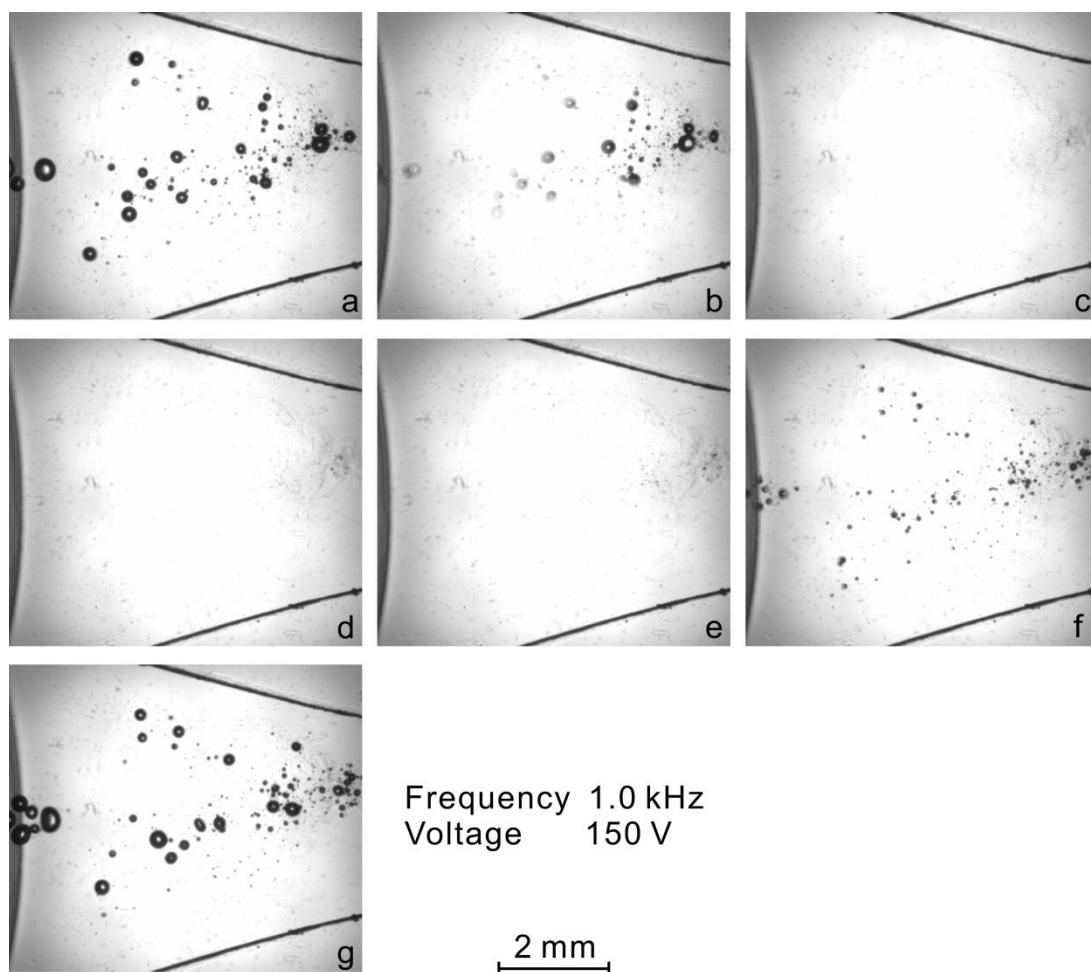


Fig. 5.4 Photographic series of the dynamics of bubbles in one cycle after being generated. The time interval between two successive images is $1/6 T$, or 0.167 ms. The actuation voltage and frequency are 150 V and 1 kHz, respectively.

The images of the bubbles at the same phase of different cycles are displayed in Fig. 5.5. The time interval between two consecutive images is one period, that is, 0.001 second. At high frequencies, especially in standing waves, bubbles can self-organize into a variety of structures such as streamers, clusters or bubble layers, and evolve on a timescale much larger than the acoustic period. However, in the present study, the bubble clouds are distributed randomly in space without certain structures due to the low frequency. For the case of 1 kHz actuation in water, the actuated pressure is almost uniformly distributed in the microfluidic channels, and no acoustic standing waves or travelling waves exist in the microfluidic chamber and thus, the bubbles cannot be organized in a certain pattern under the actuation.

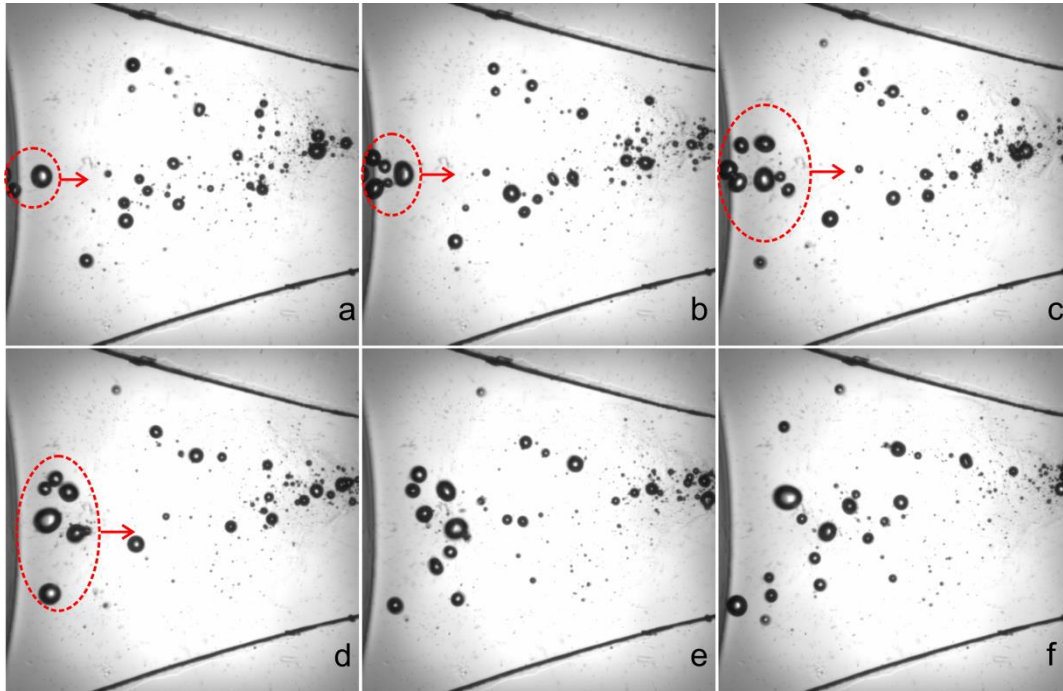


Fig. 5.5 Images of moving bubbles captured at the same phase of different cycles. The time between two successive images shown in the figure is one period, that is, 0.001 second. The actuation voltage and frequency are 150 V and 1 kHz, respectively.

5.3.3 Bubble coalescence and breakup

It is known that at low frequencies, the primary Bjerknes force which results from the radiation of the oscillatory pressure field is very weak while the secondary Bjerknes force which is the mutual interaction between oscillating bubbles is dominant at a short distance. The secondary Bjerknes force can cause the attraction or repulsion of bubbles depending on the phase

difference of two bubbles. Therefore, for the bubbles subjected to an oscillatory pressure field, the coalescence is further complicated due to the secondary Bjerknes force.

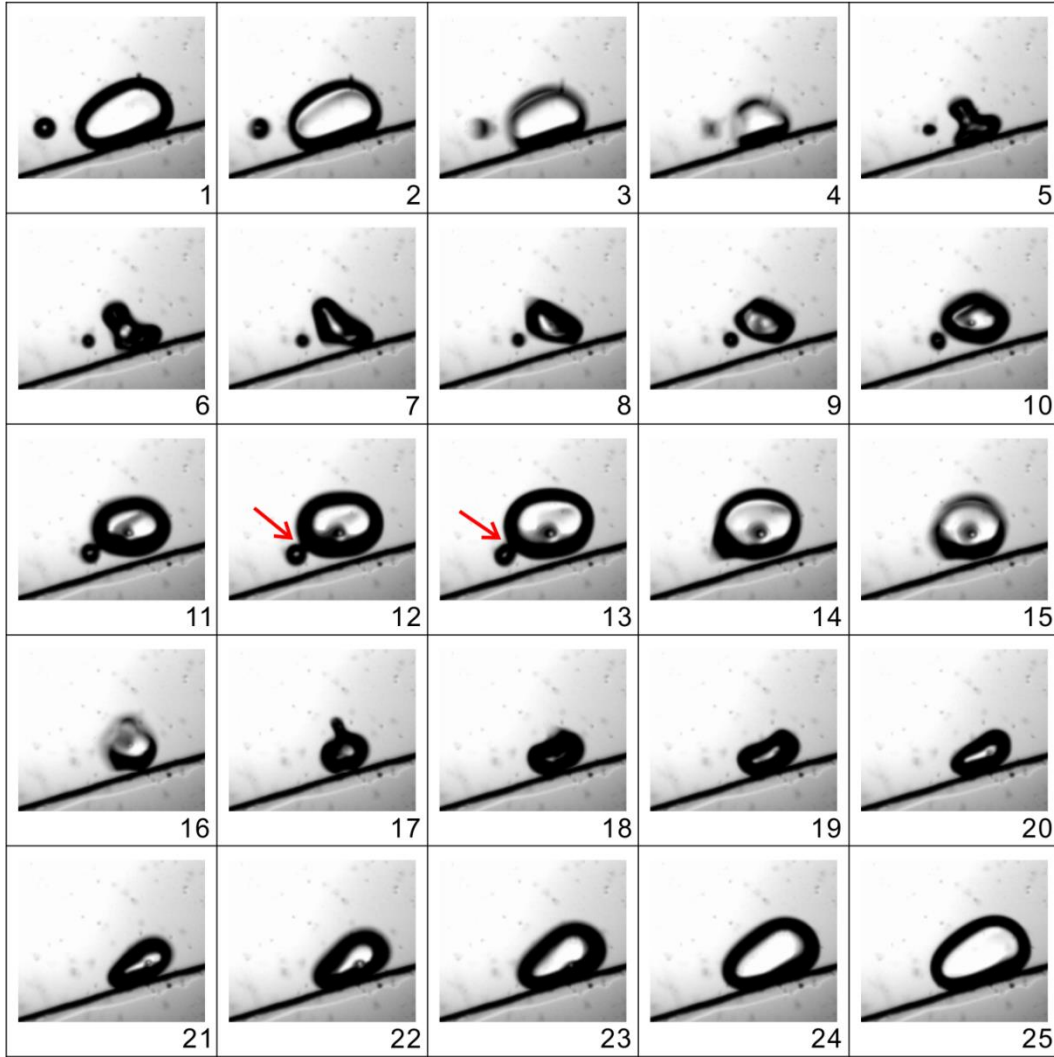


Fig. 5.6 Coalescence of two oscillating bubbles. One small bubble is attracted by a large one and then the two bubbles merge together to form a single one. The time between two successive images is $1/12 T$, or 0.083 ms. The actuation voltage and frequency are 150 V and 1 kHz, respectively.

The phenomena of bubble coalescence were photographed involving two bubbles and the process was exemplified in Fig. 5.6. It is seen that, during the compression phase a small bubble approaches a large one quickly under the action of the secondary Bjerknes force, and subsequently at expansion phase the two bubbles grow in size simultaneously until collide with each other. When the surfaces of the two bubbles touch with each other, a saddle-shaped “bridge” is built at first and the large bubble immediately “swallow” the small one with the

volume growth. After the surface area of the resultant cusp decreases, the process of bubble coalescence is finished. Finally, the consequent bubble contracts and expands with the periodic actuations. The whole process of bubble coalescence happens during an extremely short time, which is about one third of a period (0.33 ms).

The bubble model such as the Rayleigh-Plesset equation which is commonly used is based on the assumption that the oscillating bubble maintains spherical. However, when a bubble is collapsing strongly, the interface between the dense liquid and less dense gas is violently accelerated in the inward direction and thus, the bubble's shape is distorted due to the Rayleigh-Taylor instability. Under strong actuations, the shape instability of an oscillating bubble can even become so strong that breakup of the bubble takes place.

An example of the bubble breakup is demonstrated in Fig. 5.7. Contrary to the process of coalescence, as the bubble is collapsing rapidly, a cusp may be expelled from the base and then the "neck" connecting the two parts of the bubble is thinning quickly. When the interfacial tension is no longer able to maintain the bubble intact, a small bubble is shedded from the main one. The whole process of bubble breakup is even faster than the coalescence, and takes only one fourth of one period or 0.25 ms. Two mechanisms for the bubble breakup in fluids are reported, the inertial mechanism leading to sudden breakup by shear stress overcoming the surface tension and the resonance mechanism when the exciting frequency matches the natural frequency. Here, the natural frequency of the bubbles is higher than 10 kHz and the actuation frequency is far below the bubble's natural frequency and thus, the bubble breakup is caused by the large shear stress caused by the large velocity gradients.

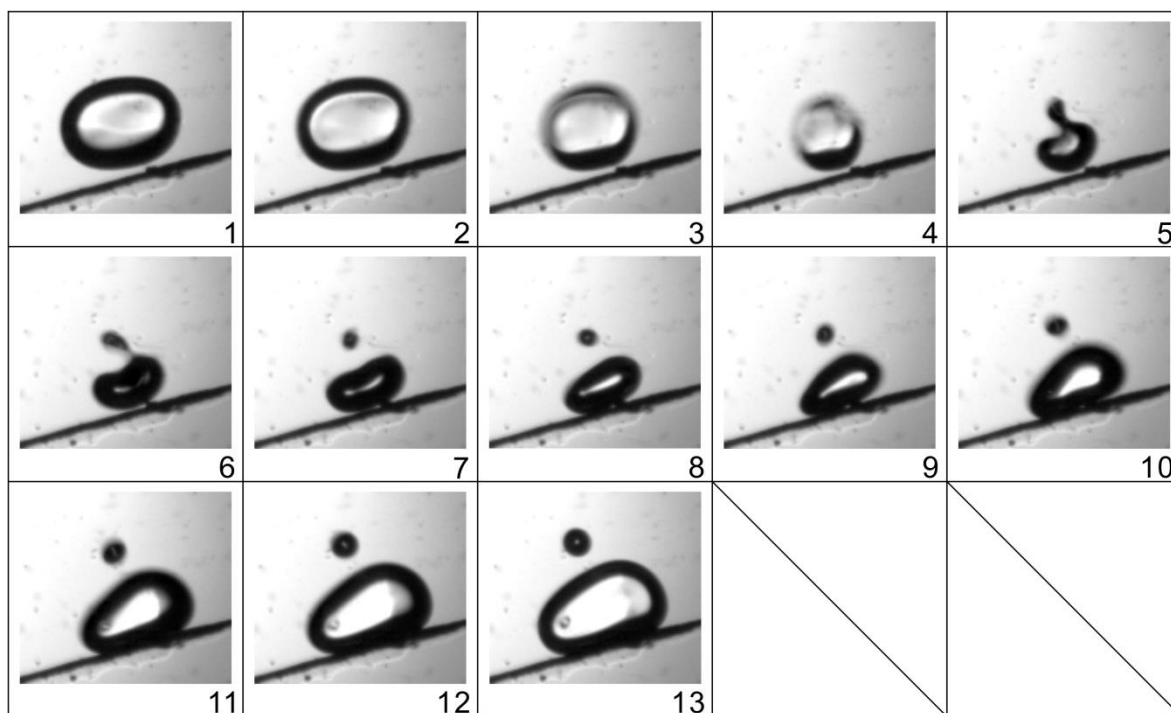


Fig. 5.7 Breakup of one oscillating bubble at the phase of the violent collapse. The time between two successive images is $1/12 T$, or 0.083 ms. The actuation voltage and frequency are 150 V and 1 kHz, respectively.

In fact, when the bubbles are translating forward, coalescences and breakups of bubbles happen frequently. Figure 5.8 shows an example of two bubbles undergoing a series of breakup and coalescence in very short time (three cycles). At first, one bubble breaks up into two smaller ones when it is collapsing and immediately the two resultant bubbles merge together into a large bubble, and in the collapse phase of the next cycle, the large bubble ruptures into several satellite ones. As such, after alternate breakup and coalescence for several times, the bubble clouds merge into a single bubble. The whole process of successive breakup and coalescence of the bubbles causes vigorous motions of the surrounding liquid, which has a major contribution to the mixing enhancement of the fluids.

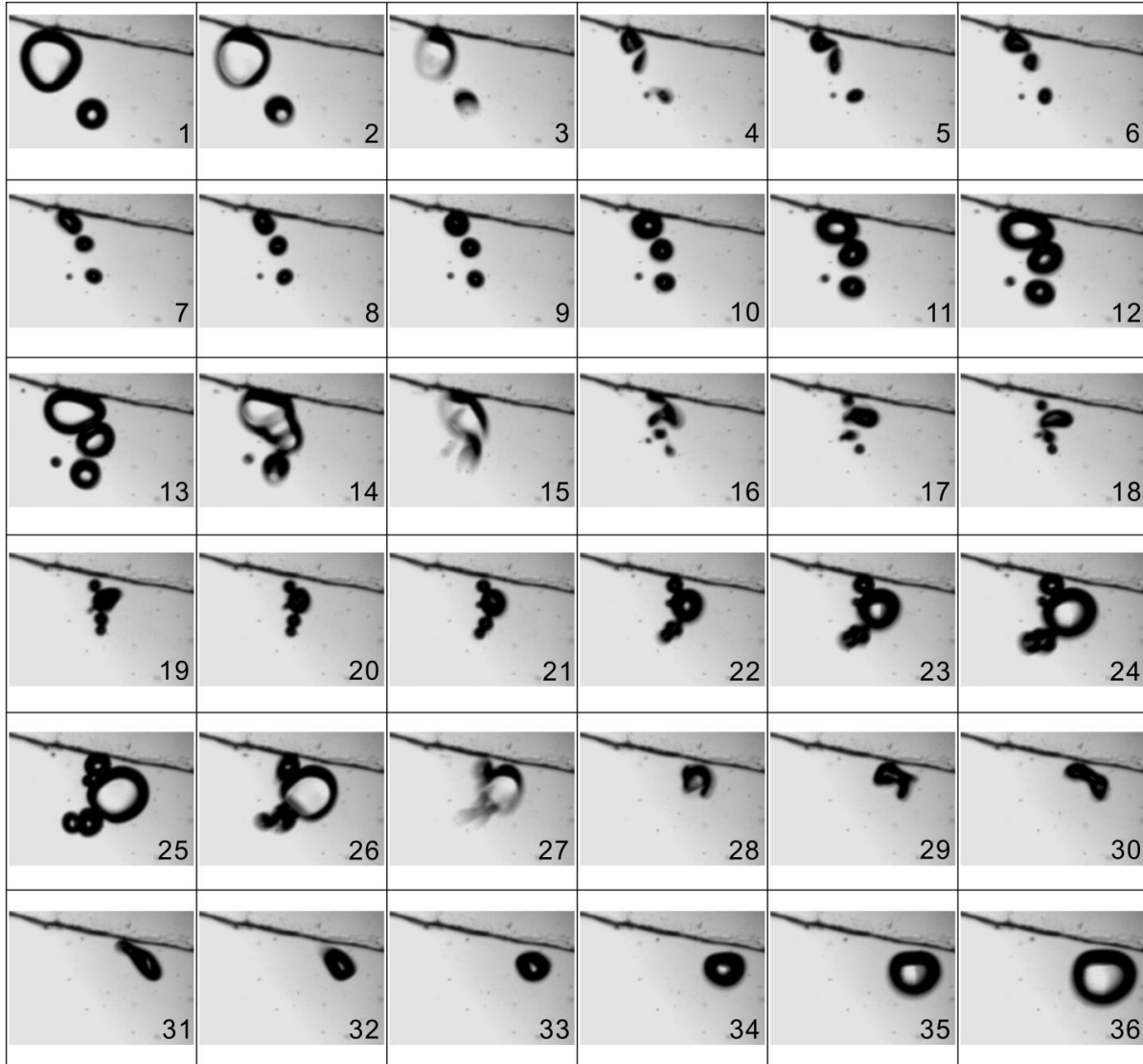


Fig. 5.8 A series of coalescence and breakup of the oscillating bubbles in the process of translation. The time between two successive images is $1/12 T$, or 0.083 ms. The actuation voltage and frequency are 150 V and 1 kHz, respectively.

5.3.4 Bubble-wall interactions

Oscillating bubbles near boundaries may not maintain spherical due to the loss of symmetry. It is reported that a nearby solid wall causes the collapsing bubbles to develop a high-speed liquid jet towards the solid surface, together with the formation of splash, vortex ring and even a sequence of shock waves [105].

Figures 5.9 and 5.10 give the example of an oscillating bubble in the proximity of the upper boundary and lower boundary, respectively. To avoid the breakup of the bubble in the process of

oscillation, we apply the actuation of lower voltage, 120 V. We can observe that due to the boundary effect, the bubble in each case cannot maintain perfectly spherical but become oblate or ellipsoidal. With the rapid contraction of the bubble, a liquid jet impacts towards the boundary in the 3rd and 4th frame of each case, which causes the bubble surface to sink from one side to the boundary. The bubble is further squeezed until it reaches the minimum volume in the 7th frame. Subsequently the bubble expands and goes into the next cycle. It is also noticeable that when the bubble is contracting quickly, the direction of the liquid jet is not perpendicular to the boundary wall, but partially directs against the main stream, which leads to the bubble's translation upstream in the nozzle.

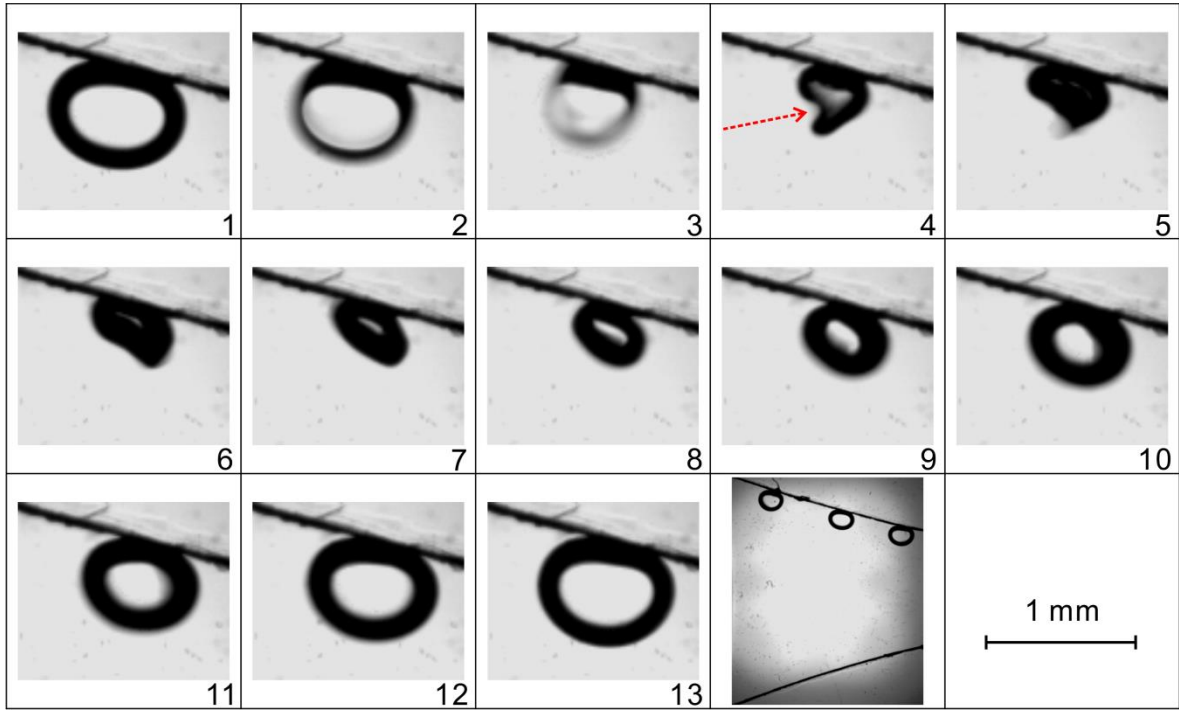


Fig. 5.9 The dynamics of an oscillating bubble nearby the upper boundary (1-13) and the trajectory of the bubble by stacking three images of the bubble corresponding to the same phase in a cycle. The time between two successive images is $1/12 T$, or 0.083 ms. The actuation voltage and frequency are 120 V and 1 kHz, respectively.

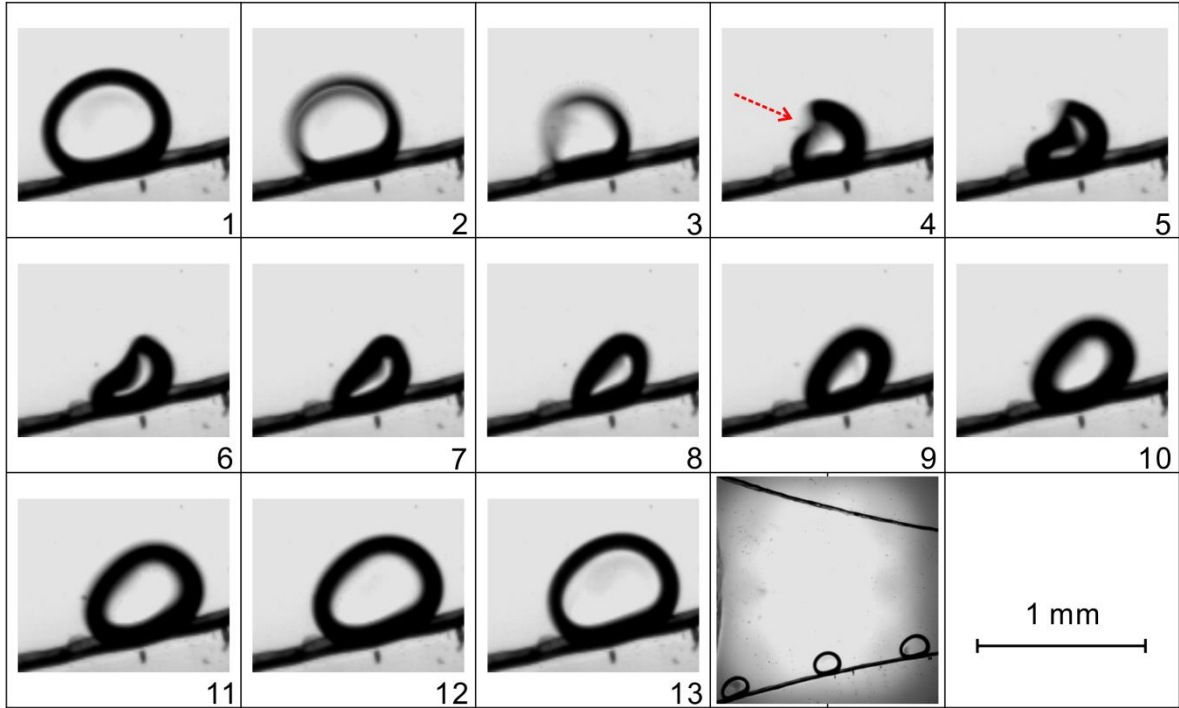


Fig. 5.10 The dynamics of an oscillating bubble nearby the bottom boundary (1-13) and the trajectory of the bubble by stacking three images of the bubble corresponding to the same phase in a cycle. The time between two successive images is $1/12 T$, or 0.083 ms. The actuation voltage and frequency are 120 V and 1 kHz, respectively.

Strasberg reported that when a bubble is close to a rigid boundary, its natural frequency shifts toward the lower frequency region [106]. Therefore, another effect of the boundary walls, including the top and bottom PMMA plates, is to make the nearby pulsating bubbles have lower resonance frequencies compared to free bubbles in infinite liquid. In addition, the parallel top and bottom walls can introduce additional drag force onto the bubble translation [107]. However, the confinement of the two parallel and symmetric walls does not fundamentally change the characteristics of the bubble dynamics in the x-y plane, such as the translation direction [108].

5.4 Numerical simulation

In order to explore the mechanism of bubble generation and oscillation in the microfluidic chamber under low frequency actuation, a three dimensional numerical simulation has been conducted by using the commercial software Ansys Fluent, focusing on pressure distribution and variation in the chamber.

5.4.1 Governing equations and boundary conditions

The bubbles generated inside the chamber are associated with the cavitation of the DI water under the low-frequency actuations. Thus, the pressure variation and distribution are key issues to understand the mechanisms of bubble generation in the microfluidic chamber. Due to small dimensions of the microfluidic chamber, it is difficult to measure the pressure experimentally. Here, numerical simulations using Ansys Fluent are performed to study the pressure variation and distribution in the chamber. The configuration and dimension of the chamber for the numerical simulation are identical to the experimental device. The computation domain and meshing scheme are shown in Fig. 5.11. There are 25 layers of meshes along the channel height direction and the meshes inside the chamber and at the Y junction are specifically refined.

Under the assumptions of incompressible, Newtonian fluid, the governing equations of continuity and momentum are expressed as,

$$\nabla \cdot \vec{V} = 0, \quad (5.1)$$

$$\frac{\partial \vec{V}}{\partial t} + \vec{V} \cdot \nabla \vec{V} = -\frac{\nabla p}{\rho} + \nu \nabla^2 \vec{V}. \quad (5.2)$$

where \vec{V} is the velocity vector, p the pressure, ρ the density and ν the kinetic viscosity.

In accordance with the experiments, the top wall is stationary and the bottom wall with PZT disk is set as a moving boundary of the PZT disk. The vibration of the PZT disk is described by the displacement $\zeta(x, y, t)$

$$\zeta(x, y, t) = \begin{cases} A_0 \sin(2\pi ft) \left(1 - \left(\frac{\sqrt{x^2 + y^2}}{R_{\text{chamb}}} \right)^2 \right)^2, & \text{within disk} \\ 0, & \text{outside disk} \end{cases}. \quad (5.3)$$

where the amplitude of vibration A_0 is 0.5 μm , the frequency imposed to the PZT disk f is 1.0 kHz, and R_{chamb} is radius of the chamber, which is 8 mm in our experiment.

The boundary condition for the inlet and outlet is set as velocity inlet and pressure outlet, respectively. All the boundary conditions are listed in Table 5.1. Based on a meshing independence study, it is found that the meshing scheme with 877300 cells in total is sufficient for our simulations.

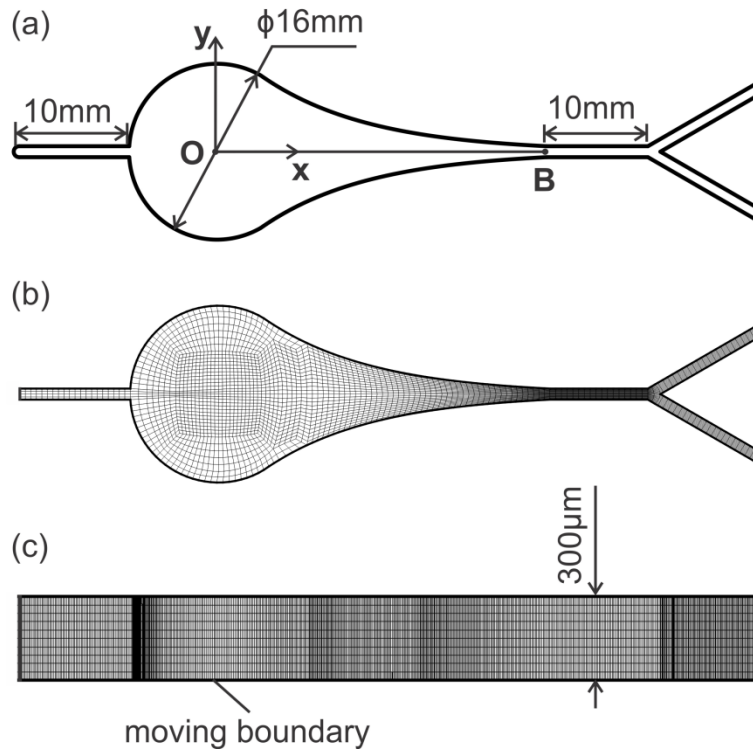


Fig. 5.11 (a) Geometry and dimension of the numerical simulation domain. (b) Meshing scheme in x-y plane (not to scale). (c) Meshing scheme in the height direction (not to scale).

Table 5.1 Boundary conditions used in the numerical simulation.

Component	Boundary condition	Description
Inlet	Velocity inlet	0.00926 m/s
Outlet	Pressure outlet	Reference pressure: 101325 Pa
Fluid		DI water Density $\rho=998.2 \text{ kg/m}^3$ Dynamic viscosity $\mu= 0.001003 \text{ Pa}\cdot\text{s}$
Wall (Bottom)	Moving	
Wall (Others)	Stationary	

The governing equations Eqs. (5.1) and (5.2) are solved by the finite volume method (FVM) in ANSYS FLUENT and the motion of the moving boundary described by Eq. (5.3) is fulfilled by the user-defined-function (UDF). The following solution methods and numerical schemes were used in the calculations: PRESTO! for pressure discretion and second order upwind for

momentum discretion; PISO scheme for pressure-velocity coupling; and the first order implicit time-dependent solution for unsteady formulations.

5.4.2 Bubble generation by low pressure

The simulation results are plotted in Fig. 5.12 which shows the pressure distributions with and without the actuation. It can be seen that without actuations (Fig. 5.12(a)), the DI water flows through the fluidic chamber from the right to left with a constant flowrate (10 mL/h). The pressure exhibits monotonic decrease from the inlet to outlet, and finally is equal to ambient pressure (101325 Pa) at the outlet, and the pressure drop is slight in the chamber. When the actuation is switched on, the pressure in the chamber fluctuates periodically following the actuation. The minimum pressure, which is our interest, in the chamber occurs at 0.75 T ($T = 1/f = 0.001\text{s}$) of each period. A typical pressure distribution at 0.75 T is presented in Fig. 5.12(b). It is found that, instead of decreasing monotonously, a low-pressure zone takes place in the region of the chamber where we observed the bubble generation in the experiments. The minimum pressure is as low as 469 Pa, which is very critical to the bubble generation.

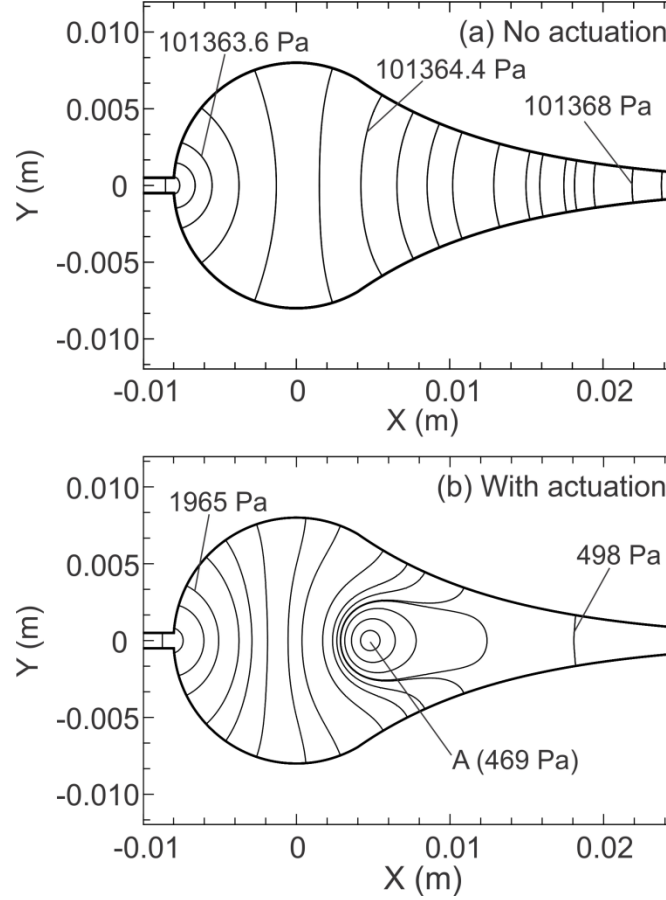


Fig. 5.12 The pressure distributions inside the chamber by numerical simulation. (a) Pressure distribution without actuation. (b) Pressure distribution under an actuation of frequency $f=1.0$ kHz at 0.75 T ($T = 1/f = 0.001$ s). The pressure at Point A is 469 Pa.

It is known that nuclei or microbubbles can exist inevitably in real liquids, even in pre-degassed water, and they act as the starting points for cavitation [109]. In a pressure field with the amplitude of P_a , the pressure on the bubble is $P_0 + P_a \sin(\omega t)$. A microbubble will undergo very weak oscillation and tiny volume pulsation unless the amplitude of the applied pressure fluctuation, P_a , is above a threshold, which is so-called Blake threshold [59]

$$P_a^B = P_0 - P_v + P_0 \left(\frac{4}{27} \frac{\alpha_S^3}{1 + \alpha_S} \right)^{\frac{1}{2}} \quad (5.4)$$

where, $\alpha_S = 2\sigma/(P_0 R_0)$ is the Laplace tension of the bubble in ambient conditions, $P_0=101325$ Pa and $P_v=3169$ Pa are the ambient pressure and vapor pressure respectively, $\sigma = 0.072$ N/m is the surface tension and R_0 is the initial radius of the bubble. Once the amplitude of the pressure fluctuation is higher than the Blake threshold, the microbubbles under the actuations may expand to a multiple of the initial size and collapse strongly afterwards, undergoing a violent volume

variation — the bubbles are observed to be “generated” in the liquid. The microbubbles in liquid have the characteristic sizes ranging from several microns to tens of microns [109]. By taking a typical microbubble of 10 μm in radius ($R_0=10\ \mu\text{m}$), the Blake threshold P_a^B can be calculated to be 100111 Pa, corresponding to the threshold pressure on the bubble $P_L = P_0 - P_a^B$, equal to 1214 Pa. The minimum pressure (469 Pa) from the simulation in the low-pressure zone is significantly below this threshold pressure, and the nuclei of the radius larger than 10 μm can be observed to be generated in the microfluidic chamber in our experiments.

It is noted that the gas dissolved in a liquid tends to accumulate in oscillating microbubbles over long periods, and this process of mass exchange from liquid to the bubbles is so-called “rectified diffusion” or RD effect [51]. When the actuation is applied, even the nuclei less than 10 μm can grow up in size continuously over many periods due to the rectified diffusion and once the microbubbles are large enough, they will become active, undergoing explosive growth and violent collapse.

5.4.3 Volume pulsation by pressure fluctuation

The pressure fluctuation over one period at the point P of zone 2 is plotted in Fig. 5.13. It shows that the pressure fluctuates periodically with its amplitude about 1 bar following a sinusoidal curve. Under this large amplitude pressure fluctuation, the bubble is expanded corresponding to the minimum pressure, while the bubble is squeezed to a collapse phase at the maximum pressure. These can be seen by the inset bubble photos in Fig. 5.13. It should be pointed out that the simulation results are obtained under the conditions of single phase and incompressible fluid. Once the bubbles are generated in the fluid, these conditions are not applicable and the pressure fluctuation amplitude can be different. However, as the bubble photos amply show, the actuated pressure fluctuations in the fluid with bubbles are strong enough to induce a large volume oscillation for the bubbles. This part will be further quantitatively studied in next chapter, together with the bubble translation.

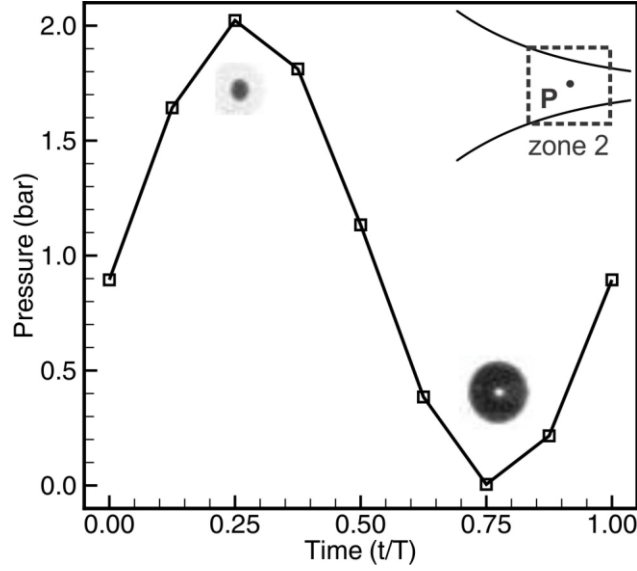


Fig. 5.13 Pressure fluctuation in one cycle at point P (0.013, 0, -0.00015) in zone 2. $T = 1/f = 0.001$ s.

5.5 Summary

In this chapter the dynamics of multiple bubbles in a microfluidic chamber under low-frequency actuation has been investigated both experimentally and numerically. The bubble generation is visualized by tracing fluorescent dyes, and the motions, coalescence and breakup of bubbles are recorded by a high-speed camera. The mechanisms of the bubble dynamics, including generation and oscillation, are studied by numerical simulation.

Our experiments show that under the actuation of 1 kHz, the bubbles are observed, starting near the center of the chamber, growing up in size and even moving upstream against the main flow. Such type of bubble generation is novel and different from those conventional bubble generations in acoustic fields, which are normally at high frequencies (> 20 kHz). The generated bubbles become irregular in shape due to the confinement of channel walls, other nearby bubbles and the curved nozzle walls. When bubbles are close enough under the action of the secondary Bjerknes force, the phenomena of bubble coalescence may take place. When a bubble is collapsing strongly, the shape instability of an oscillating bubble can even become so strong as to lead to breakup of the bubble. When the bubbles are translating forward, coalescences and breakups of bubbles happen frequently and cause vigorous motions of the surrounding liquid, which has a major effect on mixing enhancement. The simulation results show that there is a low-pressure zone in the chamber in each actuation cycle which corresponds to the area of

bubble generation in the experiment. The minimum pressure in this zone is related to a high-pressure fluctuation above the Blake threshold and the violent expansion and collapse of the pre-existing nuclei, which leads to the bubble generation in the experiment. The pressure fluctuation follows the actuation sinusoidally and maintains constant at 1 bar, resulting in considerably periodic volume pulsation of the bubble.

Chapter 6 Dynamics of a single bubble in a Microfluidic Chamber

6.1 Introduction

In the last chapter, we have investigated the generation, motions, coalescence and breakup of multiple bubbles in a microfluidic chamber with low-frequency actuations. The mechanism of bubble generation and oscillation is investigated by numerical simulation using Ansys Fluent. The bubble generation is attributed to the cavitation of nuclei in the liquid and the bubble oscillation to the pressure fluctuation in the chamber. In the experiments, we observed that bubbles translate upstream against the main flow after being generated, and this phenomenon has yet been clarified. At high frequencies, the primary Bjerknes force is the driving force of the bubble translation. However, at the low-frequency actuations, the wavelength of actuation pressure will be long compared to the bubble size and microfluidic channel, and hence the pressure gradient is very small around the bubbles, leading to a weak primary Bjerknes force. Therefore, other mechanisms, such as the wall effect, tend to be the dominant factor to propel the bubble forward under the low-frequency actuations in a microfluidic chamber.

The bubble dynamics in the vicinity of a plane wall was widely investigated by experiments and numerical simulations. However, in a microfluidic system, the bubbles are usually enclosed by multiple walls, and the wall effect will be much more complicated than the case of a single wall. Therefore, the dynamics of a single bubble in the neighborhood of multiple walls, such as two intersected walls, will be further investigated.

In this chapter, the dynamics of a single bubble, especially the translation and its relation with the oscillation, is investigated experimentally and analytically. An analytical model, taking into account of the multiple wall effect, is proposed to derive the governing equations of bubble oscillation and translation under the actuations. The analytical results are compared with the experimental observations. The mechanism of bubble translation is explored by studying the interaction force between the real bubble and the image bubbles induced by the boundary wall.

6.2 Experimental results and discussion

It is observed that the bubbles can be generated to form as a single bubble, or as a group of bubbles in a cloud, depending on the applied voltage and the degree of the fluid degassing. For the simplicity of quantitative analysis, the motion of a single bubble is investigated in this chapter. The single bubble tends to occur under low voltage in heavily degassed water, especially at the immediate beginning when the actuation is switched on. The experimental setup is the same as that used in Chapter 5 as illustrated in Fig. 6.1. The motion of a single bubble moving through zone 2 (indicated in Fig. 6.1) is recorded by a high-speed camera. In the experiments, the actuation frequency is set as 1 kHz and the total flowrate is 10 mL/h, respectively. The transient radius and displacement of the bubble are measured by processing recorded images in the software MATLAB. In the experiments, the bubble volume undergoes a great change within one actuation cycle and after the actuation is switched off, the bubble's radius is measured as its equilibrium radius.

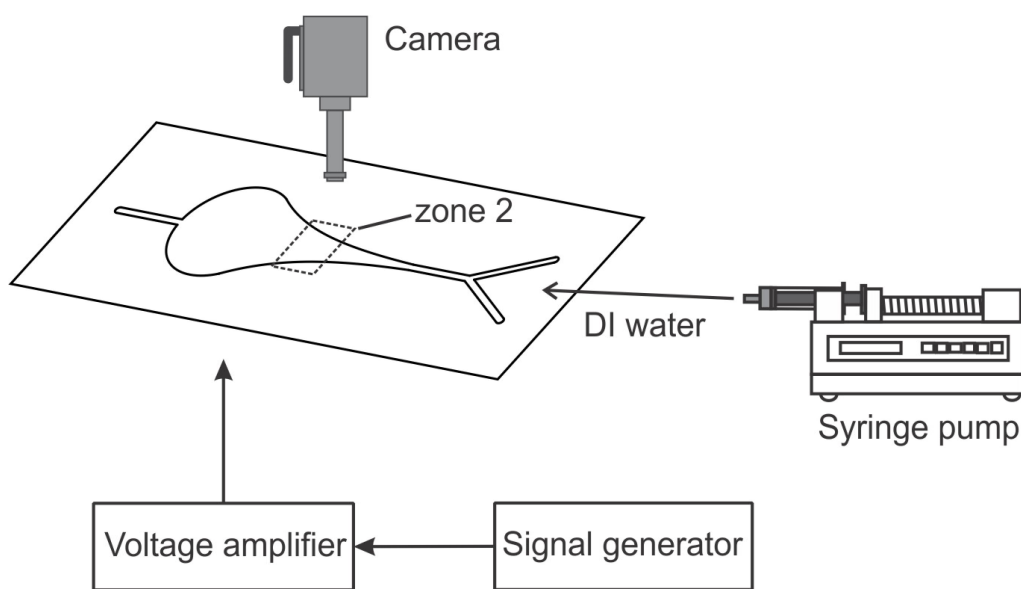


Fig. 6.1 Schematic illustration of the experimental setup. The motion of a single bubble moving through zone 2 is recorded by a high-speed camera and then analyzed in MATLAB.

6.2.1. Bubble trajectory of translation

An individual bubble moving through the region zone 2 is recorded by the camera set at 12,000 fps, namely 12 images captured in one cycle based on the actuation frequency of 1 kHz. The images of the oscillating bubble of the radius = 0.075 mm at the same phase of each cycle are stacked into a particular figure (via the software *ImageJ*), and the resultant figure is shown in Fig. 6.2. The time interval between two selected images is two periods, that is, 0.002 second. It shows that a single bubble moves forward along a straight line, which makes it an excellent case for quantitative analysis. The bubble translates against the direction of the main stream, which is agreeable with the phenomenon for multiple bubbles.

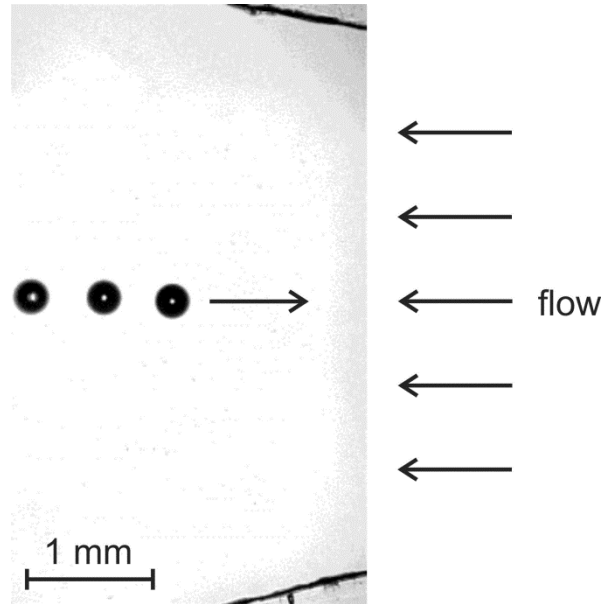


Fig. 6.2 Movement of a single bubble towards upstream along a straight line after being generated in the chamber. The trajectory is obtained by stacking four images of the bubble corresponding to the same phase in a cycle and the time between two successive images is two periods, that is, 0.002 seconds.

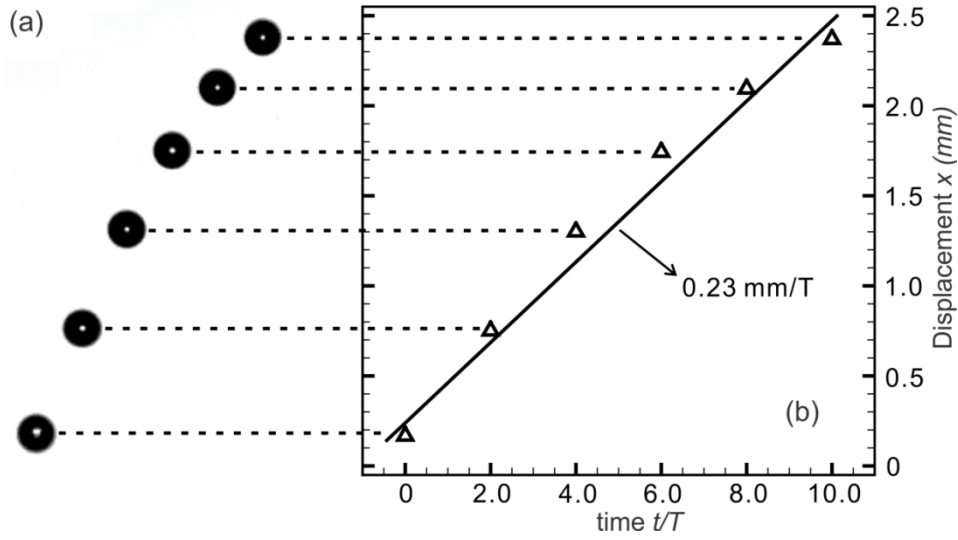


Fig. 6.3 (a) Images of a moving single bubble captured at the same phase in different cycles. (b) The displacement of the bubble versus time normalized by the actuation period $T = 0.001$ s. The average translation velocity of the bubble is estimated to be 0.23 m/s, based on the slope of the displacement curve.

The images of the moving bubble at the same phase of different cycles are displayed in Fig. 6.3(a) and the displacement of the bubble center versus time is plotted in Fig. 6.3(b). The time interval between two successive images is two periods, that is, 0.002 seconds. It can be seen that the bubble displacement increases with time and the average bubble velocity is estimated to be 0.23 m/s based on the slope of the displacement curve. The present velocity of bubble translation is much greater than the mean flow velocity (about 0.0093 m/s) inside the chamber. Crum and Eller [7] reported that a bubble, which was actuated by a standing wave field in infinite liquid, moved spatially due to the primary Bjerknes force. At the frequencies ranging from 23.6 kHz to 28.3 kHz, the translation velocity reached its maximum, 0.023 m/s, which is much smaller than that in our experiment. In our study, the translation of the bubble is not attributed to the primary Bjerknes force but the effect of the two inclined boundary walls, which will be discussed in detail in Section 6.3.3.

6.2.2. Radial oscillation and its interaction with translation

The images of a bubble under actuation at different phases in two successive cycles are presented in Fig. 6.4. The time between two successive images is $1/12 T$, with $T = 0.001$ s being the actuation period. It is observed that the bubble oscillates periodically under the actuation,

indicating that the bubble undergoes remarkable volume variation, and a complete bubble pulsation cycle is found to consist of slow growth and fast collapse. The bubble maintains spherical during most time of the oscillation, except that during a short time when the bubble contracts to its minimum volume, the spherical shape changes into an ellipsoid.

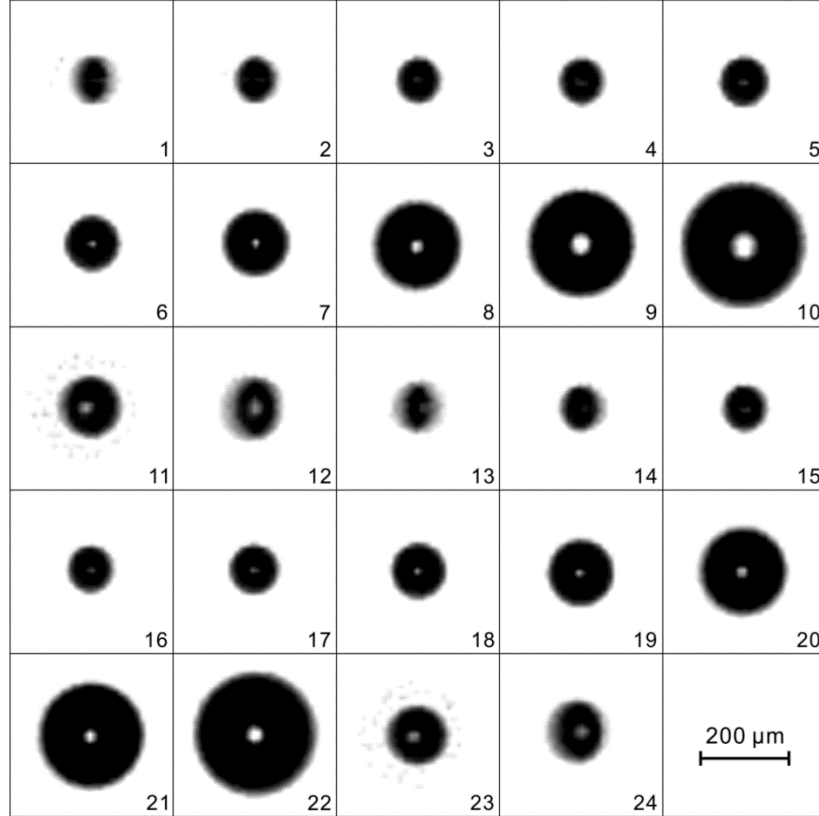


Fig. 6.4 Images of a bubble under the actuation of two successive cycles, showing remarkable volume oscillation. The time between two successive images is $1/12 T$ with $T = 0.001$ s being the actuation period.

Figure 6.5 shows the radius (Fig. 6.5(a)) and displacement (Fig. 6.5(b)) of the bubble in two successive cycles. From Fig. 6.5(a), it can be seen that the bubble radius does not follow the sinusoidal actuation with time, and there is a long expansion and steep collapse in each cycle, which indicates that the radial response of the bubble is a typical nonlinear process under strong actuation. The bubble radius varies from $R_{min} = 0.05$ mm to $R_{max} = 0.14$ mm during one cycle, corresponding to a ratio of $R_{max}/R_{min} = 2.8$ and the ratio of the maximum volume to the minimum volume about 22. Accompanied by periodical volume variation, the bubble translates in a “jerk” way as shown in Fig. 6.5(b). The bubble “jumps” forward during a short time interval of the collapse phase, and then moves backward slightly when growing up during expansion phase. In

the collapse phase (as illustrated between the two dot-dashed lines), the bubble moves faster, at the velocity of about 0.55 m/s, which is greater than the average bubble translation velocity 0.23m/s shown in Fig. 6.3(b). This observation is consistent with the numerical results by Reddy and Szeri [72] for bubbles driven at high frequencies that the bubble translation velocity was maximized when the bubble collapsed violently.

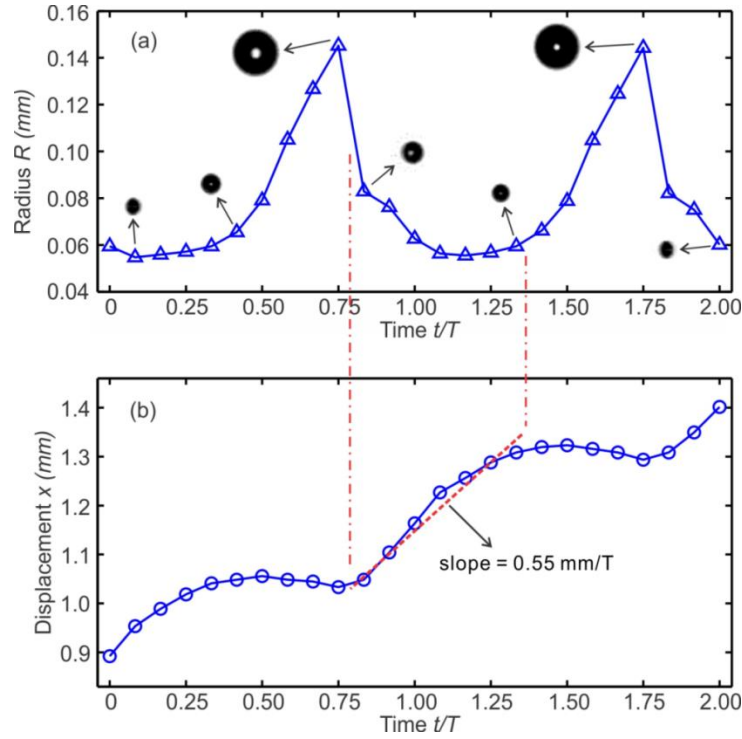


Fig. 6.5 (a) Variation of the bubble radius in two successive cycles. (b) Variation of the bubble displacement in two successive cycles. The bubble moves forward at the phase of collapse. $T = 0.001$ s, is the actuation period.

6.3 Analytical modelling

A simplified analytical model for a bubble nearby two intersected walls is proposed to analyze the bubble oscillation and translation under the actuations, especially to explore the mechanism of the bubble moving upstream against the main flow. To construct the model, we assume that the flow is potential, the fluid around the bubble is incompressible, and the bubble is small compared to the bubble-wall distance. The nozzle part of the chamber is further simplified into two intersected straight walls which extend to infinity.

6.3.1. Analytical modelling for bubble oscillation and translation

6.3.1.1 The simplified model and governing equations

Based on our experimental observations, the bubbles are confined within a narrow space (300 μm) between the top and bottom PMMA plates, and the bubble translates in the x-y plane. It is known that the bubble confined by two parallel boundaries will undergo additional drag force [107]. However, our model does not include the effect of the top and bottom surfaces for two reasons: the additional drag force does not fundamentally change the characteristics of the bubble dynamics in the x-y plane, such as the direction of the bubble translation; the additional drag force from confinements is estimated to be less than 10% on average [108]. Moreover, the nozzle profile of the chamber at zone 2 is ideally treated as two inclined straight walls and intersected at an angle of $2\alpha = 30^\circ$ on the right as illustrated in Fig. 6.6. Since the maximum main flow velocity is about 0.0093 m/s in the microfluidic chamber, which is much smaller than the observed bubble translation velocity, 0.23 m/s, the fluid is assumed to be stationary with zero main flow velocity. Thus, the original problem can be converted to a bubble moving in a still fluid between two intersected walls as shown in Fig. 6.6. The Lagrangian method used by Doinikov [8] is adopted to derive the governing equations for the bubble's radius R and displacement x in the present study. The method of images is introduced to satisfy the boundary conditions on the wall and the bubble surface and here, we take the first-order images for simplicity.

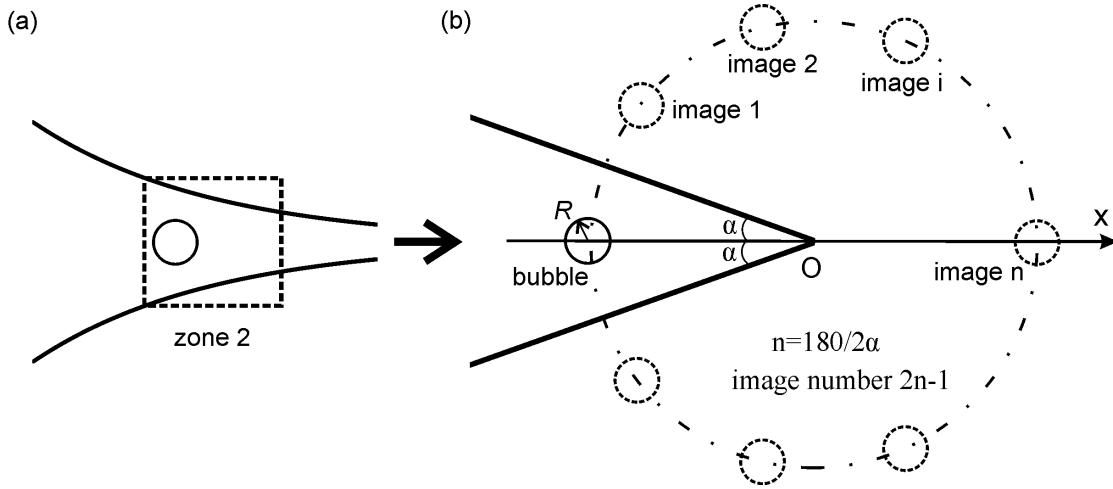


Fig. 6.6 Illustration of the analytical model. (a) In the experiment, the bubble is in zone 2 of the microfluidic chamber. (b) In the model, the bubble is located in a position on the bisector line of two inclined straight walls.

The velocity potential, Φ , which is defined as $\vec{V} = \nabla\Phi$ for the fluid velocity V in the flow field, satisfies the following governing equations and boundary conditions

$\nabla^2\Phi = 0$	in the flow field
$\nabla\Phi \rightarrow 0$	in the infinity of the flow field
$\frac{\partial\Phi}{\partial n} = -\dot{R} - \dot{x}\cos\theta$	on the bubble surface
$\frac{\partial\Phi}{\partial n} = 0$	on the sphere surface

where \bar{n} is the unit normal towards the flow field from the bubble or the boundary; R and x with dots are the corresponding time derivatives for the bubble's radius and displacement, respectively.

The velocity potential of the bubble nearby a boundary wall can be simulated by introducing a series of image bubbles to replace the boundary wall, and this is so-called the method of images. The model for a bubble between two intersected walls is illustrated in Fig. 6.7(a), together with the coordinate system. The image system which satisfies the boundary condition at the rigid walls is illustrated in Fig. 6.7(b). There are $2n-1$ image bubbles in total, where $n = 180/2\alpha$ (n is an integer). R and x denote the time-dependent radius and displacement respectively, the variables with dots corresponding to the time derivatives, and d_i is the distance between the real bubble and the i th image bubble. Local coordinates, (r, θ) and (r_i, θ_i) are located at the center of the real bubble and i th image bubbles, respectively.

The velocity potential in response to the actuation in the model is defined as

$$\Phi = \dot{R}\Phi^r + \dot{x}\Phi^x \quad (6.1)$$

where R and x with dots are the corresponding time derivatives for the bubble's radius and displacement, respectively, Φ^r is the unit potential for bubble radial motion and Φ^x is the unit potential for bubble translational motion.

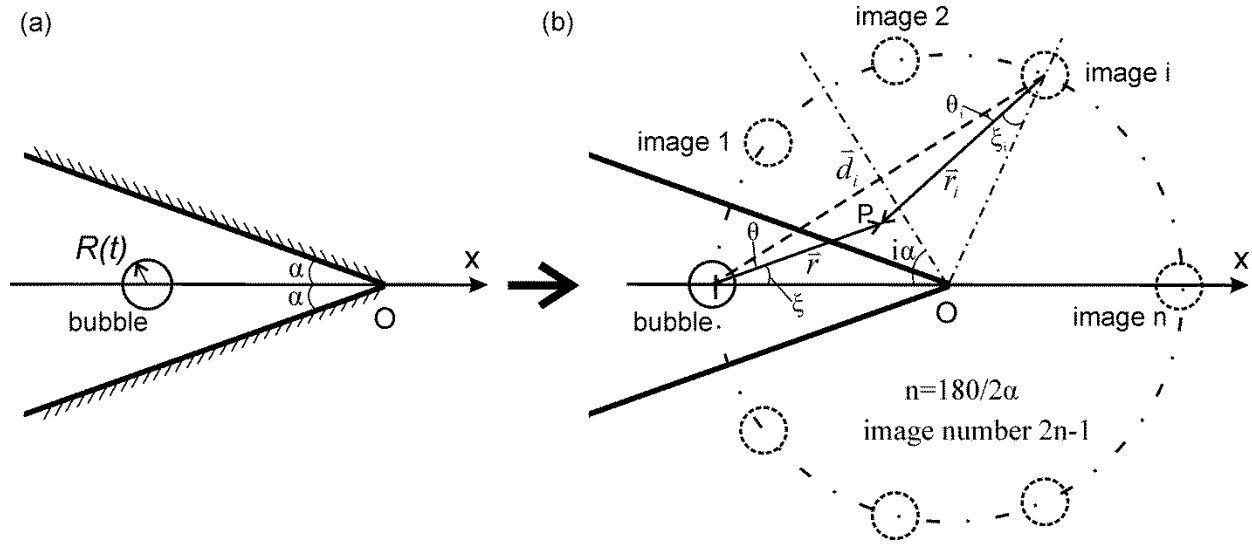


Fig. 6.7 The model and image system for a bubble located nearby two inclined walls.

The boundary conditions which satisfy the no-penetration or zero normal velocity at the surface of the bubble and walls are listed in Table 6.1.

Table 6.1 The boundary conditions at the bubble and wall surfaces.

	Bubble Surface	Wall Surface
Pulsation	$\frac{\partial \Phi^r}{\partial n} = -1$	$\frac{\partial \Phi^r}{\partial n} = 0$
Translation	$\frac{\partial \Phi^x}{\partial n} = -\cos \theta$	$\frac{\partial \Phi^x}{\partial n} = 0$

6.3.1.2 The kinetic energy

The kinetic energy T of the system is determined by the surrounding liquid

$$T = \frac{\rho}{2} \int_{\Omega} |\nabla \Phi|^2 dV \quad (6.2)$$

which can be expressed in terms of Gaussian Theorem by,

$$T = \frac{\rho}{2} \int_{\Omega} \nabla \Phi \cdot \nabla \Phi dV \quad (6.3)$$

The Green's first identity reads as,

$$\iiint_{\Omega} (\psi \nabla^2 \Phi + \nabla \Phi \cdot \nabla \psi) dV = - \oiint_{\Sigma} \psi (\nabla \Phi \cdot \vec{n}) dS \quad (6.4)$$

Here, the negative sign results from the inward normal of \vec{n} . Replacing ψ with Φ , we can immediately obtain,

$$\iiint_{\Omega} (\Phi \nabla^2 \Phi + \nabla \Phi \cdot \nabla \Phi) dV = - \oiint_{\Sigma} \Phi (\nabla \Phi \cdot \vec{n}) dS \quad (6.5)$$

For a potential flow satisfying $\nabla^2 \Phi = 0$, substituting Eq. (6.5) into Eq. (6.3), we can obtain the volume integrand of the kinetic energy,

$$T = - \frac{\rho}{2} \oiint_{\Sigma} \Phi \frac{\partial \Phi}{\partial n} dS \quad (6.6)$$

Then, the total kinetic energy is given by,

$$T = - \frac{\rho}{2} \oiint_{\Sigma} (\dot{R} \Phi^r + \dot{x} \Phi^x) \frac{\partial \Phi}{\partial n} dS = - \frac{\rho}{2} \oiint_b (\dot{R} \Phi^r + \dot{x} \Phi^x) (-\dot{R} - \dot{x} \cos \theta) dS \quad (6.7)$$

where the surface integral is taken over the real bubble surface.

Thus, the kinetic energy of the fluid, T , can be calculated based on the velocity potential Φ as [76]

$$T = \frac{\rho}{2} [\dot{R}^2 \iint_b \Phi^r dS + 2\dot{R}\dot{x} \iint_b \Phi^x dS + \dot{x}^2 \iint_b \Phi^x \cos \xi dS] \quad (6.8)$$

where ρ is the fluid density, ξ is a coordinate angle defined in Fig. 6.7, and in the calculation, the Green's second identity is used,

$$\oiint_b \Phi^r \frac{\partial \Phi^x}{\partial n} dS = \oiint_b \Phi^x \frac{\partial \Phi^r}{\partial n} dS \quad (6.9)$$

To calculate the kinetic energy T , in our model, the two inclined walls are replaced by $2n-1$ ($n = 180/2\alpha$) image bubbles to meet the boundary condition of zero normal velocity at the walls. This is illustrated in Fig. 6.7(b). Since $2\alpha = 30^\circ$ and $n = 6$ there are 11 image bubbles in our model.

The oscillation of the bubble is regarded as a point source with periodic strength and thus, the velocity potential from the bubble radial pulsation of unit strength is obtained by the superposition of contributions from all bubbles, including the real one and its images, i.e.

$$\Phi^r = \varphi^r + \sum_{i=1}^{2n-1} \varphi_i^r = -\frac{R^2}{r} + \sum_{i=1}^{2n-1} \left(-\frac{R^2}{r_i} \right) \quad (6.10)$$

where φ^r is the velocity potential corresponding to the real bubble, and φ_i^r is the velocity potential responding to the i th image bubble.

The translation of the bubble is analogous to a moving sphere in the liquid and the velocity potential from the bubble translation of unit strength is obtained by the superposition of contributions from all bubbles, including the real one and images, i.e.

$$\Phi^x = \varphi^x + \sum_{i=1}^{2n-1} \varphi_i^x = -\frac{R^3 \cos \xi}{2r^2} + \sum_{i=1}^{2n-1} \left(-\frac{R^3 \cos \xi_i}{2r_i^2} \right) \quad (6.11)$$

where φ^x is the velocity potential for the real bubble, and φ_i^x is the velocity potential for the i th image. ξ and ξ_i , are the coordinate angles denoted in Fig. (6.7b).

The first integral in Eq. (6.8) can be calculated by substituting the potential Eq. (6.10) into the integral and evaluating it over the real bubble surface. The integration, denoted as I_1 , gives

$$\oint \oint_b \Phi^r dS = 4\pi R^3 + \frac{4\pi R^4}{D_1} = I_1 \quad (6.12)$$

$$\text{where } \frac{1}{D_1} = \sum_{i=1}^{n-1} \frac{2}{d_i} + \frac{1}{d_n}.$$

By substituting the velocity potential Eq. (6.11) into the second and third integrals in Eq. (6.8), the two integrals, denoted as I_2 and I_3 , can then be obtained by evaluating integrals over the real bubble surface,

$$\oint \oint_b \Phi^x dS = -\frac{2\pi R^5}{D_2} = I_2 \quad (6.13)$$

$$\oint \oint_b \Phi^x \cos \xi dS = \frac{2}{3} \pi R^3 + \frac{2\pi R^6}{D_3} = I_3 \quad (6.14)$$

$$\text{where, in Eqs. (6.13) and (6.14), } \frac{1}{D_2} = \sum_{i=1}^{n-1} \frac{2 \sin i\alpha}{d_i^2} + \frac{1}{d_n^2} \text{ and } \frac{1}{D_3} = \sum_{i=1}^{n-1} \frac{\sin^2 i\alpha + 1}{d_i^3} + \frac{1}{d_n^3}.$$

The kinetic energy T can therefore be given as

$$T = \frac{\rho}{2} [\dot{R}^2 I_1 + 2\dot{R}\dot{x} I_2 + \dot{x}^2 I_3] \quad (6.15)$$

where I_1 , I_2 and I_3 denote the three integrals in Eq. (6.8). In the calculations, the velocity potentials contributed by the image bubble are solved by transforming the coordinates of the image bubble to the local coordinates of the real bubble and keeping the first two terms of the Legendre expansion.

6.3.1.3 The dissipation energy

The potential energy U of the system is caused by the variation of the gas volume,

$$U = -P_l V_b \quad (6.16)$$

where V_b is the time-dependent volume of the bubble and P_l is the pressure at the surface of the real bubble, $P_l = P_g - 2\sigma/R - P_\infty$, P_g the pressure of gas inside the bubble, σ the surface tension and P_∞ the pressure at infinity.

In the situation that the bubble is translating drastically or the bubble is pulsating violently, the viscous term is insignificant except in the boundary layer.

The liquid velocity can be represented by

$$\vec{V} = V_r \vec{e}_r + V_\theta \vec{e}_\theta \quad (6.17)$$

where the radial component V_r and tangential component V_θ are

$$V_r = \frac{R^2 \dot{R}}{r^2} + \frac{R^3 \dot{x} \cos \theta}{r^3} \quad (6.18)$$

$$V_\theta = \frac{R^3 \dot{x} \sin \theta}{2r^3} \quad (6.19)$$

The dissipation potential of the system is calculated by

$$F = \int_{\Omega} f d\Omega \quad (6.20)$$

where f is the density of the dissipation potential and Ω is the volume occupied by the liquid.

For the incompressible liquid, the dissipation potential density f can be calculated by [110]

$$f = \mu (V_{ij})^2 \quad (6.21)$$

where V_{ij} is the rate of strain tensor, written as

$$V_{ij} = \frac{1}{2} \left(\frac{\partial V_i}{\partial x_j} + \frac{\partial V_j}{\partial x_i} \right) \quad (6.22)$$

Therefore, substituting Eq. (6.22) into Eq. (6.21), one obtains

$$f = \mu(V_{rr}^2 + V_{\theta\theta}^2 + V_{\varphi\varphi}^2 + 2V_{r\theta}^2) = \frac{6R^4 \dot{R}^2}{r^6} + \frac{18R^5 \dot{R}\dot{x} \cos \theta}{r^7} + \frac{9R^6 \dot{x}^2}{2r^8} + \frac{9R^6 \dot{x}^2 \cos^2 \theta}{r^8} \quad (6.23)$$

Then, the dissipation potential F of the system can be integrated over the whole volume

$$F = 8\pi\mu R\dot{R}^2 + 6\pi\mu R\dot{x}^2 \quad (6.24)$$

Hence, the drag force of the bubble can be obtained as

$$F_{er} = -\frac{\partial F}{\partial \dot{R}} = -16\pi\mu R\dot{R} \quad (6.25)$$

for radial motion and

$$F_{ex} = -\frac{\partial F}{\partial \dot{x}} = -12\pi\mu R\dot{x} \quad (6.26)$$

for translational motion, which is exactly the Levich viscous drag exerted upon the bubble [111].

6.3.1.4 The Lagrangian equation

The Lagrangian L can be obtained by the kinetic energy T and potential energy U ,

$$L = T - U = \frac{\rho}{2}[\dot{R}^2 I_1 + 2\dot{R}\dot{x} I_2 + \dot{x}^2 I_3] + P_1 V_b \quad (6.27)$$

Substituting Eqs. (6.24) and (6.27) into the Lagrangian equation

$$\frac{d}{dt} \left(\frac{\partial L}{\partial \dot{q}_i} \right) - \frac{\partial L}{\partial q_i} = -\frac{\partial F}{\partial \dot{q}_i} \quad (6.28)$$

and carrying out the differentiations with respect to the generalized coordinates R and x , one can obtain the governing equations for the oscillation and translation of a bubble between two inclined walls,

$$\left(R + \frac{R^2}{D_1}\right)\ddot{R} + \left(\frac{3}{2} + \frac{2R}{D_1}\right)\dot{R}^2 - \frac{2R^2}{D_2}\dot{R}\dot{x} - \frac{R^3}{2D_2}\ddot{x} + \left(\frac{2R^3}{D_3'} - \frac{1}{4} - \frac{3R^3}{2D_3}\right)\dot{x}^2 = \frac{P_2}{\rho} \quad (6.29)$$

$$\left(\frac{R}{3} + \frac{R^4}{D_3}\right)\ddot{x} + \left(1 + \frac{6R^3}{D_3}\right)\dot{R}\dot{x} - \frac{3R^2}{D_2}\dot{R}^2 - \frac{R^3}{D_2}\ddot{R} = \frac{F_{ex}}{2\pi R^2 \rho} \quad (6.30)$$

where D_1 , D_2 , D_3 and D_3' are coefficients related to the bubble-wall distance and they are given as following

$$\frac{1}{D_1} = \sum_{i=1}^{n-1} \frac{2}{d_i} + \frac{1}{d_n}, \quad \frac{1}{D_2} = \sum_{i=1}^{n-1} \frac{2\sin i\alpha}{d_i^2} + \frac{1}{d_n^2}, \quad \frac{1}{D_3} = \sum_{i=1}^{n-1} \frac{\sin^2 i\alpha + 1}{d_i^3} + \frac{1}{d_n^3} \quad \text{and} \quad \frac{1}{D_3'} = \sum_{i=1}^{n-1} \frac{2\sin^2 i\alpha}{d_i^3} + \frac{1}{d_n^3}.$$

where, d_i is the distance between the real bubble and the i th image bubble. The coefficients D_1 , D_2 , D_3 and D_3' in Eqs. (6.29) and (6.30) contain terms with $\sum_{i=1}^{n-1}$ which denote the effect of the inclined walls. In a limiting case by setting $2\alpha = 180^\circ$ and $n = 1$, the two inclined walls will be reduced to a single flat wall and all the terms with $\sum_{i=1}^{n-1}$ in coefficients D_1 , D_2 , D_3 and D_3' will become zero. Then our derived equations Eqs. (6.29) and (6.30) will be exactly the same as the analytical results obtained by Cole [76].

In the calculations, the scattered pressure at the surface of the bubble P_2 is defined by $P_2 = P_1 - 4\mu_{\text{eff}}\dot{R}/R = P_g - 2\sigma/R - 4\mu_{\text{eff}}\dot{R}/R - P_\infty$, and μ_{eff} the effect viscosity. F_{ex} is the drag force for the bubble translation calculated by the dissipation potential of the system, $F_{\text{ex}} = -12\pi\mu R\dot{x}$. The gas bubble is polytropic so that the pressure of a bubble of radius R is $P_g = P_{g0}(R_0/R)^{3\kappa}$, where the gas pressure at equilibrium P_{g0} is calculated by $P_{g0} = P_0 + 2\sigma/R_0$, the bubble radius at equilibrium $R_0 = 0.075$ mm and κ is polytropic index, clearly, $\kappa = 1$ for isothermal process and $\kappa = \gamma$ (the ratio of the gas specific heat) for adiabatic behavior. The applied pressure at infinity is $P_\infty = P_0 - P_a \sin(2\pi ft)$, where P_0 is the ambient pressure, P_a the amplitude of applied pressure fluctuation, and f the actuation frequency. P_a is set as $0.93P_0$ which is obtained by means of numerical simulation in last chapter. The effective viscosity μ_{eff} consists of the thermal damping μ_t and fluid viscous damping μ [112]. All the parameters in the model are listed in Table 6.2.

Table 6.2 The parameters used in the analytical model.

Parameter	Symbol	Value
Liquid density	ρ (kg/m ³)	998.2
Surface tension	σ (N/m)	0.0728
Sound speed	c (m/s)	1484.7
Ambient pressure	P_0 (Pa)	101325
Vapor pressure	P_v (Pa)	3169
Pressure amplitude	P_a (Pa)	$0.93P_0$
Viscous damping	μ (kg/(m·s))	0.001
Thermal damping	μ_t (kg/(m·s))	0.0057
Driving frequency	f (kHz)	1.0
Liquid velocity at inlet	V_f (m/s)	0.00926
Polytropic exponent	γ	1.4

6.3.2. Modelling results of bubble oscillation and translation

A typical case of a spherical bubble of $R_0=0.075$ mm under the periodic pressure fluctuation with $P_a=0.93P_0$ is calculated, and the initial displacement of the bubble, x_0 , is set at -8.25 mm for the bubble located nearby two inclined walls, which is analogous to the experimental observations. The coupled equations Eqs. (6.29) and (6.30) are solved by using the ODE function in MATLAB and the results for the bubble radius and displacement are plotted in Fig. 6.8 and more details for the bubble radius and displacement over two periods are shown in Fig. 6.9.

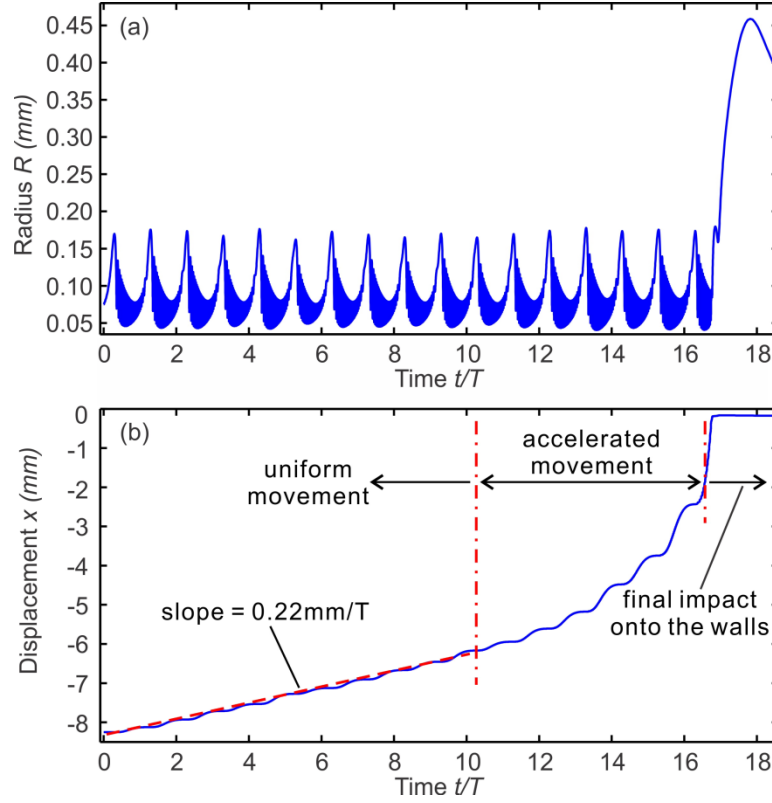


Fig. 6.8 The whole process of the motions of the bubble nearby two tapered walls. The whole bubble movement corresponds to three stages: uniform movement, accelerated movement and final impact towards the walls. (a) Radius of the bubble with time. (b) Displacement of the bubble with time. The bubble travels at an average velocity of 0.22 m/s in the stage of uniform movement.

The whole process of the bubble's motion is presented in Fig. 6.8. We can see that the bubble travels upstream from the initial position ($x_0 = -8.25$ mm) to the intersection point of the tapered walls, corresponding to three stages: uniform movement, accelerated movement and final impact towards the walls. Initially, the bubble moves upstream at an almost uniform average velocity, which is so-called uniform movement. In this stage, the average translation velocity is about 0.22 m/s, which agrees well with the experimental velocity of the bubble in zone 2 (0.23 m/s). In closer proximity to the walls, the bubble is accelerated to move forward. In the stage of final impact towards the walls, the bubble is experiencing non-spherical deformation. In this stage, the analytical model is not applicable.

The details of the bubble's oscillation and translation over two periods are demonstrated in Fig. 6.9. As shown in Fig. 6.9(a), the response of the bubble does not follow the sinusoidal actuation of the pressure fluctuation but appears strong and stable nonlinearity: during one cycle, the bubble grows up rapidly and then experiences a steep collapse followed by a series of after-

bounces. The bubble radius varies from 0.05 mm to 0.16 mm in one cycle with a ratio of R_{max}/R_{min} about 3.2, which is comparable to the ratio of 2.8 in our experiments. As shown in Fig. 6.9(b), the bubble translation mainly occurs in the collapse phase (indicated by two dot-dashed lines) with an average velocity about 0.6 m/s. While in the growth phase, the bubble does not move forward but slightly backward. This feature is also agreeable with our experimental observations in Fig. 6.5. The bubble's oscillation and translation predicted by the model demonstrate that, although several simplifications and assumptions are made in the present analytical model, the results, including bubble oscillation, translation direction and velocity, are semi-quantitatively comparable with the experimental observations.

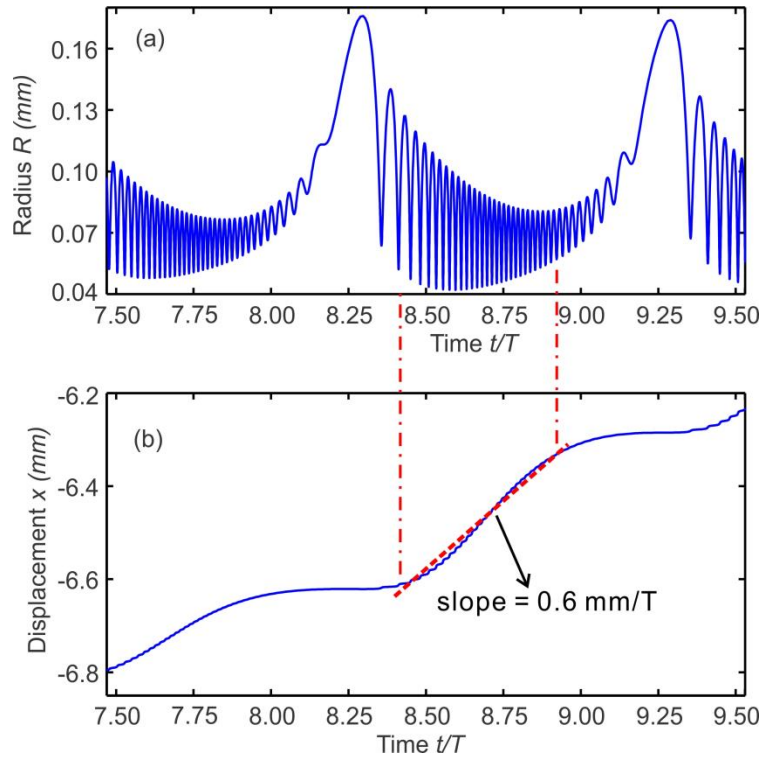


Fig. 6.9 (a) Details of the radius in two successive periods for the bubble nearby two inclined walls in an oscillatory pressure field. (b) Details of the displacement in two successive periods for the bubble nearby two inclined walls in an oscillatory pressure field.

6.3.3. Further discussion of bubble translation – wall effect

The results from both the experiments (Figs. 6.3 and 6.5) and analytical model (Figs. 6.8 and 6.9) show that the bubbles under the low-frequency actuation translate upstream towards the proximity of the walls. To explore the driving mechanism for the bubble translation, we

investigate the motion of the same bubble in infinite liquid under otherwise the same conditions and further the bubble-wall interaction is studied in terms of the mutual force between the real bubble and the image bubbles.

6.3.3.1 Comparison with bubble translation in infinite liquid

It is known that at high-frequency actuations, the wavelength of acoustic pressure is short and comparable to the microfluidic channel scale and the bubble size, and a strong acoustic field will be established inside the fluidic chamber. The bubbles in the strong acoustic field will experience acoustic forces, such as the primary Bjerknes force which is associated with the pressure gradients. The primary Bjerknes force is normally the main driving force corresponding to the bubble translations at high frequency actuations. However, the situation is different at the low-frequency actuations. In the present study, the actuation frequency is 1 kHz and the actuation pressure wavelength is about 1.5m (the sound speed in water is 1500m/s), which is much greater than the dimension of the microfluidic chamber (0.02 m-0.07 m). As a result, the actuated pressure is almost uniformly distributed in the microfluidic chamber and the pressure gradient is very small in the fluid, leading to a negligible primary Bjerknes force on the bubbles.

In order to further illustrate the wall effect, the model of a single bubble in an infinite liquid (without any walls) constructed by Doinikov [8] is solved here. All the actuation conditions are the same as that used in our model except that the bubble is free in the infinite liquid. The radius and displacement of the free bubble are plotted in Fig. 6.10(a) and 6.10(b), respectively. The results in Fig. 6.10(a) show that the bubble oscillation is less violent than the results of the bubble with two inclined solid walls. The bubble experiences a volume oscillation with its radius varying from 0.05mm to 0.15mm with smaller volume ratio (about 3.0) in one cycle. But the bubble translation is very different. As shown in Fig. 6.10(b), the free bubble under the actuation will remain stationary if there is no mainstream flow, or will be drifted following the mainstream flow from the right to the left when a main flow is imposed. From the comparison of the bubble translations without walls and nearby two intersected walls, it can be concluded that only the pressure fluctuation cannot drive the bubble to move forward and the bubble translation within two inclined walls towards upstream is attributed to the wall effects. In other words, the bubble translation is due to the action of the nearby walls, not the force from the external actuations. In

our experiments, the walls of the nozzle at zone 2 play the similar role as the inclined walls in the model.

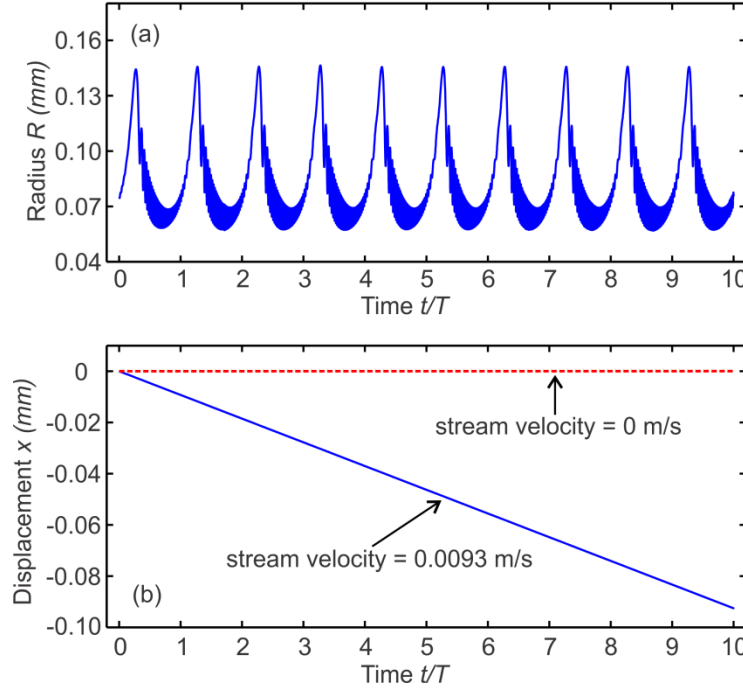


Fig. 6.10 (a) Radius of a bubble in infinite water under the oscillatory pressure actuations. (b) Displacement of a bubble in infinite water under the oscillatory pressure actuations. The bubble remains stationary in the stationary fluid (dashed line) or travels with the main stream at the stream velocity (solid line).

6.3.3.2 The secondary Bjerknes force

It has been known that the bubble translation within two inclined walls towards upstream is attributed to the wall effects. However, it is unclarified that why the force between the bubble and the nearby walls are attractive or how the wall effects on the real bubble work. From the analytical modelling of the bubble's oscillation and translation, we can see that the intersected walls around the bubble are replaced by 11 image bubbles, which impose their effects on the bubble's motion. It is known that the oscillation of one bubble can lead to radiation force on the nearby bubble due to the induced pressure disturbance, which is so-called secondary Bjerknes force. Herein, we can study the secondary Bjerknes force between the real bubble and image bubble to explore the nature of the bubble-wall interaction.

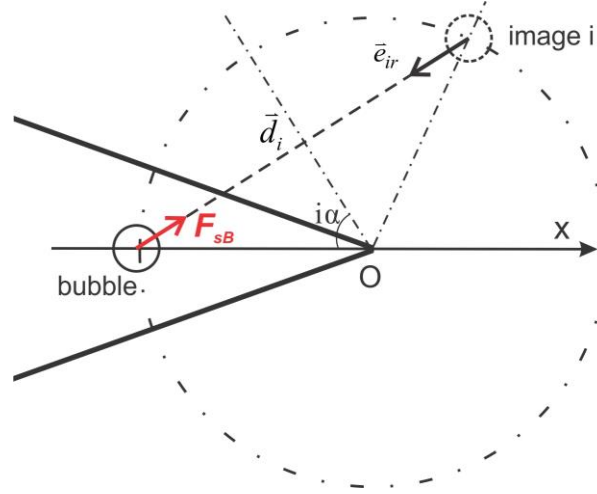


Fig. 6.11 Illustration of the real bubble and i th image bubble.

For simplicity, let us assume that the bubble of radius R together with its all image bubbles is fixed at some position nearby the intersected boundary walls. As shown in Fig. 6.11, the distance between the real bubble and the i th bubble is constant. Omitting the high-ordered convective term of the Navier-Stokes equation, the governing equation of the liquid around the bubble is

$$\rho \frac{\partial \vec{V}}{\partial t} + \nabla p = 0 \quad (6.31)$$

where V is the liquid velocity caused by the oscillation of the image bubble, ρ is the liquid density and p is the pressure emitted by the oscillating image bubble.

The oscillating velocity of the image bubble can be calculated

$$V_i^r = \frac{R^2 \dot{R}}{r_i^2} \quad (6.32)$$

Substituting Eq. (6.32) into Eq. (6.31), we can obtain the pressure gradient resulting from the image bubble's oscillation,

$$\frac{\partial p}{\partial r} = -\rho \frac{\partial V_i^r}{\partial t} = -\frac{\rho}{r_i^2} \frac{d}{dt} (R^2 \dot{R}) \quad (6.33)$$

At the center of the real bubble, the pressure gradient caused by the image bubble's oscillation can be obtained immediately,

$$\left. \frac{\partial p}{\partial r} \right|_{r_i=d_i} = -\frac{\rho}{d_i^2} \frac{d}{dt} (R^2 \dot{R}) \quad (6.34)$$

The secondary Bjerknes force for a bubble of volume V_b in liquid of a pressure gradient ∇p reads as,

$$\bar{F}_{sB} = -V_b \nabla p \quad (6.35)$$

Substituting Eq. (6.34) into Eq. (6.35), one obtains the secondary Bjerknes force of the image bubble on the real bubble,

$$\bar{F}_{sB} = \frac{\rho V_b}{D^2} \frac{d}{dt} (R^2 \dot{R}) \bar{e}_{ir} = \frac{\rho}{4\pi D^2} V_b \ddot{V}_b \bar{e}_{ir} \quad (6.36)$$

where, \bar{e}_{ir} is the unit of the pressure gradient in the radial direction.

When the bubble oscillates periodically with time, the net force on the real bubble is the time average of \bar{F}_{sB} over one period,

$$\langle \bar{F}_{sB} \rangle = \left\langle \frac{\rho}{4\pi D^2} V_b \ddot{V}_b \right\rangle \bar{e}_{ir} = \frac{\rho}{4\pi D^2} \left[\frac{1}{T} (V\dot{V}) \Big|_0^T - \langle \dot{V}^2 \rangle \right] \bar{e}_{ir} = -\frac{\rho}{4\pi D^2} \langle \dot{V}^2 \rangle \bar{e}_{ir} \quad (6.37)$$

where, $\langle \rangle$ denotes the time average value. In the coordinate system, the negative net value of \bar{F}_{sB} means the force directed to the image bubble or the real bubble is attracted by the image bubble. Therefore, the mutual force $\langle \bar{F}_{sB} \rangle$ is always attractive since $\langle \dot{V}^2 \rangle$ is always positive. In the analytical model, the real bubble is attracted by the image bubble behind the nearby boundary walls due to the secondary Bjerknes force, which also explains why the bubble moves upstream against the hydrodynamic flow in the experiments.

6.4 Summary

In this chapter, the dynamics of a single bubble in a microfluidic chamber under low-frequency actuations has been investigated both experimentally and analytically. A single bubble is generated in the microfluidic chamber with low-voltage actuation (120 V). After being generated, the bubble under actuation is found to translate against the hydrodynamic flow at an average velocity of about 0.23 m/s, and it undergoes significant expansion and compression with a ratio of the maximum to minimum volume up to 22. The bubble moves forward during a short time interval of the collapse phase with a velocity of 0.55 m/s.

A simplified analytical model which describes the dynamics of a bubble between two intersected boundaries is constructed for the first time to explore the mechanism of the bubble translation. This model extends the case of a bubble near a single flat wall to a bubble located between two intersected walls. Based on the assumptions of incompressible and potential flows,

the nearby boundary walls are replaced by 11 image bubbles and the governing equations of the bubble oscillation and translation are derived by the Lagrangian method. The bubble motions predicted by the model are agreeable with the experimental observations in terms of bubble oscillation and translation. The comparison between a bubble in infinite liquid and nearby two intersected walls shows that the bubble translation is due to the attractive secondary Bjerknes force induced by multiple image bubbles behind the two inclined walls, which is the so-called wall effect.

Chapter 7 Conclusions and Recommendations

7.1 Conclusions

The vortex generation and control, and bubble dynamics have been investigated in a resonator-shaped microfluidic chamber with PZT actuations. The following conclusions are drawn from this study based on the achieved results.

(1) A novel method of generating vortices has been demonstrated in a microfluidic chamber incorporated with a PZT actuator. Once being switched on at proper conditions, large-scale and asymmetric vortices are formed inside the chamber, while only laminar flows would exist otherwise. The generation and intensity of the vortex can be controlled by actuation voltage, frequency and flowrate. There is a frequency window between 1.5 kHz and 3 kHz, within which the vortex can be generated with strong intensity and out of this range, the vortex is very weak, or even unable to occur. The vortex intensity increases with the actuation voltage, from less than 20% at 40 V to 80% at 100 V. At 120 V, bubbles can be generated in addition to the vortices. The vortex intensity decreases with flowrate. The microfluidic chamber with resonator-shaped nozzle has much stronger vortices than a common circular chamber. The vortices generated in the chamber can be either clockwise or counter-clockwise while only one regime of vortex is generated in one specific device.

(2) By modifying the microfluidic chamber by dividing the PZT disk into two parts which can be actuated separately, the direction of the generated vortex can be shifted on-demand from clockwise to counterclockwise by simply switching between two different transducers. Such device for vortex generation can generate two regimes of vortices – CW (clockwise) vortex and CCW (counter-clockwise) vortex when the PZT disk is actuated at proper conditions. The vortex intensity can be tuned by the actuation frequency, voltage and flowrate, which is similar to the previous microfluidic chamber. PIV measurements show that the flow in the outlet channel is pulsatile with the vibration of the PZT disk and the transient velocity is as large as 0.4 m/s within the frequency window between 1.5 kHz and 3 kHz, leading to large Reynolds number. The vortex generation in the chamber with actuations is due to the flow instability when the fluids are driven through the sudden expansion part of the outlet channel at high Reynolds number. Based

on the vibration measurement of the PZT disk, it is found that the frequency window for vortex generation and flow velocity in the outlet is agreeable with the frequency range for the vibration velocity of the PZT disk, rather than the vibration displacement of the PZT disk.

(3) Bubbles are induced when actuation voltage exceeds a threshold (120 V), and such type of bubble generation is novel and different from those conventional bubble generations in acoustic fields, which are normally at high frequencies (> 20 kHz). The dynamics of multi-bubbles in the chamber with actuations at 1 kHz has been investigated both experimentally and numerically. Under the actuations, the bubbles are observed to start near the center of the chamber, grow up in size and move upstream against the hydrodynamic flow from inlets. When the bubbles are translating forward, coalescences and breakups happen frequently, leading to vigorous motions of the surrounding liquid and a significant effect on mass transfer. The simulation results show that in each actuation cycle there is a low-pressure zone in the chamber which matches the area of bubble generation observed in the experiment. The minimum pressure in this zone is related to a high-pressure fluctuation above the Blake threshold, which leads to the bubble generation.

(4) The bubbles can be generated to form as a single bubble, or as a group of bubbles in a cloud, depending on the applied voltage and the degree of the fluid degassing. For the simplicity of quantitative analysis, the motion of a single bubble is investigated both experimentally and analytically. Under the actuations, the bubble undergoes significant expansion and compression with a ratio of the maximum to minimum volume up to 22. After being generated, the bubble under actuations is found to translate along a straight line against the hydrodynamic flow at an average velocity of about 0.23 m/s. The bubble movement mainly occurs during a short time interval of collapse phase. A simplified analytical model which describes the dynamics of a bubble between two intersected boundaries is constructed to simulate the bubble oscillation and translation. The governing equations of the bubble radius and displacement are derived by using the Lagrangian method. The motions of the bubble predicted by the model are agreeable with the experimental observations in terms of oscillation and translation. The comparison between a bubble in infinitely large liquid domain and nearby two intersected walls shows that the bubble translation is due to the attractive secondary Bjerknes force of multiple image bubbles behind the two inclined walls, which is the so-called wall effect.

7.2 Recommendations for Future Work

In this study, the vortex generation and control, and bubble dynamics have been investigated in detail by means of experimental visualization and numerical simulation. However, there are several unsolved problems which are worthwhile to be studied further in future. The following are two recommendations.

(1) The flow field in the chamber needs to be characterized by means of PIV measurement to justify the proposed mechanism of vortex generation. It would be useful to conduct numerical simulation to study the vortex formation in the microfluidic chamber with actuations and make direct comparison with the PIV results.

(2) The dynamics of the bubble in the chamber with low-frequency actuations has been studied. The applications of the bubble in microfluidics can be further explored, such as manipulations of micro/nano particles by means of an oscillating bubble, including the particle trapping, sorting, migration or even patterning.

Publication List

XP Shang, XY Huang, C Yang, “The interactions between a gas bubble and a movable sphere in an oscillatory pressure field,” (in preparation)

XP Shang, XY Huang, C Yang, “Vortex generation and control in a microfluidic chamber with actuations,” *Physics of Fluids*, **28**, 122001 (2016).

XP Shang, XY Huang, C Yang, “Bubble dynamics in a microfluidic chamber under low-frequency actuation,” *Microfluidics Nanofluidics*, **20**, 14 (2016).

XP Shang, XY Huang, C Yang, “Mixing enhancement by the vortex in a microfluidic mixer with actuation,” *Experimental Thermal and Fluid Science*, **67**, 57 (2015).

XP Shang, XG Cui, XY Huang, C Yang, “Vortex generation in a microfluidic chamber with actuations,” *Experiments in Fluids*, **55**, 1758 (2014).

XP Shang, XY Huang, C Yang, “Bubble translation at low-frequency actuation in a resonator-shaped microfluidic chamber,” *The 7th International Conference on Fluid Mechanics*, Qingdao/China (2015).

XP Shang, XY Huang, C Yang, “Mixing enhancement by the vortex in a microfluidic mixer with actuation,” *The 5th International Conference on Heat Transfer and Fluid Flow in Microscale*, Marseille/France (2014).

References

- [1] G. M. Whitesides, "The origins and the future of microfluidics," *Nature* 442, 368 (2006).
- [2] A. J. Mach, J. H. Kim, A. Arshi, S. C. Hur and D. D. Carlo, "Automated cellular sample preparation using a Centrifuge-on-a-Chip," *Lab Chip* 11, 2827 (2011).
- [3] N. Nguyen and Z. Wu, "Micromixers – a review," *J. Micromech. Microeng.* 15, R1 (2005).
- [4] X. P. Shang, X. Huang and C. Yang, "Mixing enhancement by the vortex in a microfluidic mixer with actuation," *Exp. Therm. Fluid Sci.* 67, 57 (2015).
- [5] W. Lauterborn and T. Kurz, "Physics of bubble oscillations," *Rep. Prog. Phys.* 73, 106501 (2010).
- [6] M. S. Plesset and P. Calif, "The dynamics of cavitation bubbles," *J. Appl. Mech.* 16, 277 (1949).
- [7] L. Crum and A. Eller, "Motion of bubbles in a stationary sound field," *J. Acoust. Soc. Am.* 48, 181 (1970).
- [8] A. A. Doinikov, "Translational motion of a spherical bubble in an acoustic standing wave of high intensity," *Phys. Fluids* 14, 1420 (2002).
- [9] Y. Liu, K. Sugiyama, S. Takagi and Y. Matsumoto, "Surface instability of an encapsulated bubble induced by an ultrasonic pressure wave," *J. Fluid Mech.* 691, 315 (2012).
- [10] Tandiono, S. W. Ohl, D. S. W. Ow, E. Klaseboer, V. V. Wong, R. Dumke and C. D. Ohl, "Sonochemistry and sonoluminescence in microfluidics," *Proc. Natl. Acad. Sci.* 108, 5996 (2011).
- [11] M. J. Lighthill, *An informal introduction to theoretical fluid mechanics* (Oxford University Press, London, 1986) p.68.
- [12] T. V. Karman, *Aerodynamics: selected topics in the light of their historical development* (Cornel University Press, New York, 1954) p.67.
- [13] G. I. Taylor and A. E. Green, "Mechanism of the production of small eddies from large ones," *Proc. R. Soc. Lond. A* 158, 499 (1937).
- [14] M. E. Brachet, M. Meneguzzi, H. Politano and P. L. Sulem, "The dynamics of freely decaying two-dimensional turbulence," *J. Fluid Mech.* 194, 333 (1988).
- [15] A. Babiano, C. Basdevant, B. Legras and R. Sadourny, "Vorticity and passive-scalar dynamics in two-dimensional turbulence," *J. Fluid Mech.* 183, 379 (1987).
- [16] G. Haller, "An objective definition of a vortex," *J. Fluid Mech.* 525, 1 (2005).
- [17] A. D. Strook, S. K. W. Dertinger, A. Ajdari, I. Mezic, H. A. Stone and G. M. Whitesides, "Chaotic mixer for microchannels," *Science* 295, 647 (2002).
- [18] V. Mengeaud, J. Josserand and H. H. Girault, "Mixing Processes in a Zigzag Microchannel: Finite Element Simulations and Optical Study," *Anal. Chem.* 74, 4279 (2002).
- [19] X. Wang, J. Zhou and I. Papautsky, "Vortex-aided inertial microfluidic device for continuous particle separation with high size-selectivity, efficiency, and purity," *Biomicrofluidics* 7, 044119 (2013).
- [20] M. S. N. Oliveira, F. T. Pinho and M. A. Alves, "Divergent streamlines and free vortices in Newtonian fluid flows in microfluidic flow focusing devices," *J. Fluid Mech.* 711, 171 (2012).

- [21] R. H. Liu, A. S. Stremler, K. V. Sharp, M. G. Olsen, J. G. Santiago, R. J. Adrian, H. Aref and D. J. Beebe, "Passive Mixing in a Three-Dimensional Serpentine Microchannel," *J. Microelectromech. Syst.* 9, 190 (2000).
- [22] M. K. Singh, T. G. Kang, H. E. H. Meijer and P. D. Anderson, "The mapping method as a toolbox to analyze, design, and optimize micromixers," *Microfluid. Nanofluid.* 5, 313 (2008).
- [23] T. G. Kang, M. K. Singh, T. H. Kwon and P. D. Anderson, "Chaotic mixing using periodic and aperiodic sequences of mixing protocols in a micromixer," *Microfluid. Nanofluid.* 4, 589 (2008).
- [24] C. Simonnet and A. Groisman, "Chaotic mixing in a steady flow in a microchannel," *Phys. Rev. Lett.* 94, 134501 (2005).
- [25] M. Camesasca, M. Kaufman and I. M. Zloczower, "Staggered passive micromixers with fractal surface patterning," *J. Micromech. Microeng.* 16, 2298 (2006).
- [26] T. M. Squires and M. Z. Bazant, "Induced-charge electro-osmosis," *J. Fluid Mech.* 509, 217 (2004).
- [27] Z. Wu and D. Li, "Micromixing using induced-charge electrokinetic flow," *Electrochimica Acta* 53, 5827 (2008).
- [28] H. Y. Wu and C. H. Liu, "A novel electrokinetic micromixer," *Sensors Actuat. A* 118, 107 (2005).
- [29] N. Sasaki, T. Kitamori and H. B. Kim, "AC electroosmotic micromixer for chemical processing in a microchannel," *Lab chip* 6, 550 (2006).
- [30] S. H. Huang, S. K. Wang, H. S. Khoo and F. G. Tseng, "Ac electroosmotic generated in-plane microvortices for stationary or continuous fluid mixing," *Sensors Actuat. B* 125, 326 (2007).
- [31] A. Kumar, S. Williams and S. T. Wereley, "Experiments on opto-electrically generated microfluidic vortices," *Microfluid. Nanofluid.* 6, 637 (2009).
- [32] C. Park and S. T. Wereley, "Rapid generation and manipulation of microfluidic vortex flows induced by AC electrokinetics with optical illumination," *Lab Chip* 13, 1289 (2013).
- [33] R. H. Liu, J. Wang, M. Z. Pindera, M. Athavale and P. Grodzinski, "Bubble-induced acoustic micromixing," *Lab Chip* 2, 151 (2002).
- [34] D. Ahmed, X. Mao, J. Shi, B. K. Juluri and T. J. Huang, "A millisecond micromixer via single-bubble-based acoustic streaming," *Lab Chip* 9, 2737 (2009).
- [35] C. Wang, B. Rallabandi and S. Hilgenfeldt, "Frequency dependence and frequency control of microbubble streaming flows," *Phys. Fluids* 25, 022002 (2013).
- [36] B. Rallabandi, C. Wang and S. Hilgenfeldt, "Two-dimensional streaming flows driven by sessile semicylindrical microbubbles," *J. Fluid Mech.* 739, 57 (2014).
- [37] M. Grumann, A. Geipel, L. Riegger, R. Zengerle and J. Ducree, "Batch-mode mixing on centrifugal microfluidic platforms," *Lab Chip* 5, 560 (2005).
- [38] R. Calhoun, A. Yadav, P. Phelan, A. Vuppu, A. Garcia and M. Hayes, "Paramagnetic particles and mixing in micro-scale flows," *Lab Chip* 6, 247 (2006).
- [39] T. Franke, L. Schmid, D. A. Weitz and A. Wixforth, "Magneto-mechanical mixing and manipulation of picoliter volumes in vesicles," *Lab Chip* 9, 2831 (2009).

- [40] S. J. Kim, F. Wang, M. A. Burns and K. Kurabayashi, "Temperature-Programmed Natural Convection for Micromixing and Biochemical Reaction in a Single Microfluidic Chamber," *Anal. Chem.* 81, 4510 (2009).
- [41] M. Geissler, B. Voisin and T. Veres, "Air stream-mediated vortex agitation of microlitre entities on a fluidic chip," *Lab Chip* 11, 1717 (2011).
- [42] R. E. Apfel, "Acoustic cavitation inception," *Ultrasonics* 22, 167 (1984).
- [43] D. H. Trevena, "Cavitation and the generation of tension in liquids," *J. Phys. D: Appl. Phys.* 17, 2139 (1984).
- [44] D. E. Young, "Skins of varying permeability: a stabilization mechanism for gas cavitation nuclei," *J. Acoust. Soc. Am.* 65, 1429 (1979).
- [45] Trevena, *Cavitation and tension in liquids* (Hilger, Bristol, 1987) p.15.
- [46] F. Caupin, "Liquid-vapor interface, cavitation, and the phase diagram of water," *Phys. Rev. E* 71, 051605 (2005).
- [47] E. Herbert, S. Balibar and F. Caupin, "Cavitation pressure in water," *Phys. Rev. E* 74, 041603 (2006).
- [48] I. Akhatov and N. Gumerov, "The role of surface tension in stable single bubble sonoluminescence," *Phys. Rev. Lett.* 78, 227 (1997).
- [49] R. E. Apfel, "Acoustic cavitation prediction," *J. Acoust. Soc. Am.* 69, 1624 (1981).
- [50] F. R. Young, *Cavitation* (Imperial College Press, London, 1989) p. 44.
- [51] D. Y. Hsieh and M. S. Plesset, "Theory of rectified diffusion of mass into gas bubbles," *J. Acoust. Soc. Am.* 33, 206 (1961).
- [52] E. A. Neppiras, "Acoustic cavitation thresholds and cyclic processes," *Ultrasonics* 18, 201 (1980).
- [53] C. E. Brennen, *Cavitation and bubble dynamics* (Oxford University Press, London, 1995) p.89.
- [54] D. F. Gaitan, L. A. Crum, C. C. Church and R. A. Roy, "Sonoluminescence and bubble dynamics for a single, stable, cavitation bubble," *J. Acoust. Soc. Am.* 91, 3166 (1992).
- [55] H. Poritsky, in *Proceedings of the First U.S. National Congress on Applied Mechanics*, New York, U.S.A., 1952, edited by E. Sternberg, p. 813-821.
- [56] C. C. Church, "A theoretical study of cavitation generated by an extracorporeal shock wave lithotripter," *J. Acoust. Soc. Am.* 86, 215 (1989).
- [57] J. B. Keller and M. Miksis, "Bubble oscillation of large amplitude," *J. Acoust. Soc. Am.* 68, 628 (1980).
- [58] A. Prosperetti and A. Lezzi, "Bubble dynamics in a compressible liquid: part 1. First-order theory," *J. Fluid Mech.* 168, 457 (1986); A. Lezzi and A. Prosperetti, "Bubble dynamics in a compressible liquid: part 2. Second-order theory," *J. Fluid Mech.* 185, 289 (1987).
- [59] O. Louisnard and J. G. Garcia, *Acoustic cavitation in Ultrasound Technologies for food and bioprocessing* (Springer Science, 2011) p.21.
- [60] Z. C. Feng, "Nonlinear bubble dynamics," *Ann. Rev. Fluid Mech.* 29, 201 (1997).
- [61] L. L. Vignoli, A. L. F. Barros, R. C. A. Thome, A. L. Nogueira, R. C. Paschoal and H. Rodrigues, "Modeling the dynamics of single-bubble sonoluminescence," *Eur. J. Phys.* 34, 679 (2013).
- [62] S. Hilgenfeldt, M. P. Brenner, S. Grossmann and D. Lohse, "Analysis of Rayleigh-Plesset dynamics for sonoluminescing bubbles," *J. Fluid Mech.* 365, 171 (1998).

- [63] W. Lauterborn and R. Mettin, in *Proceedings of the NATO Advanced Study Institute*, Washington, U.S.A., 18-29 August 1997. edited by L. A. Crum, T. J. Mason, J. L. Reisse and K. S. Suslick, pp. 63-72.
- [64] K. W. Commander and A. Prosperetti, "Linear pressure waves in bubbly liquids: comparison between theory and experiments," *J. Acoust. Soc. Am.* 85, 732 (1989).
- [65] D. Z. Zhang and A. Prosperetti, "Ensemble phase-averaged equations for bubbly flows," *Phys. Fluids* 6, 2956 (1994).
- [66] B. Gompf and R. Pecha, "Mie scattering from a sonoluminescing bubble with high spatial and temporal resolution," *Phys. Rev. E* 61, 5253 (2000).
- [67] W. Lauterborn, T. Kurz, R. Mettin and C. D. Ohl, "Experimental and theoretical bubble dynamics," *Adv. Chem. Phys.* 110, 316 (1999).
- [68] D. Kroninger, Ph.D. thesis, University of Gottingen, 2008.
- [69] T. G. Leighton, A. J. Walton and M. J. W. Pickworth, "Primary Bjerknes force," *Eur. J. Phys.* 11, 47 (1990).
- [70] J. Magnaudet and D. Legendre, "The viscous drag force on a spherical bubble with a time-dependent radius," *Phys. Fluids* 10, 550 (1998).
- [71] D. Krefting, J. O. Toilliez, A. J. Szeri, R. Mettin and W. Lauterborn, "Translation of bubbles subject to weak acoustic forcing and error in decoupling from volume oscillation," *J. Acoust. Soc. Am.* 120, 670 (2006).
- [72] A. J. Reddy and A. J. Szeri, "Coupled dynamics of translation and collapse of acoustically driven microbubbles," *J. Acoust. Soc. Am.* 112, 1346 (2002).
- [73] A. A. Doinikov, "Translational motion of two interacting bubbles in a strong acoustic field," *Phys. Rev. E* 64, 026301 (2001).
- [74] R. Mettin, *Oscillations, waves, and interactions* (University of Gottingen Press, Gottingen, 2007) p.187.
- [75] J. R. Blake and D. C. Gibson, "Cavitation bubbles near boundaries," *Ann. Rev. Fluid Mech.* 19, 99 (1987).
- [76] R. H. Cole, *Underwater explosions* (Princeton University Press, Clinton, 1948) p.327.
- [77] K. Sato, Y. Tomita and A. Shima, "Numerical analysis of a gas bubble near a rigid boundary in an oscillatory pressure field," *J. Acoust. Soc. Am.* 95, 2416 (1994).
- [78] D. Kroninger, K. Kohler, T. Kurz and W. Lauterborn, "Particle tracking velocimetry of the flow field around a collapsing cavitation bubble," *Exp. Fluids* 48, 395 (2010).
- [79] X. Xi, F. Cegla, R. Mettin, F. Holsteysns and A. Lippert, "Collective bubble dynamics near a surface in a weak acoustic standing wave field," *J. Acoust. Soc. Am.* 132, 37 (2012).
- [80] X. Xi, F. Cegla, M. Lowe, A. Thiemann, T. Nowak, R. Mettin, F. Holsteysns and A. Lippert, "Study on the bubble transport mechanism in an acoustic standing wave field," *Ultrasonics* 51, 1014 (2011).
- [81] E. Klaseboer and B. C. Khoo, "An oscillating bubble near an elastic material," *J. Appl. Phys.* 96, 5808 (2004).
- [82] P. B. Robinson, J. R. Blake, T. Kodama, T. Shima and Y. Tomita, "Interaction of cavitation bubbles with a free surface," *J. Appl. Phys.* 89, 8225 (2001).
- [83] Y. Tomita, P. B. Robinson, R. P. Tong and J. R. Blake, "Growth and collapse of cavitation bubbles near a curved rigid boundary," *J. Fluid Mech.* 466, 259 (2002).

- [84] P. Garstecki, I. Gitlin, W. Diluzio, G. M. Whitesides, E. Kumacheva and H. A. Stone, "Formation of monodisperse bubbles in a microfluidic flow-focusing device," *Appl. Phys. Lett.* 85, 2649 (2004).
- [85] M. Shirota, T. Sanada, A. Sato and M. Watanabe, "Formation of a submillimeter bubble from an orifice using pulsed acoustic pressure waves in gas phase," *Phys. Fluids* 20, 043301 (2008).
- [86] D. Rabaud, P. Thibault, J. P. Raven, O. Hugon, E. Lacot, and P. Marmottant, "Manipulation of confined bubbles in a thin microchannel: Drag and acoustic Bjerknes forces," *Phys. Fluids* 23, 042003 (2011).
- [87] T. Segers and M. Versluis, "Acoustic bubble sorting for ultrasound contrast agent enrichment," *Lab Chip* 14, 1705 (2014).
- [88] E. Zwaan, S. L. Gac, K. Tsuji and C. D. Ohl, "Controlled Cavitation in Microfluidic Systems," *Phys. Rev. Lett.* 98, 254501 (2007).
- [89] P. A. Q. Su, K. Y. Lim and C. D. Ohl, "Cavitation bubble dynamics in microfluidic gaps of variable height," *Phys. Rev. E* 80, 047301 (2009).
- [90] A. Patrascioiu, J. M. Fernandez-Pradas, A. Palla-Papavlu, J. L. Morenza and P. Serra, "Laser-generated liquid microjets: correlation between bubble dynamics and liquid ejection," *Microfluid. Nanofluid.* 16, 55 (2014).
- [91] X. P. Shang, X. G. Cui, X. Y. Huang and C. Yang, "Vortex generation in a microfluidic chamber with actuations," *Exp. Fluids* 55, 1758 (2014).
- [92] J. Veilleux and S. Coulombe, "A total internal reflection fluorescent microscopy study of mass diffusion enhancement in water-based alumina nanofluids," *J. Appl. Phys.* 108, 104316 (2010).
- [93] S. Wang, X. Huang and C. Yang, "Mixing enhancement for high viscous fluids in a microfluidic chamber," *Lab Chip* 11, 2081 (2011).
- [94] J. Lighthill, "Acoustic streaming," *J. Sound Vib.* 61, 391 (1978).
- [95] N. Riley, "Steady streaming," *Ann. Rev. Fluid Mech.* 33, 43 (2001).
- [96] F. Durst, A. Melling and J. H. Whitelaw, "Low Reynolds number flow over a plane symmetric sudden expansion," *J. Fluid Mech.* 64, 111 (1974).
- [97] M. Shapira, D. Degani and D. Weihs, "Stability and existence of multiple solutions for viscous flow in suddenly enlarged channels," *Comput. Fluids* 18, 239 (1990).
- [98] J. Mizushima and Y. Shiotani, "Transitions and instabilities of flow in a symmetric channel with a suddenly expanded and contracted part," *J. Fluid Mech.* 434, 355 (2001).
- [99] A. Quaini, R. Glowinski and S. Canic, "Symmetry breaking and Hopf bifurcation for incompressible viscous flow in a contraction-expansion channel," *Int. J. Comput. Fluid Dyn.* 30, 7 (2016).
- [100] A. Revuelta, "On the two-dimensional flow in a sudden expansion with large expansion ratios," *Phys. Fluids* 17, 028102 (2005).
- [101] M. Dufresne, J. Vazquez, A. Terfous, A. Ghenaïm and J. B. Poulet, "Experimental investigation and CFD modelling of flow, sedimentation, and solids separation in a combined sewer detention tank," *Comput. Fluids* 38, 1042 (2009).
- [102] I. Sobey, "Observation of waves during oscillatory channel flow," *J. Fluid Mech.* 151, 395 (1985).

- [103] E. Roberts and M. Mackley, “The development of asymmetry and period doubling for oscillatory flow in baffled channels,” *J. Fluid Mech.* 328, 19 (1996).
- [104] X. P. Shang, X. Y. Huang and C. Yang, “Vortex generation and control in a microfluidic chamber with actuations,” *Phys. Fluids* 28, 122001 (2016).
- [105] W. Lauterborn and T. Kurz, “Physics of bubble oscillations,” *Rep. Prog. Phys.* 73, 106501 (2010).
- [106] M. Strasberg, “The pulsation frequency of nonspherical gas bubbles in liquids,” *J. Acoust. Soc. Am.* 25, 536 (1953).
- [107] B. F. Espinoza, R. Zenit and D. Legendre, “The effect of confinement on the motion of a single clean bubble,” *J. Fluid Mech.* 616, 419 (2008).
- [108] X. P. Shang, X. Y. Huang and C. Yang, “Bubble dynamics in a microfluidic chamber under low-frequency actuation,” *Microfluid. Nanofluid.* 20, 14 (2016).
- [109] T. G. Leighton, *The acoustic bubble* (Academic Press, San Diego, CA, 1994) p.72.
- [110] L. D. Landau and E. M. Lifshitz, *Fluid Mechanics* (Pergamon, Oxford, 1986).
- [111] B. V. Levich, *Physicochemical hydrodynamics* (Prentice-Hall, Englewood Cliffs, NJ, 1962).
- [112] A. Prosperetti, “Thermal effects and damping mechanisms in the forced radial oscillations of gas bubbles in liquids,” *J. Acoust. Soc. Am.* 61, 17 (1977).